The Dissertation Committee for Kohei Kajimoto
certifies that this is the approved version of the following dissertation:

A Large Area Time of Flight Detector for the STAR Experiment at RHIC

Committee:

Gerald Hoffmann, Supervisor

Eiichiro Komatsu

Christina Markert

Robert Ray

Peter Riley

A Large Area Time of Flight Detector for the STAR Experiment at RHIC

by

Kohei Kajimoto, B.S., M.S.

DISSERTATION

Presented to the Faculty of the Graduate School of

The University of Texas at Austin

in Partial Fulfillment

of the Requirements

for the Degree of

DOCTOR OF PHILOSOPHY

THE UNIVERSITY OF TEXAS AT AUSTIN

December 2009

A Large Area Time of Flight Detector for the STAR Experiment at RHIC

Publication No. _____

Kohei Kajimoto, Ph.D.
The University of Texas at Austin, 2009

Supervisor: Gerald Hoffmann

A large area time of flight (TOF) detector based on multi-gap resistive plate chamber (MRPC) technology has been developed for the STAR (Solenoidal Tracker at RHIC) experiment at the Relativistic Heavy Ion Collider at the Brookhaven National Laboratory, New York. The TOF detector replaces STAR's Central Trigger Barrel detector with 120 trays, each with 32 MRPCs. Each MRPC has 6 channels. The TOF detector improves by a factor of about 2 STAR's particle identification reach in transverse momenta and enhances STARs physics research program.

Table of Contents

List of Tables

List of Figures

Chapter 1

Introduction

In several fields of physics many-body systems behave very differently than their simple system analogs. From low temperature phenomena, such as superconductivity and Bose-Einstein condensates, to high temperature phenomena, such as electromagnetic plasmas, many-body systems persist as a fertile source of new physics for scientists. In a similar manner, nuclear physicists began to explore the system properties of strongly interacting particles after the nature of the strong interaction were revealed in the late 1960s. By the 1970's the theory of Quantum Chromodynamics (QCD) began to take the form we now know, with experimental evidence later confirming the theory.

1.1 Color Confinement and Asymptotic Freedom

QCD contains two types of elementary particles, quarks and gluons, and provides a description of the interactions among them. Quarks were originally introduced by Murray Gell-Mann and George Zweing in the context of the hadron spectroscopy as a virtual basis for a classification scheme based on group theory. Quarks have one of six flavors: 'up', 'down', 'charm', 'strange', 'top', or 'bottom' and carry a color charges (or anti-color charge): 'red', 'green', and 'blue' in ad-

dition to their regular electric charges. Table 1.1 shows the basic properties of quarks. They were later identified with partons found in deep inelastic scattering (DIS) experiments. In the DIS experiment performed by a SLAC-MIT group, high energy electrons collided with a fixed proton target.

	Mass [GeV/c^2]	Q_e	I_z
u	1.5 – 7 MeV	+2/3	+1/2
d	3 – 7 MeV	-1/3	-1/2
c	1.25 ± 0.09 MeV	+2/3	
s	95 ± 25 MeV	-1/3	
t	165 – 183 GeV	+2/3	
b	4.10 – 4.80 GeV	-1/3	

Table 1.1: Properties of Quarks[1].

This experiment revealed for the first time point-like electric substructure in the proton. R. P. Feynman and J. D. Bjorken introduced the parton model to interpret these results. To this day, quarks have never been directly observed and are believed to be confined in hadrons in a doublet or triplet structure of quarks and anti-quarks. This characteristic of quarks is expressed by the constraint of color charge neutrality in hadrons and is known as color confinement. The energy potential of this theory can be written (approximately) as

$$V(r) = -\frac{4\alpha_s}{3r} + kr \ , \tag{1.1}$$

where α_s is the coupling constant, k is the spring constant, and r is the distance between the two quarks. The first term describes the repulsive force necessary to sustain the hadron's finite size, and the second term describes confinement.

Confinement has not been shown in analytical QCD calculations. However, results from numerical calculations on a finite lattice, called lattice QCD (LQCD), support confinement's inclusion in the theory.

Another novel characteristic of QCD is asymptotic freedom. Discovered in the early 1970s by David Gross, Frank Wilczek and David Politzer, they shared the honor of a 2004 Nobel Prize in Physics for their discovery. The theory of renormalization groups allows for running coupling constants and for interactions to become weaker in the short-distance limit. As a consequence, quarks can become almost free in the limit of short distance. This is in remarkable contrast to color confinement, which states that quarks are limited to reside in finite sized color neutral objects. Asymptotic freedom played a critical role in the SLAC-MIT experiment where constituent quarks inside a proton could be probed as isolated charges by hard electrons.

1.2 Quark Gluon Plasma

Quark Gluon Plasma (QGP) is considered a state of matter in which the system's temperature and density are high enough that the quarks interact with each other in the region of asymptotic freedom. While color confinement still holds globally, the boundaries of hadrons disappear inside the QGP. It is believed that this state of matter existed just after the big bang. As the Universe cooled down, matter went through a freeze-out process forming hadrons and nuclei. The freeze out temperature is predicted to occur at $T_c \sim 170\,\mathrm{MeV}$ by lattice QCD. Due to this relatively low critical temperature, de-confinement is exptected to be obtainable in

a laboratory setting by colliding heavy nucleons at relativistic speeds. Relativistic heavy ion physics has attracted many scientists for a variety of reasons, including: (1) testing QCD itself, (2) studying matter under extreme conditions of pressure and temperature, (3) providing insight about the early evolution of the Universe, and (4) using this information to understand the properties of the cores of neutron stars.

1.3 Relativistic Heavy Ion Accelerators

The transition between normal nuclear matter and the QGP has been of great interest to scientists for years. This phase transition is called the deconfinement phase transition. Relativistic heavy ion accelerators are used to create, in a laboratory setting, the high temperatures and densities thought necessary to produce the QGP.

On February 10, 2000, CERN announced their finding of the QGP based on an accumulation of evidence from seven experiments done at the Super Proton Synchrotron (SPS). The Relativistic Heavy Ion Collider (RHIC), located at the Brookhaven National Laboratory (BNL), came online in the summer of 2000 just after the CERN announcement, and since then has served as the main facility for high energy heavy ion experiments in the world. Operating at a peak energy of $\sqrt{s_{NN}} = 200\,\mathrm{GeV}$, RHIC will remain at the energy frontier for heavy ion experiments until the Large Hadron Collider (LHC) at CERN comes online near 2010. The LHC's maximum design beam energy for Pb+Pb collisions is $\sqrt{s_{NN}} = 5.5\,\mathrm{TeV}$, roughly 30 times higher than that at RHIC.

1.4 New Physics Capabilities

The large area Time-of-Flight (TOF)detector subsystem will benefit all physics analyses in STAR. Four types of measurements and analyses are described in the following. The first involves the study of possible effects of a strongly interacting medium on two-particle correlations which result from conserved quantities. The second is the study of fragmentation in the heavy-ion collision environment. The third involves the reconstruction of resonances, while the fourth involves rare particles (e.g. D-mesons).

1.4.1 Two-particle Correlations and Conserved Quantities

RHIC-STAR Au+Au data reveal a complex correlation structure, including large-momentum-scale two-particle correlations in transverse momentum (p_t), pseudorapidity (η), and azimuth (ϕ), which provide direct access to a range of QCD phenomena available from no other experimental source. Charge-independent (isoscalar) and charge-dependent (isovector) correlation structures have been observed [2, 3] in two-dimensional, two-particle transverse momentum, pseudo-rapidity, and azimuthal angle correlations which are comparable in size to STAR's tracking detector's [Time Projection Chamber (TPC)] acceptance. To fully extract the information these correlations carry and to understand the role of nonperturbative QCD in Au+Au collisions at RHIC requires baryon - meson separation and at least some flavor dependence (strangeness) determination. Such measurements require particle identification (e.g. π, K, p) over the full STAR TPC acceptance, over a momentum range substantially exceeding that for dE/dx particle identi-

fication in the TPC. This capability will be afforded by the new Time-of-Flight (TOF) subsystem described in this thesis.

Conserved quantum numbers such as electric charge, baryon number, and quark flavor (in the strong interaction, e.g. strangeness) are expected to be locally conserved in hadron pair production in nuclear collisions. An interesting possibility is that the range over which local quantum number conservation affects the resulting two-particle correlations could be modified by the presence of a strongly interacting QCD medium. While a first observation of charge-dependent correlations of particles appears to exhibit gross features qualitatively similar to those observed in elementary p-p collisions, the study of possible medium induced modifications is just beginning. Baryon number and flavor-dependence conservation are however considered to be more sensitive probes of the QCD medium than charge conservation, which may be heavily influenced by the decays of resonances in the final state. The large acceptance of the TPC ($|\eta| < 1.5$, and 2π in azimuth) together with the new TOF detector will make possible measurements of the large-momentum-scale correlation structures associated with baryon number and flavor-dependence conservation.

1.4.2 Particle Flavor Dependent Fragmentation

A significant fraction of the particle production in central heavy-ion collisions at RHIC energies result from transverse partonic scattering and fragmentation. In the limit of large momentum transfers such processes produce well collimated sprays of particles known as "jets." However, due to the strong power-

law dependence of the perturbative QCD cross section, the bulk of such processes occur at relatively low momentum transfers of order a few GeV/c [4]. These "semi-hard" processes, or "minijets," [5] produce only a few charged particles which are broadly distributed on azimuth and pseudorapidity. It has been estimated that of order 20 - 40 semi-hard processes occur in a central Au-Au collision at $\sqrt{s_{NN}} = 200\,\mathrm{GeV}$ [6].

Two-particle correlation analyses show that the majority of the hadronic fragments from such processes are distributed on transverse momentum from about 0.5 to 2 GeV/c [6]. Thus, the use of energy loss (dE/dx) in the TPC for particle identification is ineffective whereas that afforded by the TOF is ideal for this type of analysis. The minijet fragments are spread over a large region of phase-space (relative η and ϕ of order 0.7). Correlations due to dijets occupy the full available phase-space of the STAR TPC. Thus, the large TOF angular acceptance enables the study of possible medium induced modifications of semi-hard parton fragmentation in heavy-ion collisions. Specifically, the TOF will make it possible to identify protons up to 3 GeV/c, and to measure the relative strengths of meson-meson, meson-baryon, and baryon-baryon azimuthal and rapidity correlations. These measurements will allow for a further understanding of particle flavor dependent fragmentation at RHIC energies and a deeper understanding of jet quenching phenomena in heavy-ion collisions.

The recent observation [7] of a jet-like correlation plus broad ridge structure on relative pseudorapidity among higher momentum particle pairs (typically above 2 GeV/c) requires complete flavor dependent decomposition of both structures

in order to guide our understanding of the ridge and its dynamical origins. Of particular interest are comparisons of the baryon-to-meson and strange-to-non-strange ratios for the lower p_t semi-hard scattering fragments (minijets), the higher momentum jets, the ridge and the soft, underlying event.

1.4.3 Physics of Resonances in Heavy Ion Collisions

In a thermal statistical description of heavy ion collisions the state of matter is thought to pass through two characteristic stages, chemical freeze-out and kinetic freeze-out. The former is when particle production and annihilation ceases, and the latter is when the constituent particles stop interacting and begin to free-stream to the experimental detectors. Between these two stages, elastic collisions can occur that transfer particle momentum but don't necessarily change particle flavor. Since most particles we observe experimentally pass through these stages after their hadronization, it is important to understand how and when these two transitions occur in order to trace back to hadronization. One way to accomplish this is by measuring the production of different resonance particles with varying lifetimes during these stages, then systematically using them to probe the dynamics of the matter. With these multiple probes, it might be possible to infer the dynamical evolution of the nuclear matter between chemical and kinetic freeze-out.

Within STAR the resonances studied thus far include ρ, Δ, f_0, K^*, $\Sigma(1385)$, $\Lambda(1520)$, and ϕ. The physics goals of these resonances measurements include [8]:

1. Providing experimental constraints on theoretical models of particle pro-

duction in heavy ion collisions. Contributions from resonance decays to the production of stable particles in the final state are significant and the contributions must be accounted for in detail by the models of particle production.

2. Studying the dense matter effects on various resonance particles. Measurements of mass-shifts and mass-width change, for example, have been proposed as methods to investigate the properties of the medium in which they are formed based on phenomenological QCD calculations.

3. Providing probes of the time evolution of the nuclear matter from chemical freeze-out to kinetic freeze-out. Since the lifetime of short lived resonances is comparable to the time span of the two time-out points, their survival probability is a good measure of the duration and the density of the medium.

In order to perform these resonance studies in heavy ion collisions, great care must be taken to differentiate the signal from the background. The particle identification (PID) capability of the experimental detector system plays a central role in reducing the background and enhancing the signal over background ratio of the measurement.

1.4.4 Open Charm Meson Reconstruction

RHIC is the first heavy ion facility with a sufficiently high center-of-mass energy that the low Bjorken x behavior of the parton structure functions of the nucleon are directly relevant to the initial collisions of the colliding nuclei. At low Bjorken x the gluon distribution is dominant, and it is therefore expected that

gluon dynamics will dominate the initial stage of the collision. An interesting conjecture is that at some scale of x and Q^2, the gluon distribution in the incoming nuclei is saturated, and that this may be reflected in the observed multiplicity [9].

Charm quark production in relativistic heavy ion collisions is particularly sensitive to the early gluon dominated stages of the collision. It can occur during initial parton-parton collisions, during the subsequent secondary parton cascade, and during the final hadron rescattering stage [10, 11]. Most $c\bar{c}$ production is expected to occur during the early partonic stages, much of it via hard gluon fusion, $gg \rightarrow c\bar{c}$. The cross section for this process is known. Parton scattering may also generate $c\bar{c}$, but the amount of such production depends strongly upon the parton energy distribution and longitudinal space-momentum correlations [10, 11, 12]. Because the yield of charm is sensitive to the details of the early collision stages, the measurement of the charm production rate is important for determining a proper description the initial conditions and early stages of relativistic nucleus-nucleus collisions.

The information afforded by the measurement of charm production, and specifically by D mesons, is particularly robust since the yield of mesons with open charm is weakly affected by final state interactions; charm quarks are produced during the early stages; are subsequently neither created or annihilated; and emerge from the collision, primarily as open-charm mesons or baryons. Studies of open charm differ in this respect from studies of the J/ψ, since the observed yield for charmonium is sensitive to screening in a color deconfined medium and final state hadronic scattering (medium) effects. The measurement of open charm

is indeed an important "calibration" for the study of J/ψ production [13, 14].

Open charm production studies using the barrel TOF will focus on: (1) constraining the initial state nuclear gluon structure function by comparing measured yields and spectra of D mesons with pQCD calculations, (2) establishing a baseline for studying J/ψ production, and (3) measuring possible energy loss of charm quark jets.

D meson yields will be measured by reconstructing an invariant mass spectrum for the K-π decay channel using event-mixing to generate the combinatorial background. Particle identification using the TOF is most important for correctly identifying the charged kaon daughters. The centroid of the p_t distribution for kaons that survive STARs acceptance and efficiency cuts is about 1 GeV/c. For kaons, PID based on dE/dx in the STAR TPC cuts off at 0.6 GeV/c. The proposed barrel TOF will extend PID for kaons to 1.7 GeV/c. As a consequence, $5\times$ more kaon daughters will be identified, and a better sampling of the kaon p_t distribution will be possible, greatly increasing the efficiency for D meson detection and reconstruction. The improvement will mainly serve to reduce the large combinatorial background in the invariant mass distribution.

1.5 Outline

This dissertation covers details of the Time of Flight (TOF) detector upgrade for the STAR detector at RHIC. In Chapter 2 an overview of RHIC is given, the STAR detector is described, and significant STAR results to date are discussed. Chapter 3 is devoted to a brief history of the STAR TOF project:

motivation for the upgrade, and details of TOF final design from mechanical design to electronics components. Chapter 4 provides a description of the Multi-gap Resistive Plate Chamber (MRPC) module tests and their results. Chapter 5 details the STAR TOF construction process, quality assurance work done during construction, noise measurements, and final tray testing and certification using cosmic ray test stands. Chapter 6 reports on installation and commissioning at STAR. The final chapter contains conclusions.

Chapter 2

The STAR Experiment

2.1 Relativistic Heavy Ion Collider

The RHIC Project began in the late 1980s and the experiment began running in the summer of 2000 with the primal intentions of studying: (1) the formation and properties of the QGP, and (2) the spin structure of the proton. The RHIC facility is located at Brookhaven National Laboratory, Upton, New York and contains a set of accelerators, transfer lines, detectors, and computational facilities used for simulations, data storage and analysis. The principal facility is the RHIC collider which was constructed in an existing tunnel that included a large helium refrigerator from the earlier ISABELLE/CBA project. The collider has two separate quasi-circular beam rings: a "blue ring" for the clockwise beam and a "yellow ring" for the counter-clockwise beam. Each ring has six straight sections with intersection points between 6 larger arc sections that form a 3.8 km circumference. The two beams are separated by 90 cm horizontally in the arc sections and alternate a left/right orientation between each of the intersection regions. A total of 1740 superconducting magnets, including various types of dipoles, quadrupoles and sextuples form a magnet lattice that is used to bend, focus, and steer the beams. The magnets are cooled to a temperature of $< 4.6\,\mathrm{K}$ by circulation of supercritical helium which is cooled by a 25 kW refrigerator[15].

A schematic of the accelerator complex is show in Figure 2.1. Gold (Au) beams start as negatively charged ions ($Q = -1$) originating from a pulsed sputter ion source. From there, they are accelerated by the Tandem Van de Graaff to 1MeV/u and partially stripped of orbital electrons ($Q = +32$). The beam is then delivered to the Booster Synchrotron, accelerated to 95 MeV/u, and again stripped of electrons to achieve a net charge of $Q = +77$ at the exit of the Booster. It continues to travel to the AGS where it is accelerated up to 10.8 GeV/u and undergoes a final electron stripping ($Q = +79$) before being injected into the RHIC collider via the AGS-to-RHIC (AtR) Beam Transfer Line. Likewise the polarized proton beam starts at the existing 200 MeV Linac and follows the same path as Au ion beams after injection into the Booster. In addition to the previously mentioned magnets, Siberian Snakes were installed at the RHIC collider to help maintain the polarizion of the proton beams for the spin physics program.

The maximum design energy of the RHIC beam is 100 GeV/nucleon for heavy ions, and 250 GeV for protons. The first collisions were achieved at $\sqrt{s_{\mathrm{NN}}} =$ 56 GeV on June 12, 2000, and later at 130 GeV during the 4-week physics run that followed. During the following 10 years, RHIC has operated with various configurations of p+p, Cu+Cu, d+Au, and Au+Au, typically operating for 3–6 months each year. Experiments are located at four of the six interaction regions located around RHIC. The four detectors systems are managed by four independent experimental collaborations: BRAHMS (2000-2006), PHOBOS (2000-2005), PHENIX, and STAR.

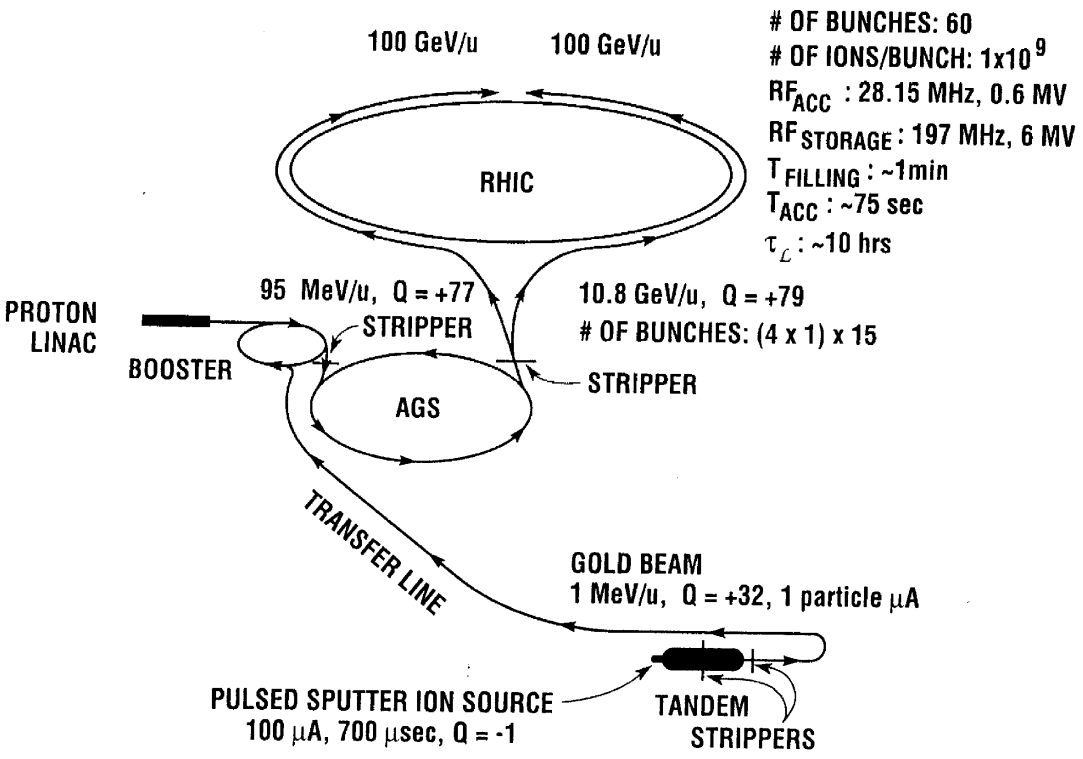

Figure 2.1: RHIC accelerator complex[15].

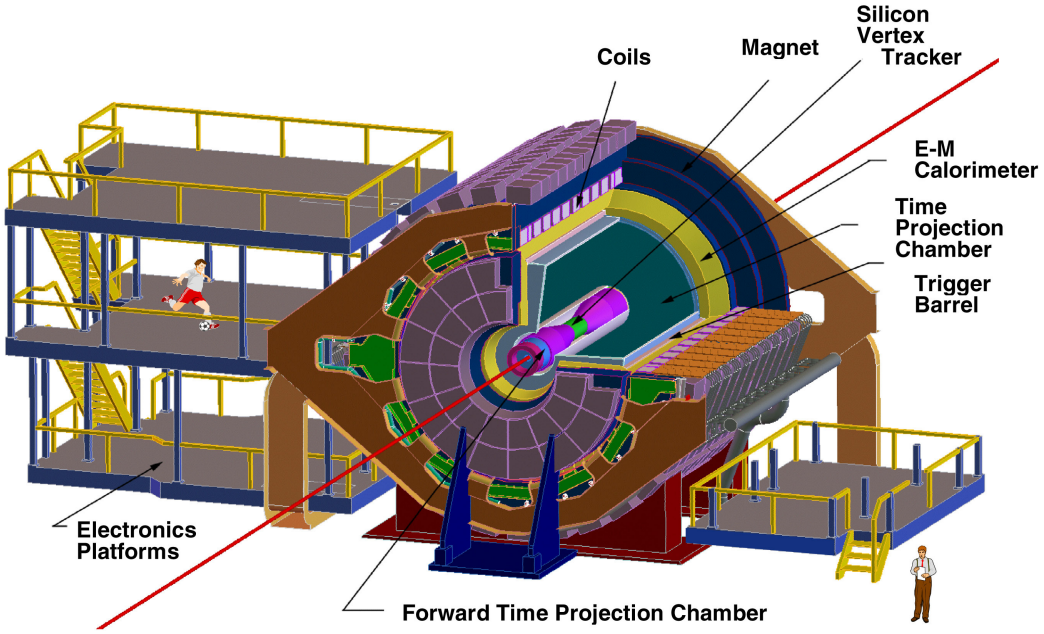

Figure 2.2: Schematic of the STAR detector

2.2 Solenoidal Tracker at RHIC

The Solenoidal Tracker at RHIC (STAR) is a detector consisting of several subsystems that employ multiple detector technologies for different purposes. STAR and its data acquisition (DAQ) [16] system are located at the 6 o'clock intersection position (south end) of the RHIC collider in a building called the Wide Angle Hall. The primary focus of the STAR detector is to measure, with large spatial acceptance, hadrons produced in heavy ion collisions. STAR is cylindrical in shape, sharing its central axis with the beam line. The subsystems generally form cylindrical layers around the beam axis. A schematic of the STAR detector is shown in Figure 2.2, and a cutaway view is show in Figure 2.3.

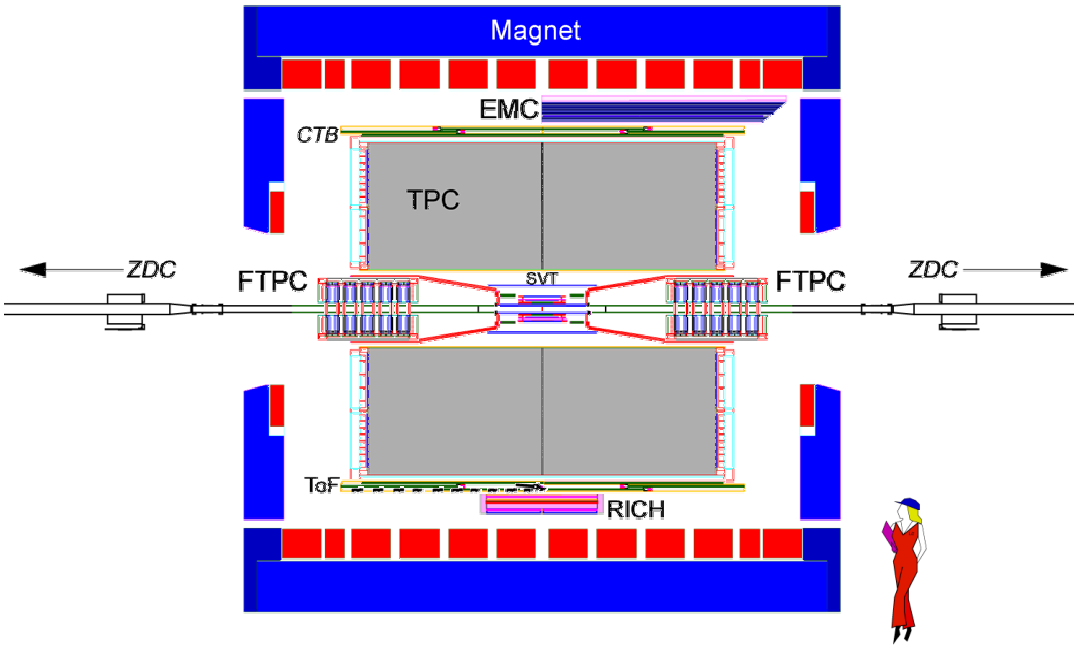

Figure 2.3: Cutaway view of the STAR detector.

Starting from the middle and working outwards, the subsystems consist of a silicon vertex tracker (SVT) [17] [recently decomissioned], one layer of silicon strip detectors (SSD) [18], a large volume time projection chamber (TPC) [19], a central trigger barrel (CTB) which is now upgraded to the time of flight detector (TOF), and a barrel electromagnetic calorimeter (BEMC) [20]. Additional subsystems are located in the forward direction, including a radial-drift time projection chamber (FTPC), an end-cap electromagnetic calorimeter (EEMC) [21], a beam-beam counter (BBC), a photon multiplicity detector (PMD) [22], a primary vertex position detector (pVPD) [23], a forward pion detector (FPD) / forward meson spectrometer (FMS), and a zero-degree calorimeter (ZDC) [24]. A solenoidal magnet also aligned with the beam axis supplies a nearly uniform magnetic field up to 0.5 T along beam axis (z-axis). The magnet field bends the transverse trajectory of charged particles such that their momenta can be determined from curvature of their paths and their angle with respect to the beam axis. The polarity of the magnetic field can be flipped, allowing for studies of systematic errors.

2.2.1 Time Projection Chamber

The TPC acceptance is 2π in azimuthal angle and over ± 1 in pseudo-rapidity η. It is STAR's primary detector and is used to track and identify charged particles originating from the beam collisions. The TPC is filled with a mixture of 10% methane and 90 % argon gas, which ionizes to release electrons as charged particles from the collisions pass through. The TPC's hollow chamber is barrel shaped with a radius of 200 cm and a length of 420 cm. It has multi-segmented

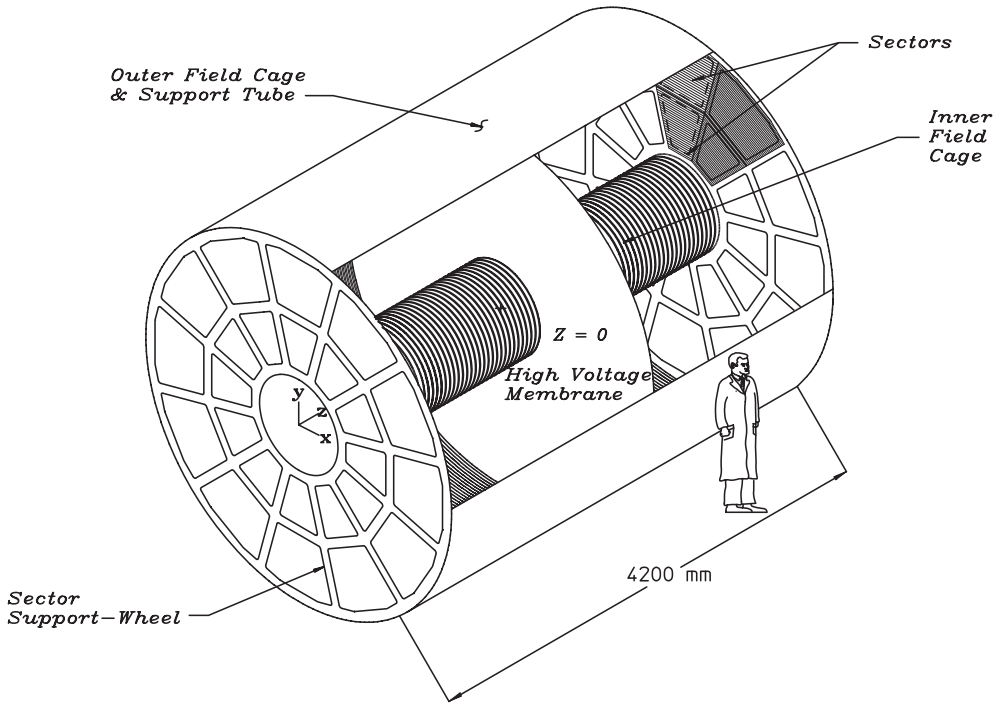

Figure 2.4: Schematic of STAR TPC[19].

readouts at two end caps where the electron showers are collected and used to reconstruct the originating particles path. Each end cap plane is divided into 12 radial sectors and each sector has two different readout pad patterns for the inner and outer parts of the endcaps. A schematic of the TPC is shown in Figure 2.4, and a diagram of one readout sector in the end cap is shown in Figure 2.5.

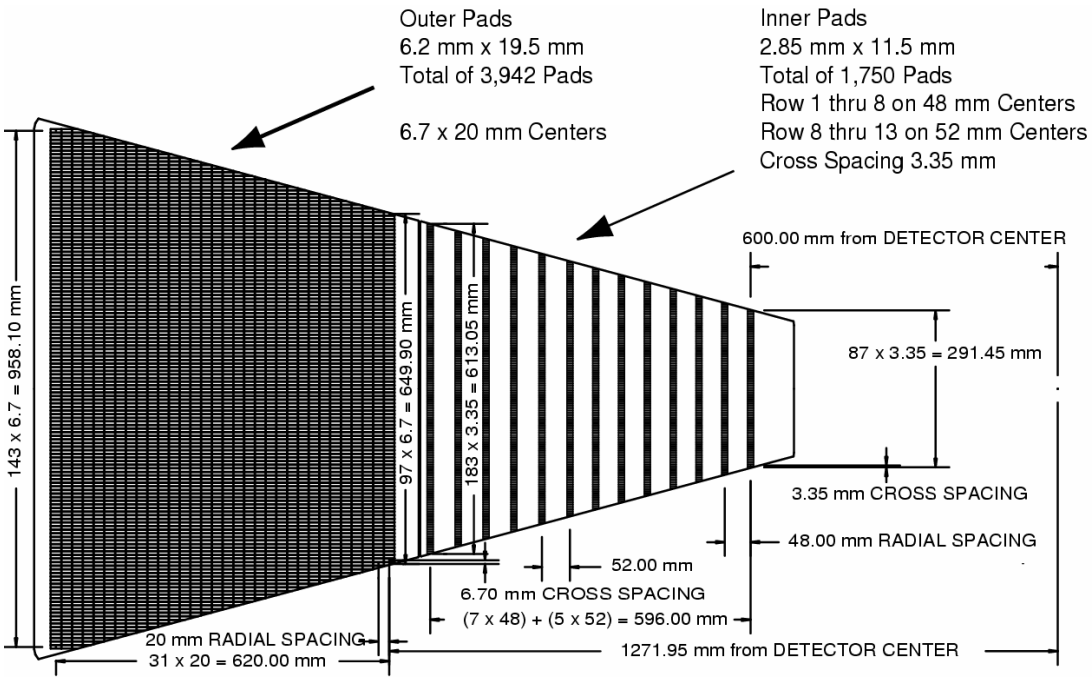

Figure 2.5: Schematic of one TPC readout sector[19].

2.2.2 Silicon Detectors

The two silicon detectors, the SVT and the SSD, track charged particles near the collision vertex in the pseudo-rapidity range $|\eta| \leq 1$ and full azimuthal angle $0 \leq \phi \leq 2\pi$. These detectors are used to make precision measurements of the primary interaction vertex and to locate the decay vertices of unstable particle shortly after they leave the collision region.

The SVT consists of three layers of multiple-ladders which have 4-7 silicon wafers. A picture and schematic of the the SVT are shown in Figure 2.6. The detector was installed in 2001 for RHIC Run-2, and was functional from Run-3 through Run-7[25]. It was decomissioned before Run-8.

The SSD consists of a single layer of 20 ladders with 16 silicon wafers and wraps around the SVT as a fourth layer. The system was installed for Run-4, and has been fully functional since Run-5[25]. Figure 2.7 shows an expansion diagram of an SSD ladder, and Figure 2.8 shows a fully assembled picture of the detector.

2.2.3 Electromagnetic Calorimeter

The two electromagnetic calorimeters, the BEMC and the EEMC, provide coverage over the region $-1 \leq \eta \leq 2$ and $0 \leq \phi \leq 2\pi$, and allow for energy measurements of high transverse momentum photons, electrons, and leptonic decaying hadrons such as neutral pions. Figure 2.9 shows the locations of the BEMC and the EEMC in STAR, Figure 2.10 shows a module of BEMC, and Figure 2.11 shows a module of EEMC.

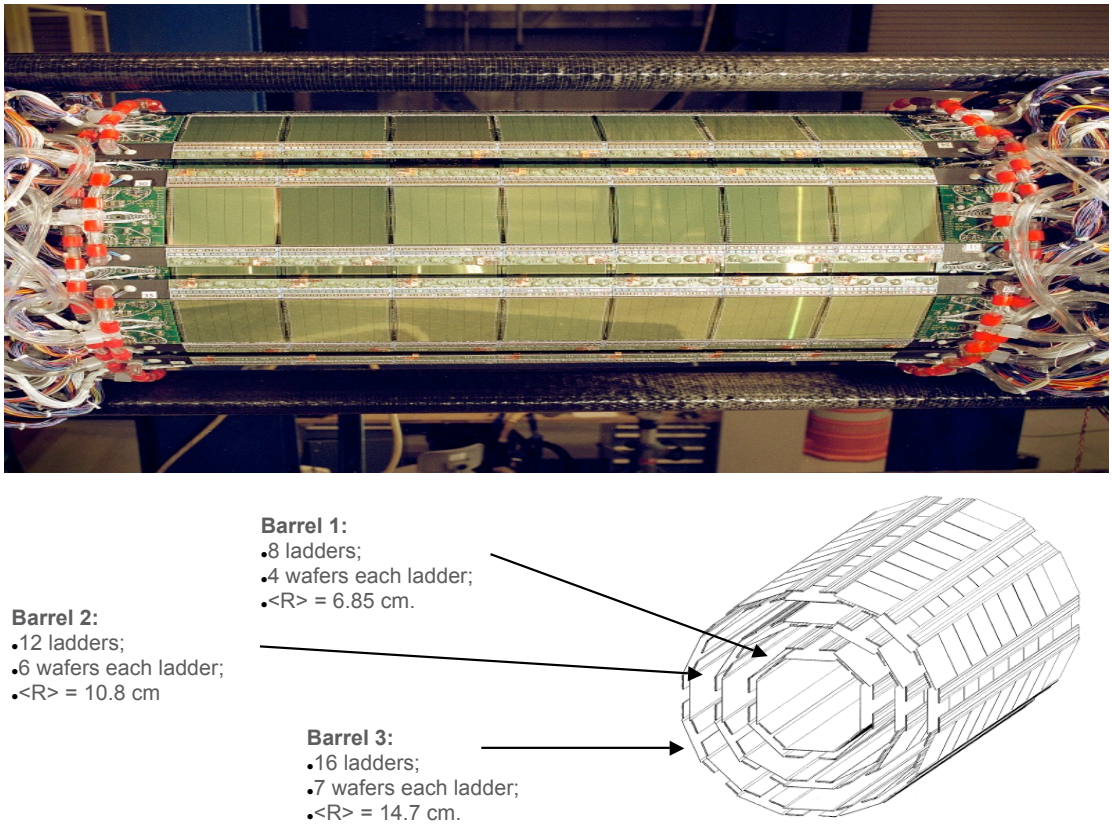

Figure 2.6: Picture and schematic of the SVT[25].

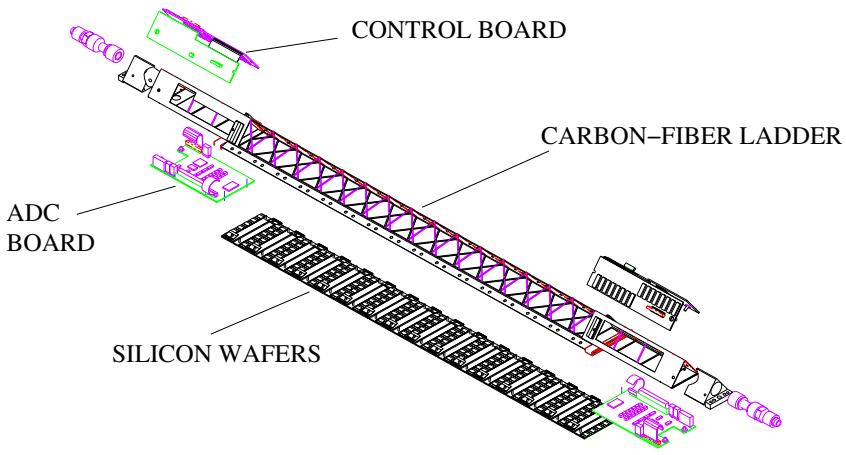

Figure 2.7: Expansion diagram of an SSD ladder[18].

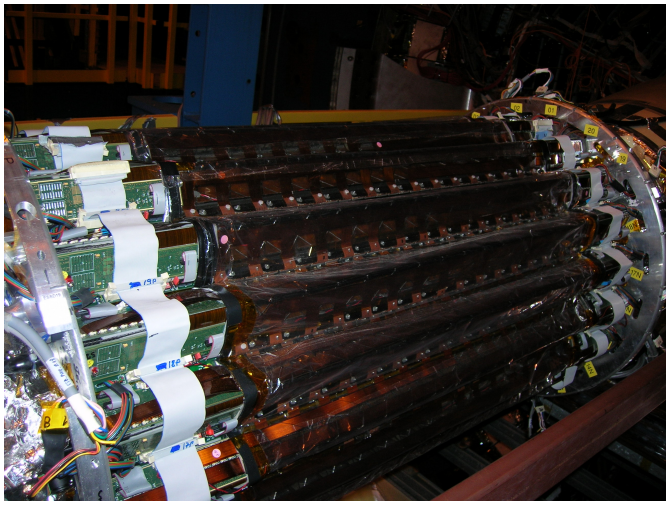

Figure 2.8: Picture of Silicon Strip Detector[25].

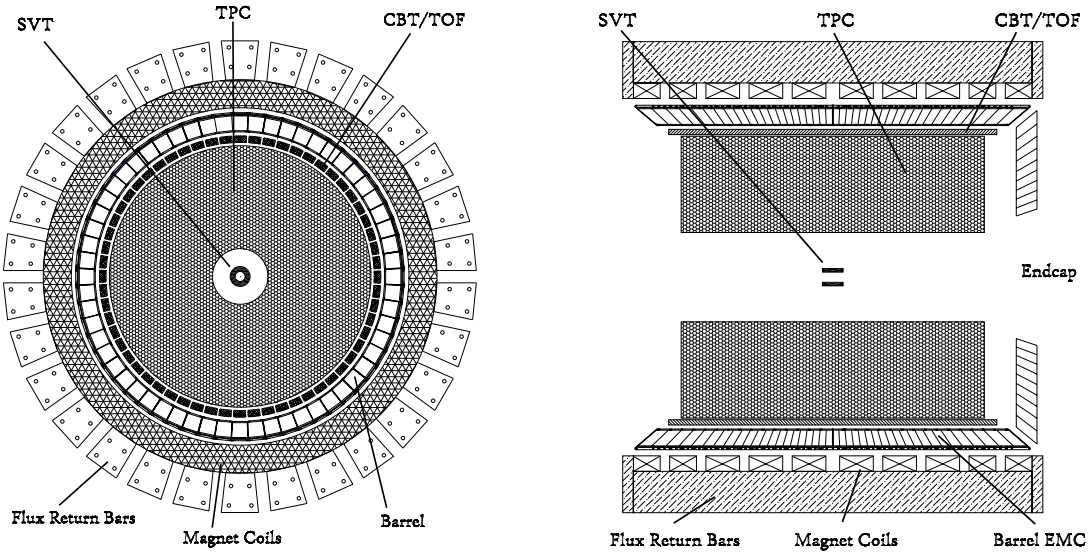

Figure 2.9: Cross sectional views of the STAR detector. The Barrel EMC is located outside the CTB/TOF detector[20].

2.2.4 Central Trigger Barrel

The Central Trigger Barrel (CTB) covers $-1 \leq \eta \leq 1$ and $0 \leq \phi \leq 2\pi$ with 240 plastic scintillators coupled to PMTs and provides measurements of charged particle multiplicity. The detector has a modular design and consists of 120 trays. Each tray covers one unit in pseudo-rapidity and 6 degree in azimuthal angle. The TOF detector, the main subject of this dissertation, replaces the CTB and will provide more detailed and precise measurements of the time and location of charged particles passing through the detector region. A schematic of a prototype CTB tray is shown in Figure 2.12. For the production CTB trays the cooling loop was omitted and the trays were made of aluminum.

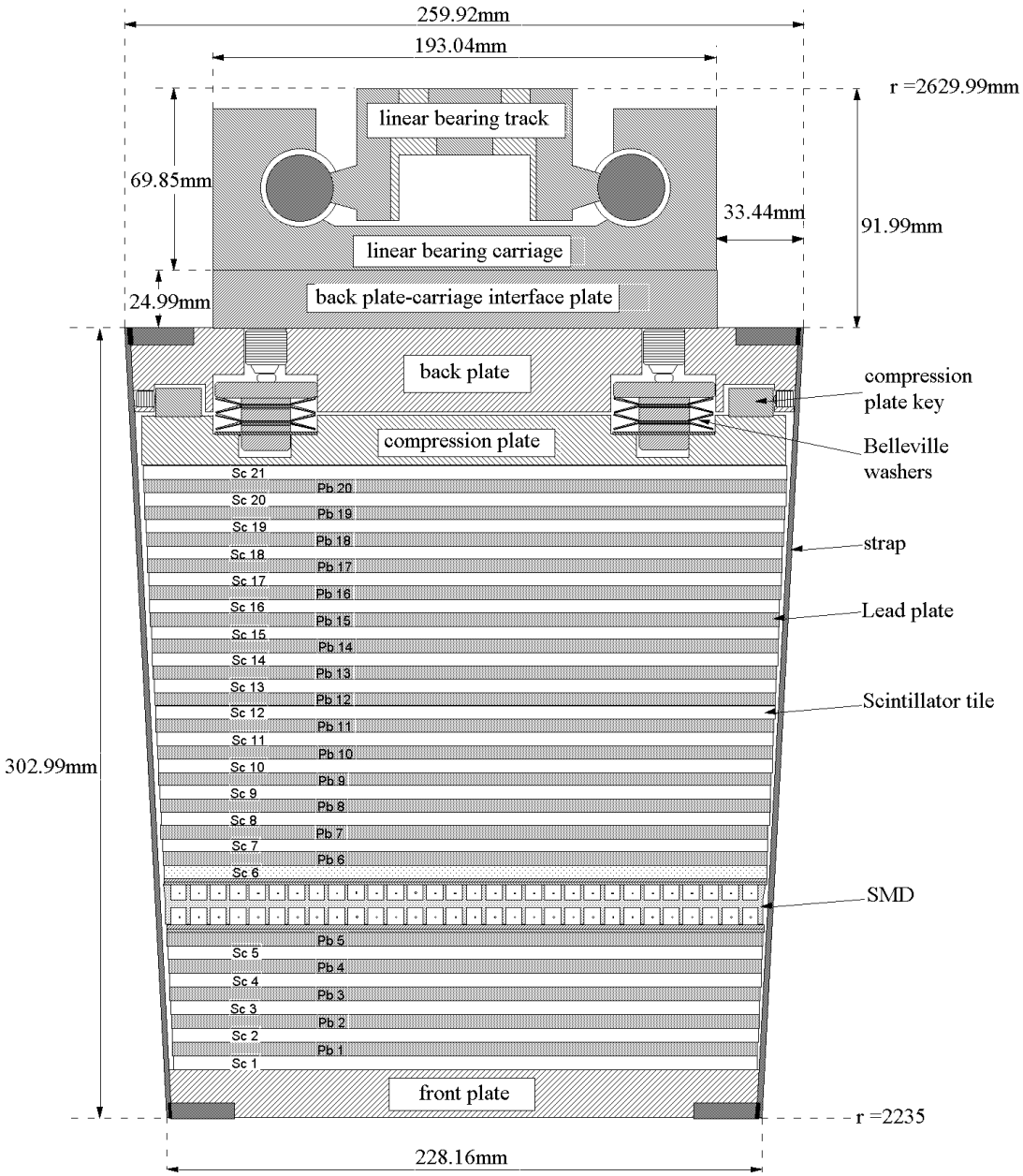

Figure 2.10: Side view of a STAR BEMC module[20].

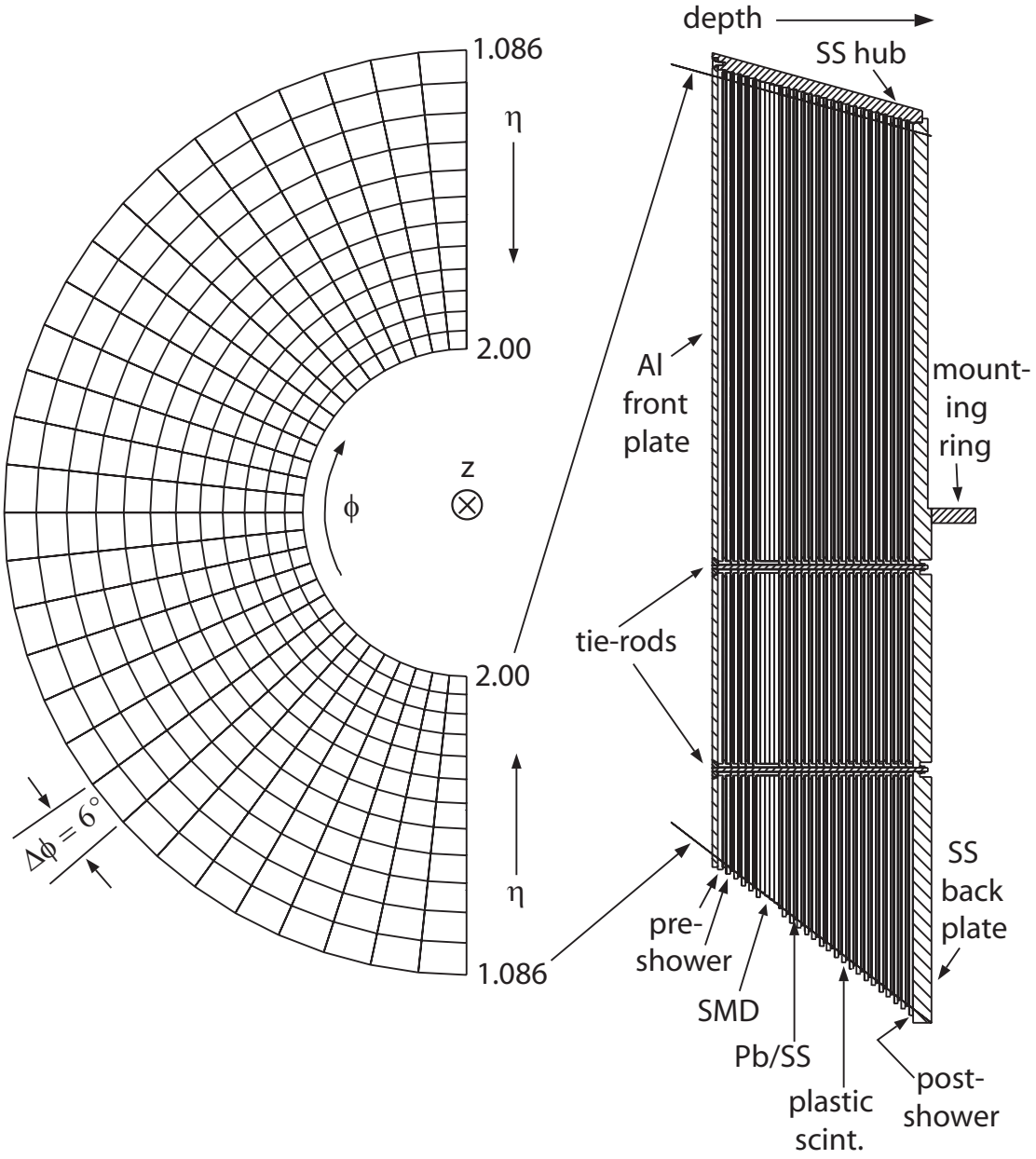

Figure 2.11: Schematic of a STAR EEMC module[21].

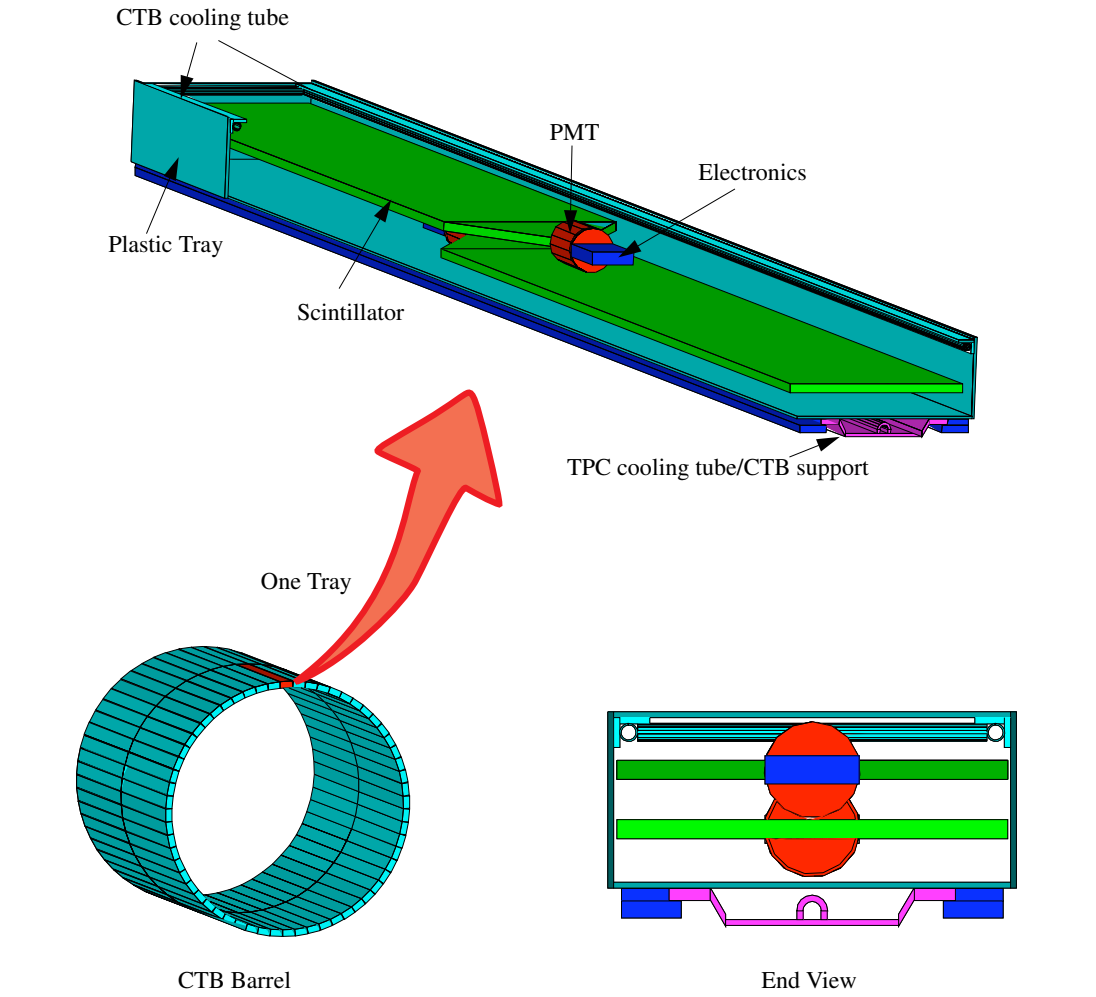

Figure 2.12: Schematic of prototype CTB tray[26].

2.2.5 Beam-Beam Counters

The two Beam-Beam Counters are located 3.5 m from the intersection point and wrap around the beam pipe. Each counter consists of two rings of hexagonal scintillator tiles, as shown in Figure 2.13. The outer ring is composed of large tiles, and the inner ring is composed of small tiles. Both rings are divided into two separate sub-rings of 6 and 12 tiles each.

2.2.6 Photon Multiplicity Detector

The Photon Multiplicity Detector is located outside the east side of the STAR magnet end-cap, 5.5 m from the center of STAR. It covers a pseudo-rapidity range of 2.5–3.5 with full azimuth. It consists of highly segmented gas chambers, filled with Ar+CO_2, behind a lead plate converter. A photon produces an electromagnetic shower when it goes through the converter and the shower particles are detected by the cells. The cells are made from a copper honeycomb wall sandwiched by two PCBs. The wall acts as a common cathode while gold-plated tungsten wires bridged between the two PCBs at the center of each cell act as anodes. Solder-islands, cathode extensions, and signal tracks are printed on the PCBs. A honeycomb of 24×24 cells form a unit module, and 4-9 modules form 12 super-modules. Figure 2.14 shows a schematic of a unit cell and a module layout.

2.2.7 Primary Vertex Position Detector

The pVPD consists of two identical assemblies which are mounted on the beam-pipe-support aluminum I-beam and wrapped around the beam pipe 5.6 m

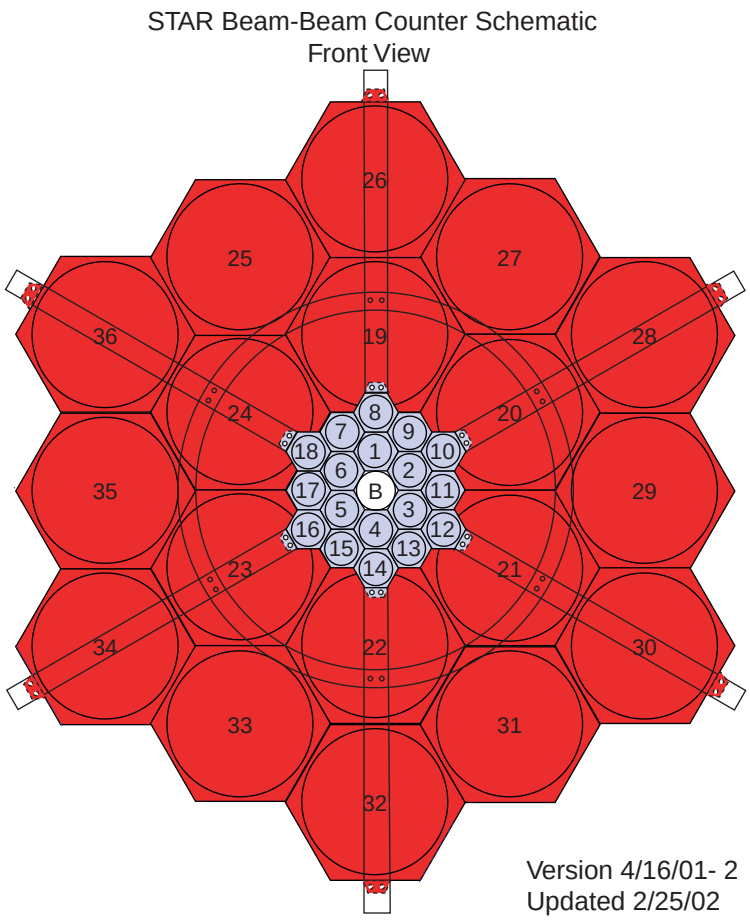

Figure 2.13: Schematic of Beam-Beam Counter[26].

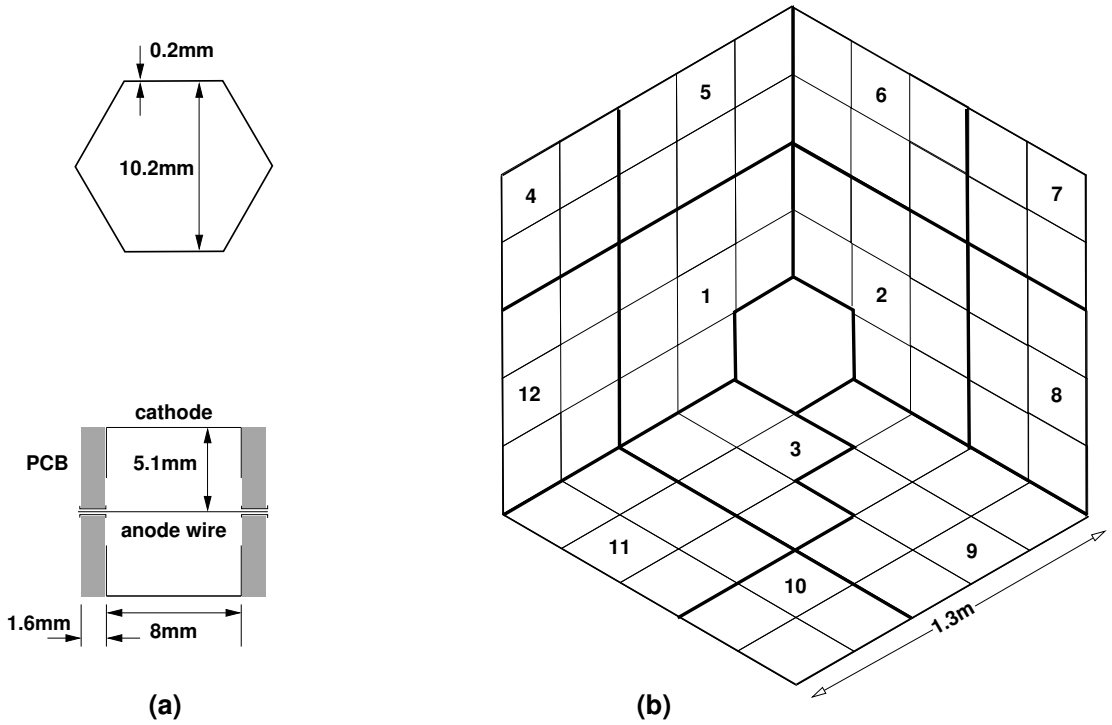

Figure 2.14: (a) Cross-sectional views of unit cell. (b) Layout of PMD modules. Thick lines indicate super-module boundaries. The figures are taken from [22].

from the intersection point. Each assembly consists of a total of 19 PMT units coupled with layers of lead and scintillator in a two ring layout. The inner ring consists of 10 PMTs, and the outer ring consists of 9 PMTs. This latest design of the pVPD detector, also know as upVPD, was installed before Run-6. From Run-2 through Run-5, each side had only 3 PMTs in a single ring layout. The detector was also refered to as *Pseudo* Vertex Position Detector. Figure 2.15 is a picture of the pVPD assemblies.

2.2.8 Foward Pion Detector / Forward Meson Spectrometer

The Forward Pion Detector consists of eight segments of lead-glass colorim; up, down, north and south are 7.5 m from the intersection point relative to the beam pipe on each side of STAR (East and West). The up and down segments consist of 5×5 arrays of lead-glass Cherenkov detectors, and the north and south segments consist of 7×7 arrays [26]. The Forward Meson Spectrometer is an upgrade of the FPD and has 14400 cells in two layers. 756 ($= 37 \times 37 - 20 \times 20$) cells of $5.8 \times 5.8 \times 60\,\mathrm{cm}^3$ lead-glass form the outer shell and 684 ($= 28 \times 28 - 10 \times 10$) cells of $3.8 \times 3.8 \times 60\,\mathrm{cm}^3$ lead-glass form the inner [27]. Figure 2.16 shows the layouts of the two detector systems.

2.2.9 Zero Degree Calorimeters

On both sides of STAR, a pair of ZDC detectors are installed 18 m from the intersection point. They are located outside of the DX dipole magnets, the magnets that split and merge the two colinear beams as the beams pass through

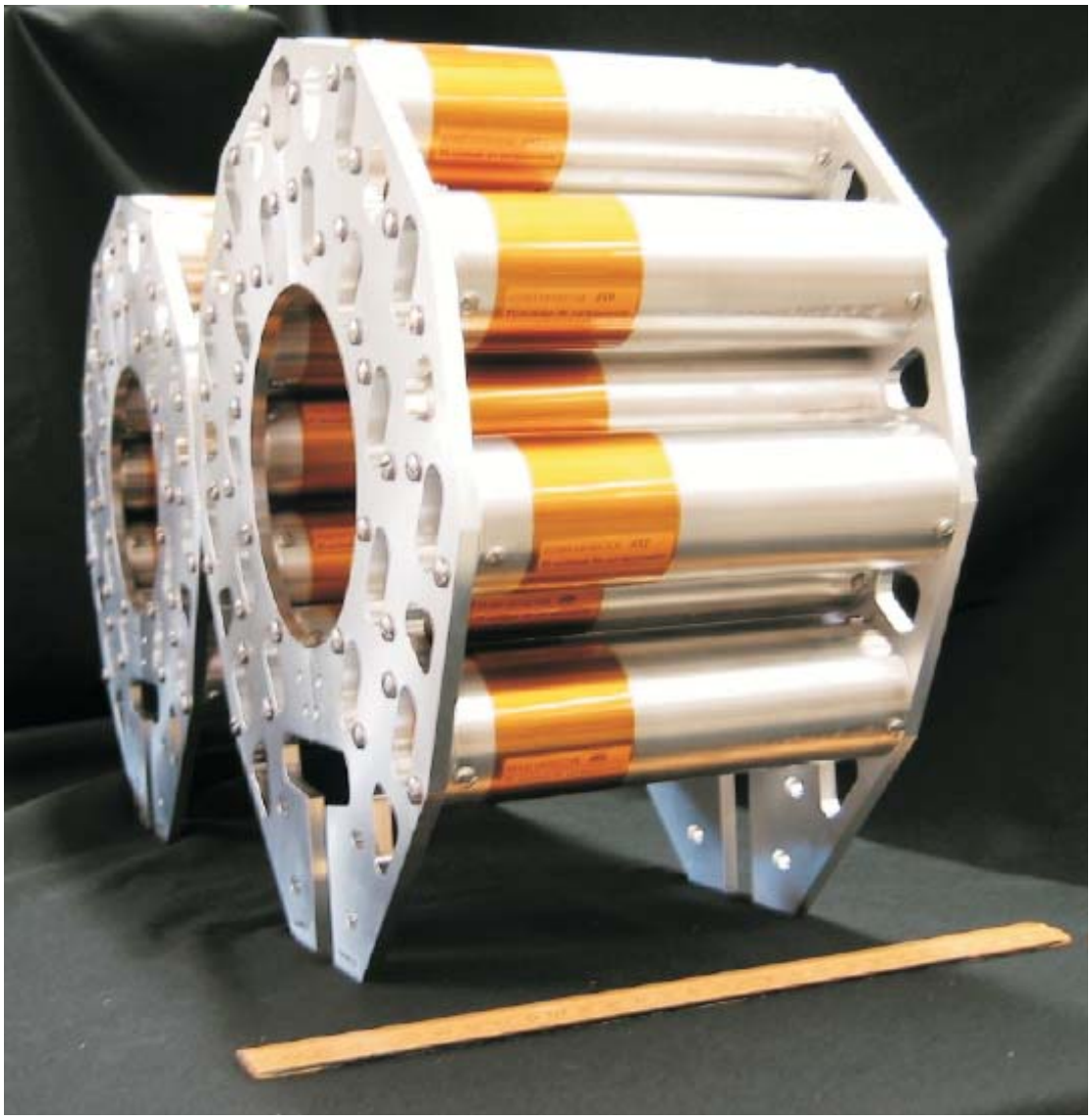

Figure 2.15: Picture of pVPD assemblies.

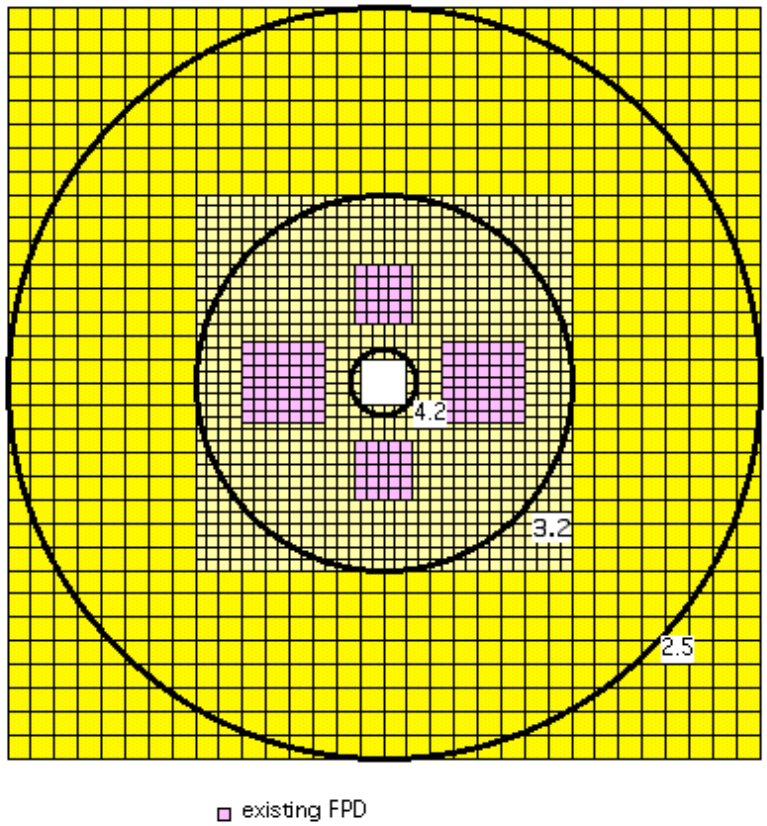

Figure 2.16: Cross-sectional schematic of FPD and FMS. The circles represent contour in pseudo-rapidity[27].

the intersection region. Because the DX dipole magnets bend charged particles away from the straight line which leads to the ZDC detectors, the ZDC only detects neutral spectator neutrons. The configuration of the ZDC detector is shown in Figure 2.17. Each ZDC consists of three modules and each module consists of a series of tungsten plates alternating with layers of wavelength shifting PMMA fibers connected to PMTs. The Cherenkov light created in the tungsten plates leads to the PMTs via the fibers. The mechanical design is show in Figure 2.18. The ZDC measurements of the spectator neutrons are used for beam monitoring, collision triggering, and measuring the centrality (an estimate of the impact paramter) of individual collisions [28, 24].

2.2.10 Trigger

The STAR Trigger consists of multiple levels of logic, Level 0 to Level 2, implemented by a set of VME modules, NIM modules, and Linux CPUs, to decide whether it accepts the event and records the readouts for every RHIC crossing. The decision is made based on trigger data from trigger detectors including ZDC, BBC, pVPD, CTB, EEMC, BEMC, and FPD. The data from the fast detectors are sent in the form of digital signals to the Data Storage and Manipulation Board (DSM)[29, 26]. The geometry of these detectors are shown in Figure 2.19.

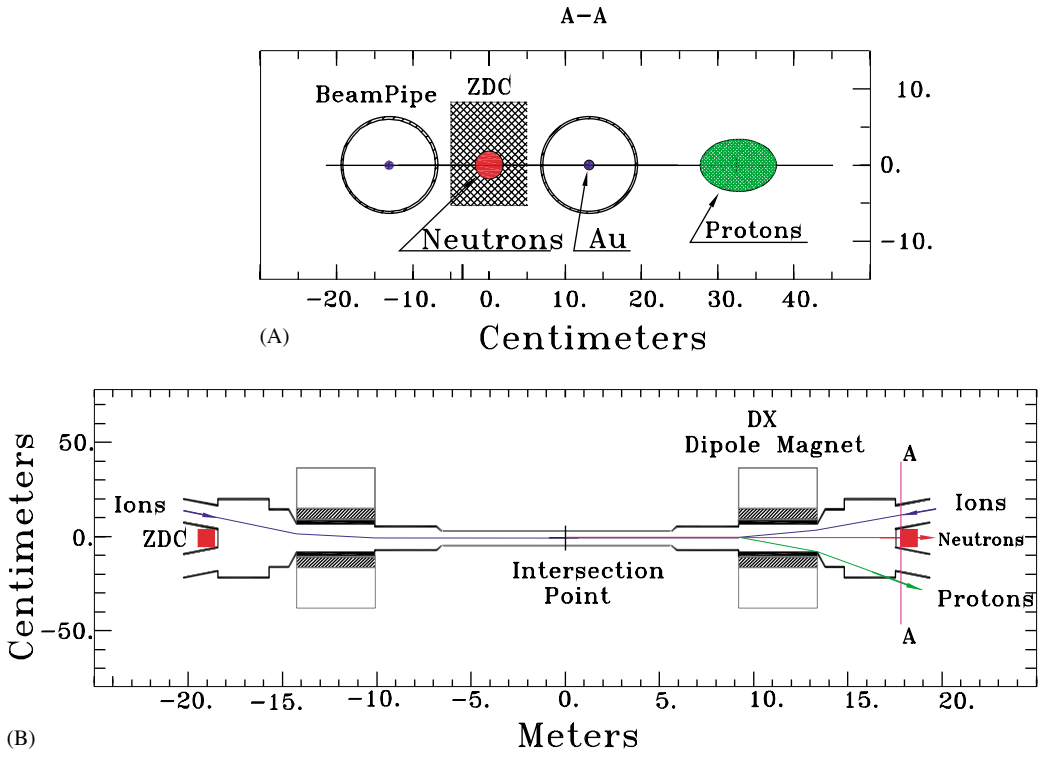

Figure 2.17: (A) Only neutral particles are seen by the ZDCs. (B) Location of the ZDC detectors[28].

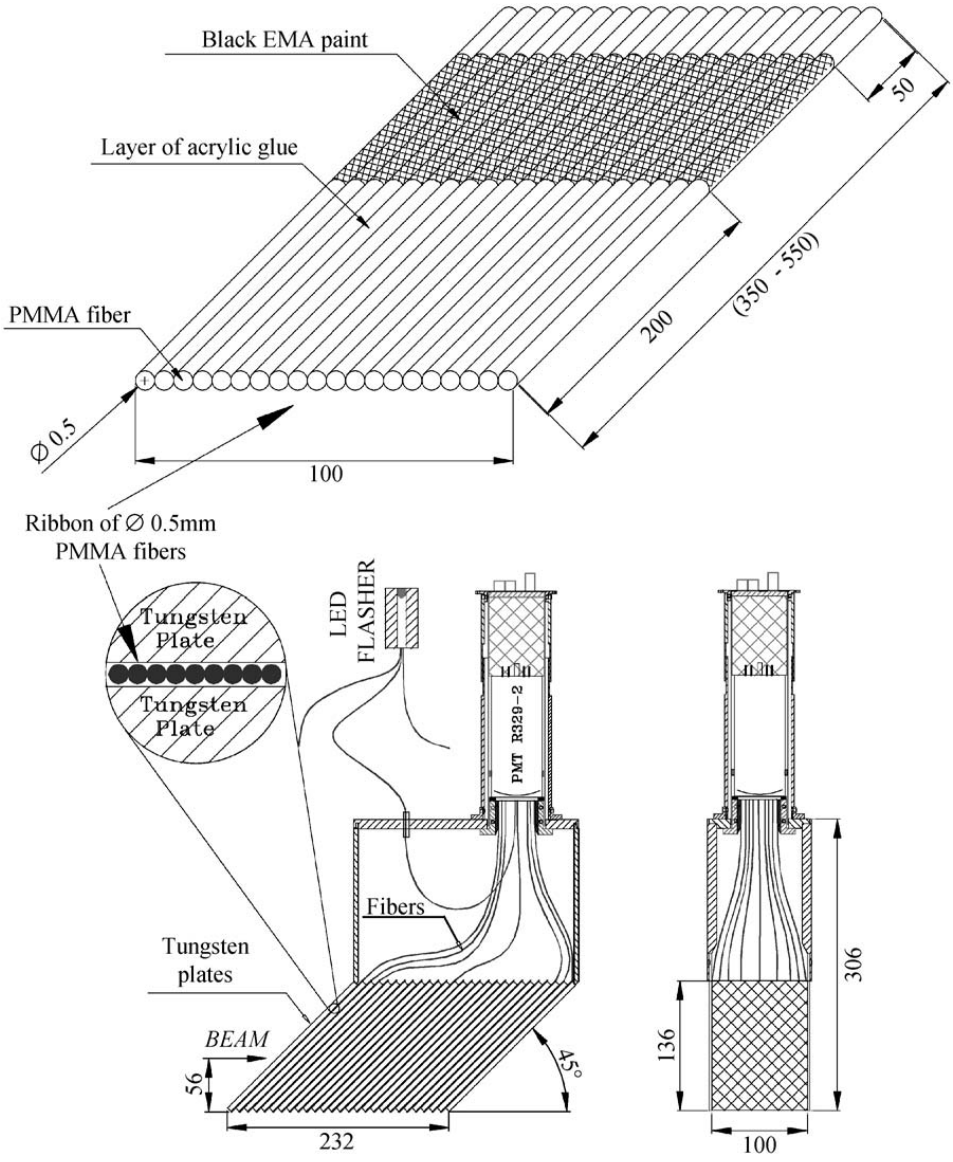

Figure 2.18: Mechanical design of the ZDC detectors[24].

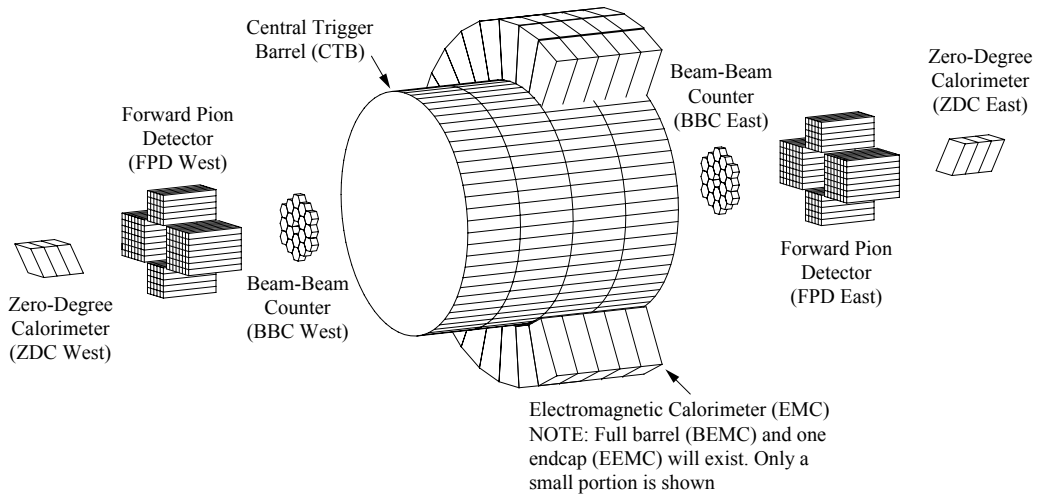

Figure 2.19: Schematic of trigger detectors. The pVPD is not shown in the figure[26].

Chapter 3

The STAR Time of Flight Detector

The purpose of the Time of Flight (TOF) detector upgrade is to enhance the upper transverse momentum (p_T) limit of STAR particle identification (PID) over a large acceptance (2π in azimuthal angle and $|\eta| \leq 1.0$ in pseudo-rapidity) [8]. The design is based on the relatively inexpensive technology of the Multi-gap Resistive Plate Chamber (MRPC) [30] which was developed recently at CERN for the ALICE detector at the LHC.

After significant research and development, construction of the detector began in November 2006 and was completed in May 2009. Several iterations of prototype trays were tested at the AGS and RHIC since 2001. The first 5 production trays were installed in Fall of 2007 before RHIC Run-8, and an additional 89 trays were installed during the break before Run-9. The full 120 trays will be installed before the start of Run-10 (year 2010).

In the following sections the STAR TOF design will be reviewed, and the technological developments for TOF will be discussed.

3.1 Detector Design

The TOF system measures the time interval Δt that it takes a charged particle to pass between two spacial points along its flight path. The first time, the "start time," is determined by the two STAR pVPDs, and the second time, the "stop time" is determined by the barrel TOF detector. These two detectors are often referred as "start side" and "stop side" according to their functionality.

Each pVPD assembly consists of 19 PMTs coupled to scintillators. The assemblies are mounted very close to the beam pipe about 5 m from the intersection point ($z \sim \pm 5$ m) on both the East and West sides of STAR. They detect forward moving charged fragments from the collision. Because most of the fragments are spectators (not directly involved in the collisions) they move at very high speeds, almost the speed of light. In principle the start time can be determined from one pVPD measurement, but in practice both pVPDs are used to best determine the start time.

The barrel TOF detector (stop side) consists of 120 trays that form a cylindrical outer shell around the STAR TPC; it covers the full azimuthal angle and the range $-1 < \eta < 1$ in pseudo-rapidity. Each TOF tray covers 6 degrees in azimuthal angle and one unit of pseudo-rapidity ($-1 < \eta < 0$ or $0 < \eta < 1$). The shape of a TOF tray is almost identical to that of a CTB tray. A TOF tray box is 95" (241.3 cm) long, 8.5" (21.6 cm) wide, and 3.5" (8.9 cm) high. The tray contains 32 MRPC modules (inside) and 17 onboard electronics boards (outside). It is gas-tight and filled with R134a (freon) that flows during operation. Figure 3.1 shows the inside of a TOF tray, and Figure 3.2 shows a tray's onboard electronics.

Each of the trays 32 MRPC modules has 6 pads for a total of 192 channels per tray. The full barrel TOF detector with its 120 trays thus has 23,040 channels. When a charged particle passes through any given pad, a signal is generated that determines the stop time t_1. Combining measurements from the start and the stop side provides the "time-of-flight" interval $\Delta t = t_1 - t_0$.

The hits at the stop side detector are matched to reconstructed tracks from the STAR TPC. Using the momentum, p, and track length, Δs, of the associated track from the TPC, there is sufficient information to calculate the average value of the inverse velocity, $1/\beta$,

$$\frac{1}{\beta} = c\frac{\Delta t}{\Delta s} \ , \tag{3.1}$$

where c is the speed of light, and the mass of the charged particle, m, is given by

$$m = \frac{p}{\gamma\beta c} = \frac{p\sqrt{1-\beta^2}}{\beta c} = \frac{p}{c}\sqrt{\left(\frac{1}{\beta}\right)^2 - 1}. \tag{3.2}$$

This measurement of the particle's mass is the basis of particle identification (PID) determined by TOF. Note that oppositely charged particles are distinguishable in the TPC from the direction of helical tracks. Therefore, for example, π^+ and π^- are distinguishable.

Since the velocity of a particle converges to the speed of light as the momentum goes to infinity, particle identification becomes more difficult at higher particle momenta. This can be seen more explicitly by looking at the error propagation of the TOF reconstructed mass,

$$\frac{\delta m}{m} = \gamma^2\frac{\delta p}{p} \oplus \frac{\delta(\Delta t)}{\Delta t} \oplus \frac{\delta(\Delta s)}{\Delta s}. \tag{3.3}$$

Figure 3.1: Picture of 2 TOF trays. Each tray contains 32 MRPC modules. The white wires comprise the high voltage bus.

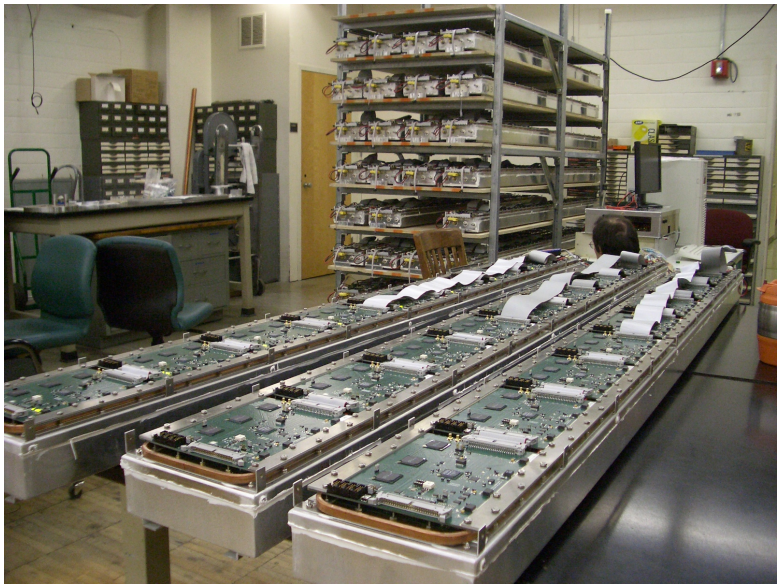

Figure 3.2: Picture of TOF trays being prepared for shipment to BNL. The flat ribbon cables connect the TDIGs with the TCPU. The TDIGs mount on top of the TINOs and a rectangular copper cooling loop is sandwiched between TDIGs and TINOs. An aluminum cover will be installed to protect electronics from RF noise and mechanical damage.

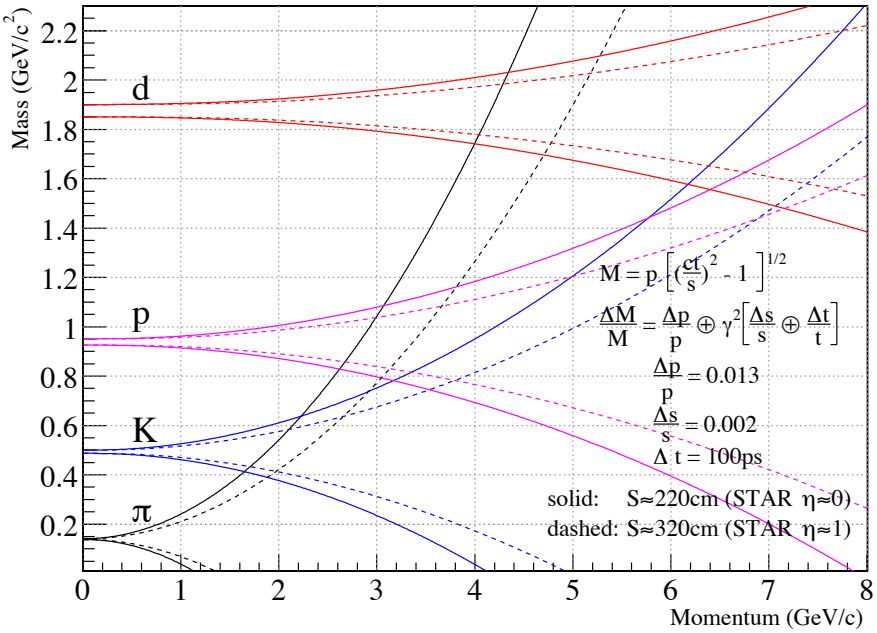

Figure 3.3: The momentum dependence of the mass resolution. Two lines correspond to two edges of TOF tray. Parameters used for the estimation are shown on the graph. Figure is taken from [8].

The factor γ^2, which diverges as the velocity goes to the speed of light, magnifies the error contribution substantially at high momenta. The other contributions to the mass resolution are estimated to be approximately $\delta p/p = 1.3\%$, $\delta s/s = 0.2\%$, and $\delta t = 100$ ps and are shown in Figure 3.3. Two different lines, solid- and dashed-line, are given for each particle speces and represent the approximate minimum and maximum errors depending on the particles' path lengths.

3.2 Multi-gap Resistive Plate Chamber (MRPC)

An MRPC module is a sandwich of two honeycomb boards, two graphite electrode plates, two outer glass plate, 5 partitioned glass plates separated by thin fishing lines, and 2 laminate boards containing 6 copper pads each.

Supplying an appropriate high voltage between the pair of electrodes allows the module to operate in what is known as the avalanche mode. The layers of glass plates divide the gas gaps into smaller sections, making several small avalanches; this technique improves the timing resolution of the module. Side views of the MRPC module are show in Figure 3.4, and the pattern of copper read-out pads for the module is shown in Figure 3.5. Figure 3.6 is a photograph of an MRPC module.

3.3 Electronics Design

The time of flight system requires high precision time digitization at two separate locations. Because of the high radiation enviroment inside the collider and the the large size and number of channels comprising the TOF detector, it is not possible to simply send logic signals via long cables into an integrated system. The STAR TOF design, therefore, uses a distributed electronics system. At both the start and stop sides, signals are digitized relative to a common clock instead of atteempting to digitize a stop time relative to a start time for each collision.

A series of custom made electronics boards were developed and built to carry out this distributed system design. The top-level diagram of the electronics

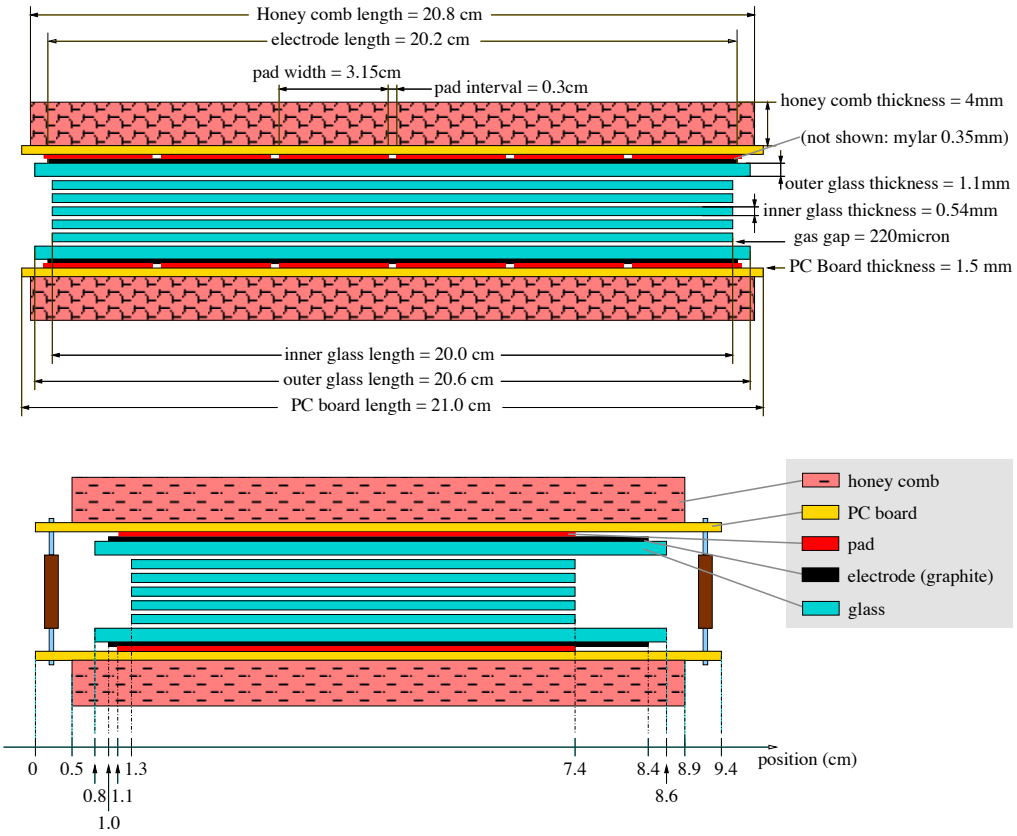

Figure 3.4: Two side views of the MRPC module. Figure is taken from [8].

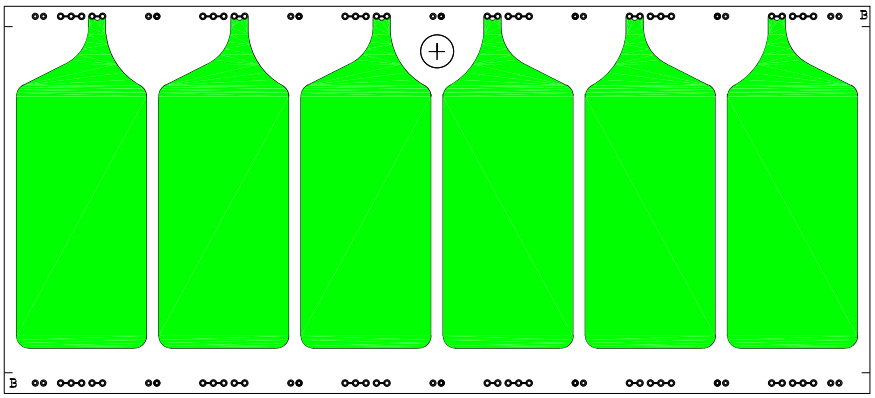

Figure 3.5: The circuit board with the copper read-out pads for the MRPC module. Figure is taken from [8].

chain is shown in Figure 3.7. During the R&D phase, some electronics boards were upgraded and renamed. TFEE was renamed TAMP before finally settling on TINO in the production design. Likewise, TFEEb was changed to TPMT and later to TPMD, and TMIT is now called THUB. Each electronics board is discussed in more detail in the following subsections.

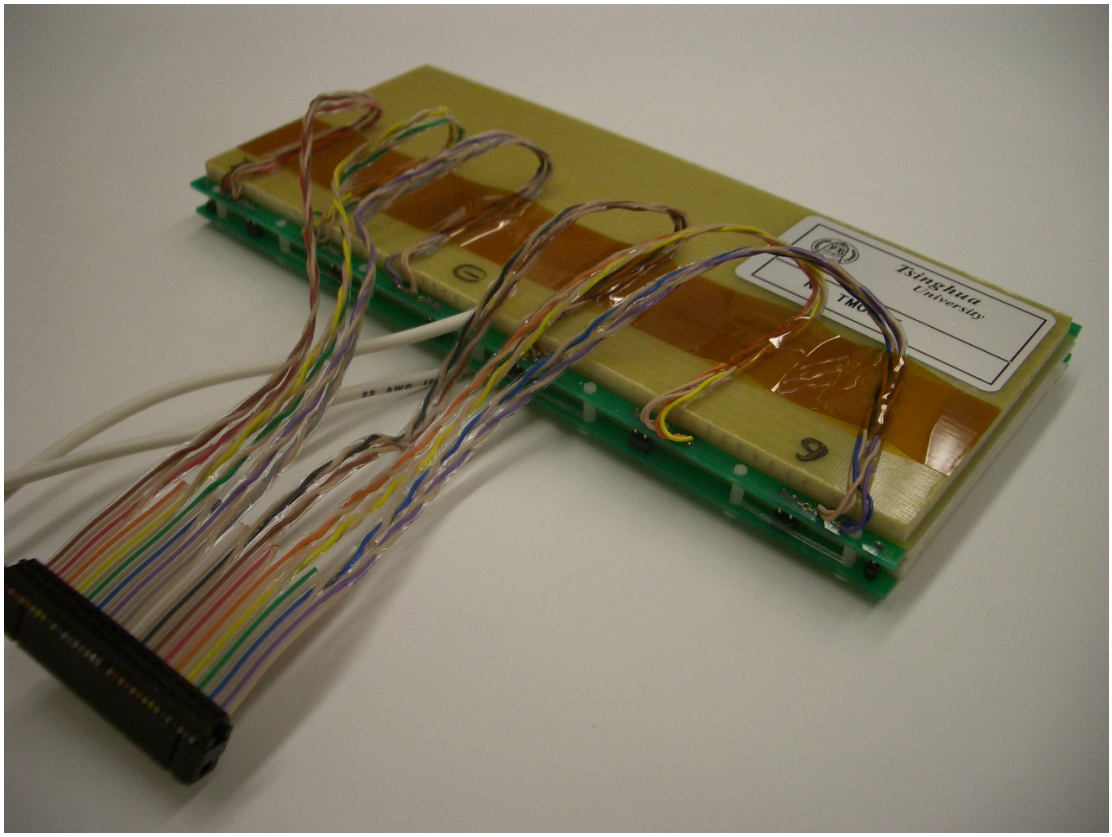

Figure 3.6: Picture of MRPC Module.

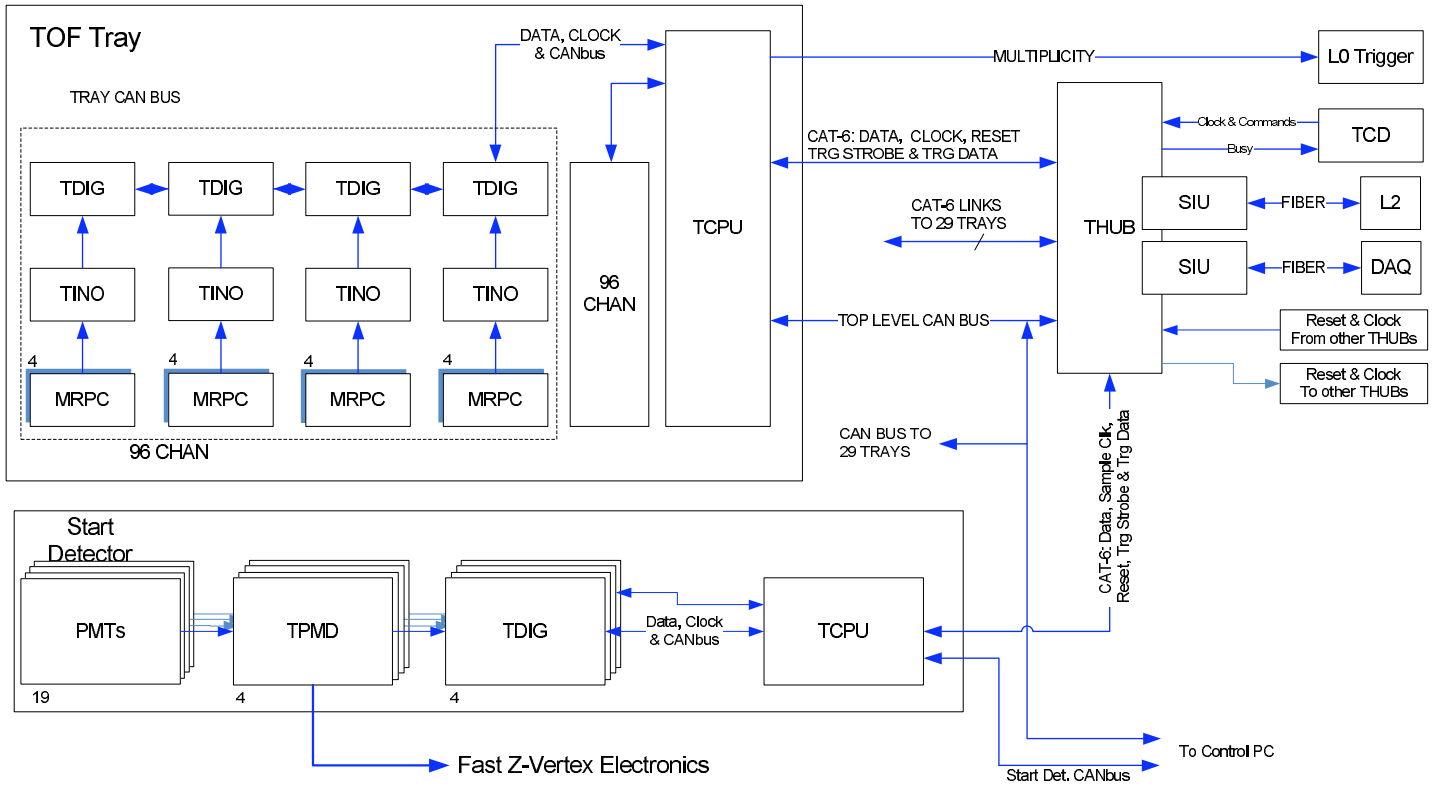

Figure 3.7: Block diagram of top level signal stream.

3.3.1 TFEE

This was the first generation front-end electronics board for the MRPC. The board performed amplification functions for the signals picked up from the copper pads and provides discriminator functionality using a MAXIM 3760 preamplifier and AD96685 comparator. While the original design specification was for 24 channels, which would accommodate signals from 4 MRPC modules, a 6-channel version of TFEE was produced for the prototype TOF tray, TOFr. This prototype board also had additional functions such as amplified analog output and NIM logic signal output that would not be implemented in production. In the first generation cosmic ray test stand, we used this version of the TFEE. Both types of signals, analog and digital are sent to a DAQ system and processed by ADCs and TDCs respectively. Figure 3.8 shows a prototype TFEE.

3.3.2 TFEEb

TFEEb is a modified version of the TFEE. The board accepts input signals from a PMT instead of a MRPC. This modified board was developed specifically for the start side and allowed for identical signal processing chains to be used on both the start and stop side detectors.

3.3.3 TAMP

This interface board which is located between the MRPC tray and the TDIG is a new design of the TFEE. It amplifies the MRPC signals. Each TAMP card handles four 6-channel MRPC modules. In total, there are 960 TAMP cards.

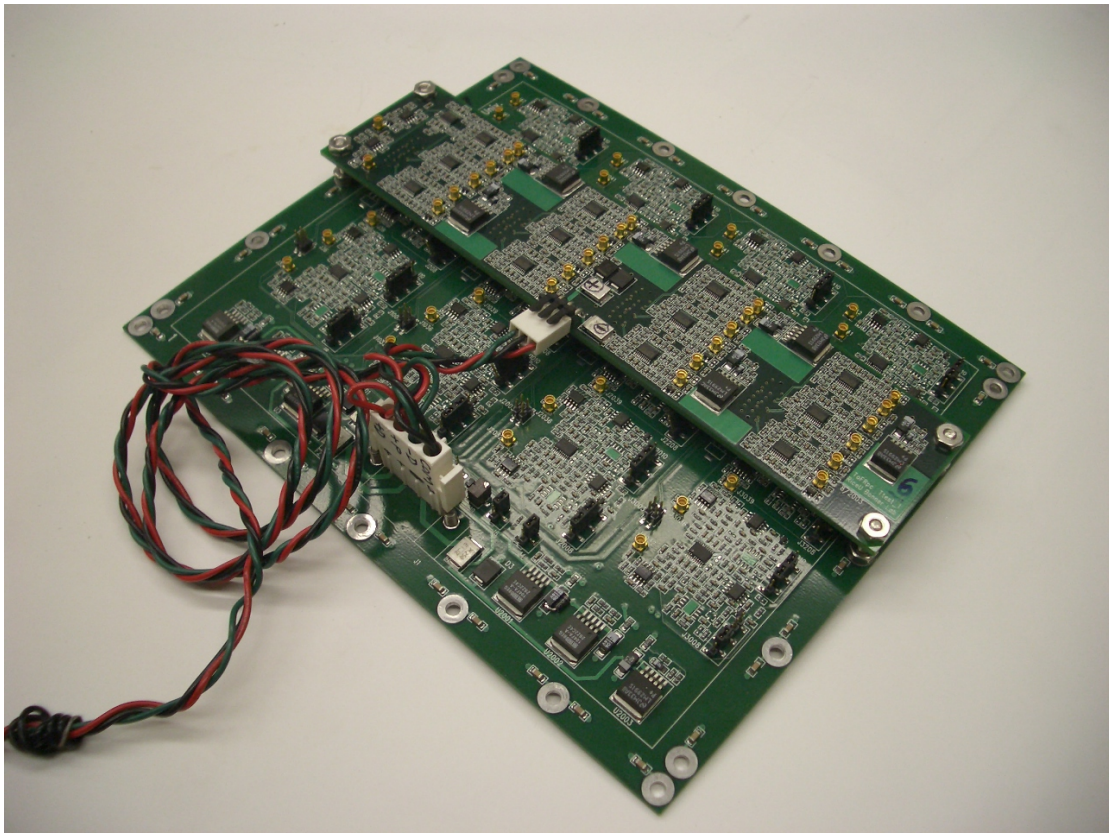

Figure 3.8: The TFEE prototype.

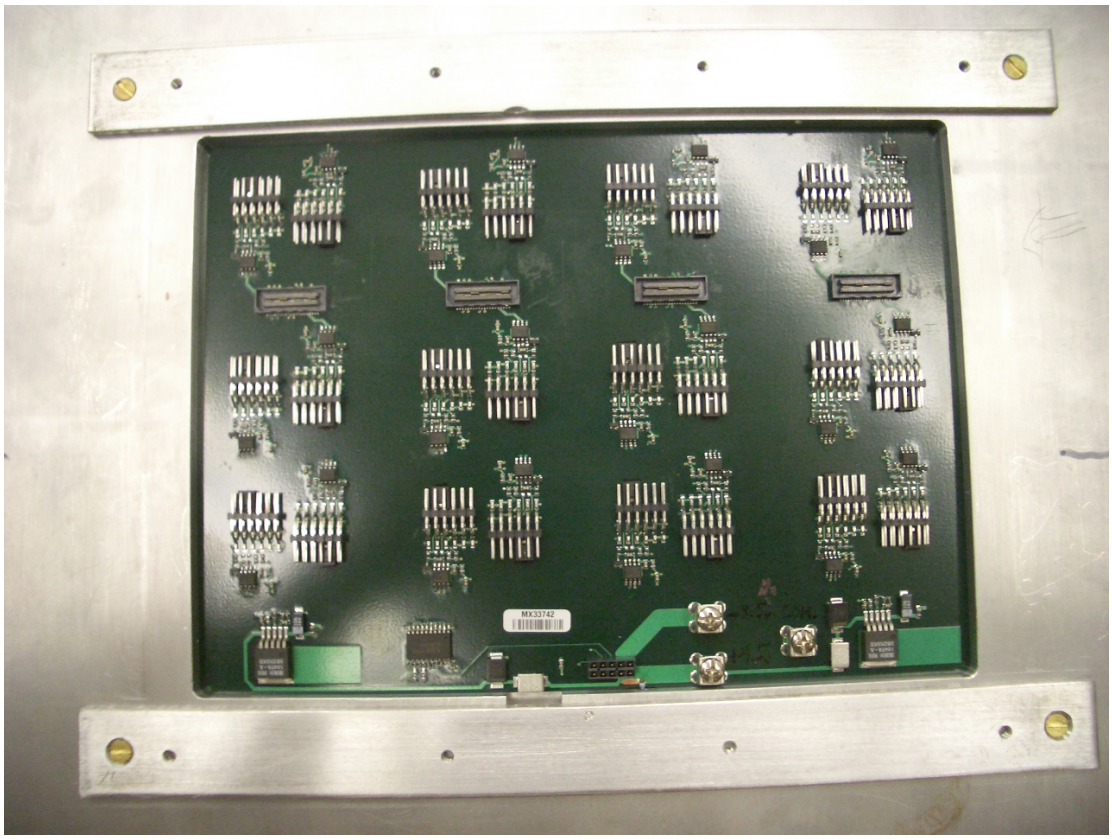

Figure 3.9: The TAMP prototype.

The Maxim 3664 preamplifier is still located on this board, but the Maxim 9601 comparator wass moved to the TDIG board.

3.3.4 TINO

The TINO is the final iteration of the front-end electronics card for the MRPC. Unlike the previous designs, it uses a custom NINO ASIC [31] instead of a combination of commodity products. The NINO was developed at CERN for a

similar TOF system being built for the ALICE experiment. The decision to use this relatively low cost and low power chip was reached in Feb 2006 based on its performance during cosmic ray testing that took place at UT. The raw signal is fed into a discrimiator with a specific threshold, and as the threshold is crossed by the raw signal, logic signals are transmitted to the TDIG card for digitization. Trailing edge signals are delayed by the TINO so that the TDIG can input both signals into a single channel. A block diagram and a picture of TINO are shown in Figure 3.10 and Figure 3.11 respectively.

3.3.5 TDIG

The TDIG board processes leading and trailing edge timings for sets of 4 MRPC modules (24 detector channels). These cards are mounted directly onto the TINO (previously TAMP or TFEE) boards - 8 pairs of TDIG/TINO boards for each tray. The primary inputs to the TDIG board are the discriminator signals, clock, multiplicity gate, and L0 trigger readout commands, while the timing data of the hit edges and the 5-bit partial multiplicity sums are created as outputs.

The board has 3–4 HPTDC ASICs developed at CERN for the ALICE and CMS experiments [32]. At the early stages of development, the leading edge timing for the 24 channels was done using 25 ps bins that were provided by the 3 HPTDC devices while operating in 8 channel “very hi res mode”. The trailing edges of all 24 channels were determined by 1 device operating in a 32 channel “hi res mode ” that used 100 ps time bins. In the production design, the leading and trailing edges of 24 channels are all digitized by 3 HPTDC devices operating

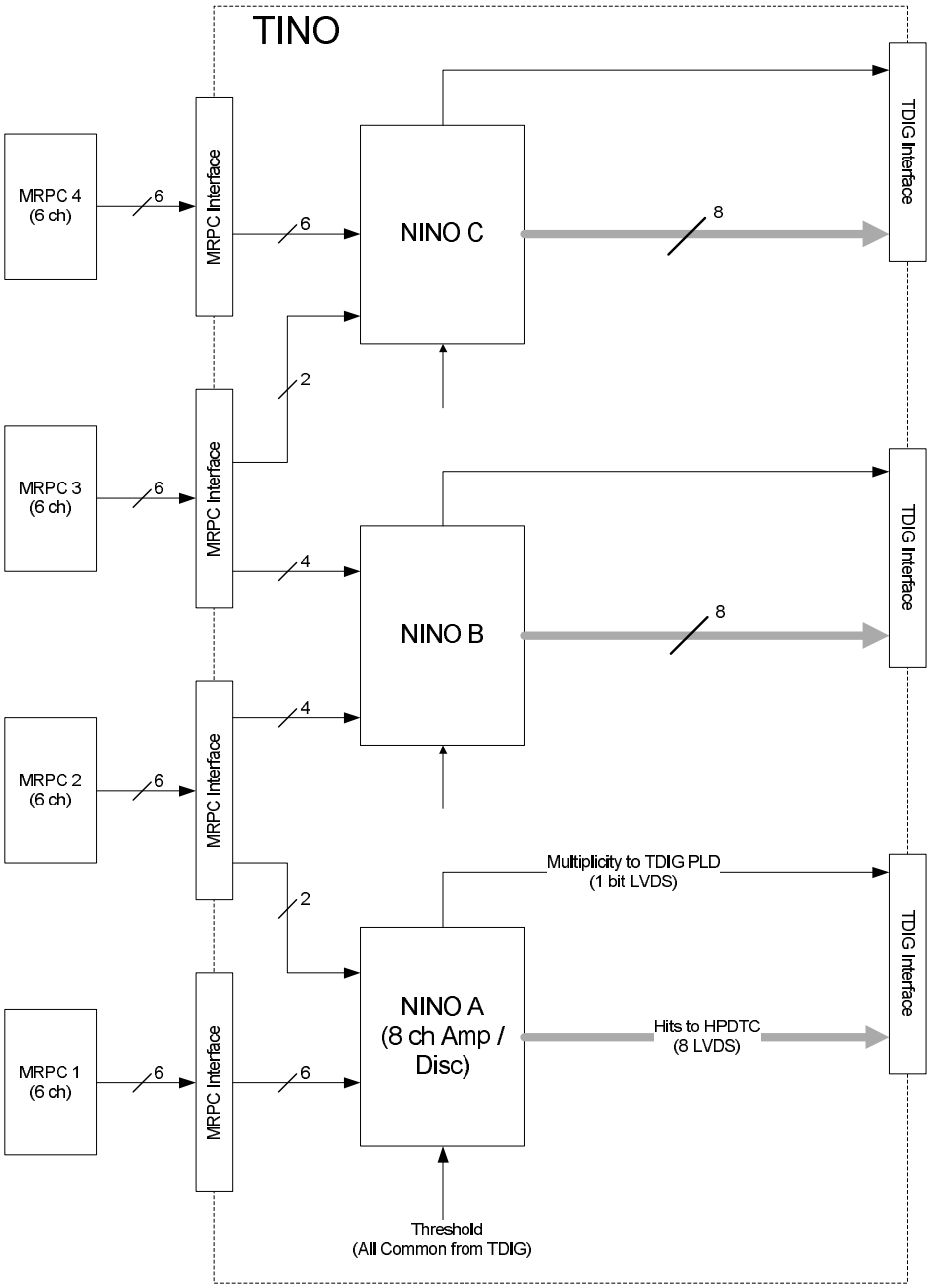

Figure 3.10: Block diagram of TINO.

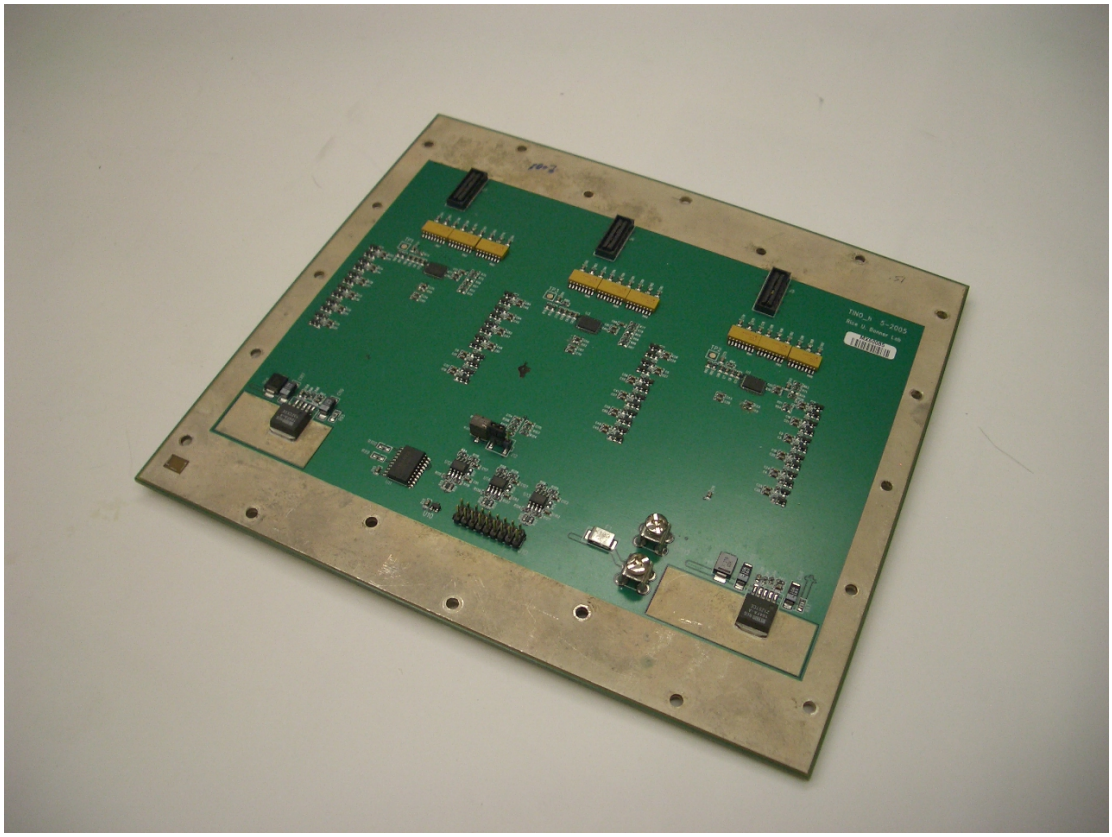

Figure 3.11: Picture of TINO.

in “very hi res mode”. In order to achieve this simplification, the discriminator signals of trailing edges had to be delayed at the TINO board.

To communicate the TDIG’s output, a built-in hardware handshake protocol is used. It allows for the 16 HPTDC devices to share a 80 Mbit/sec serial output port so that only 2 data cables are required per TOF tray (4 TDIG boards, 96 MRPC pads each). Additionally, this board has a slow serial interface which is used for HPTDC and logic configuration, control of the discriminator threshold, and temperature monitoring. A top level block diagram of TDIG is shown in Figure 3.12. Figure 3.13 is a picture of the latest version of TDIG.

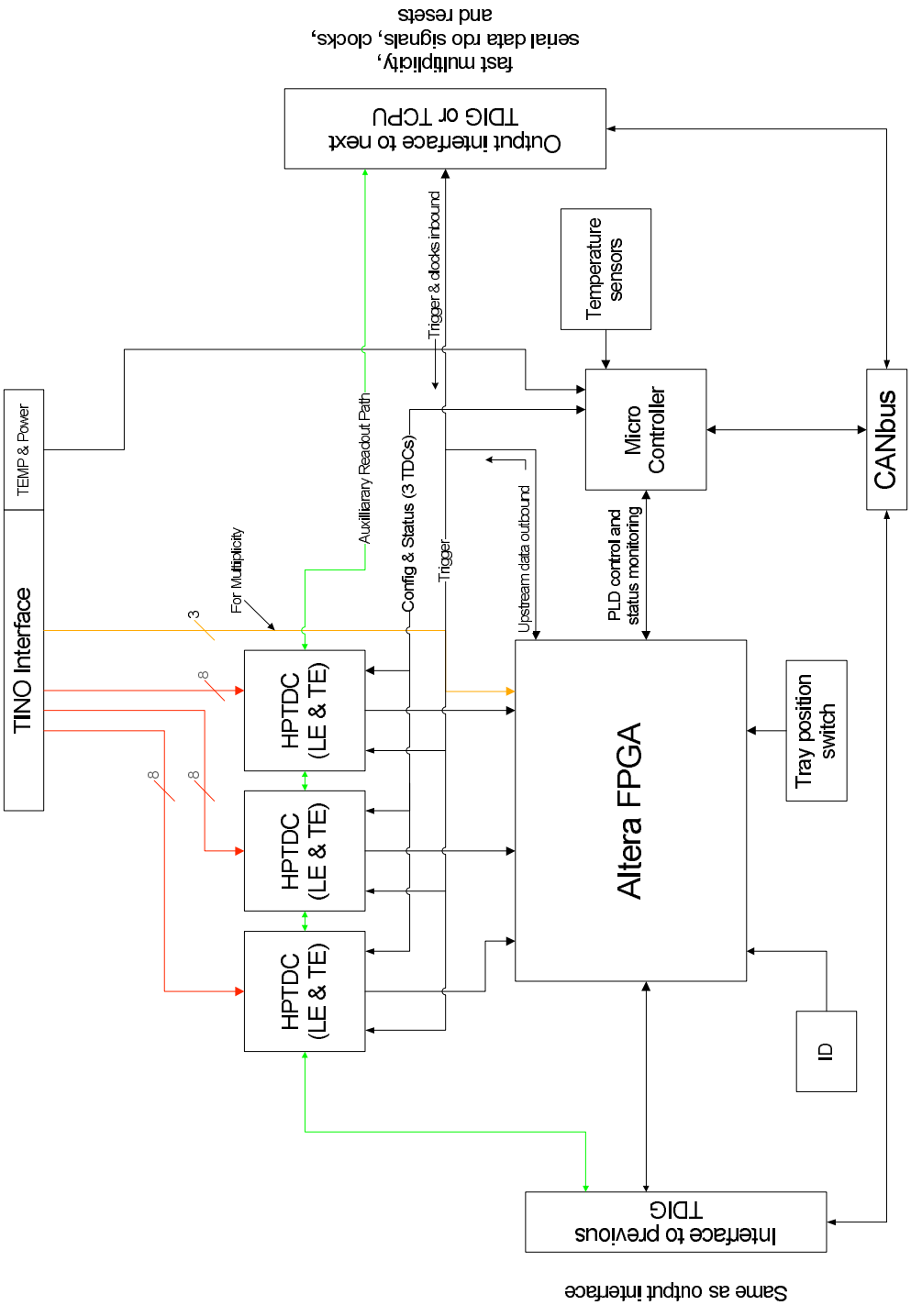

Figure 3.12: Top level block diagram for TDIG.

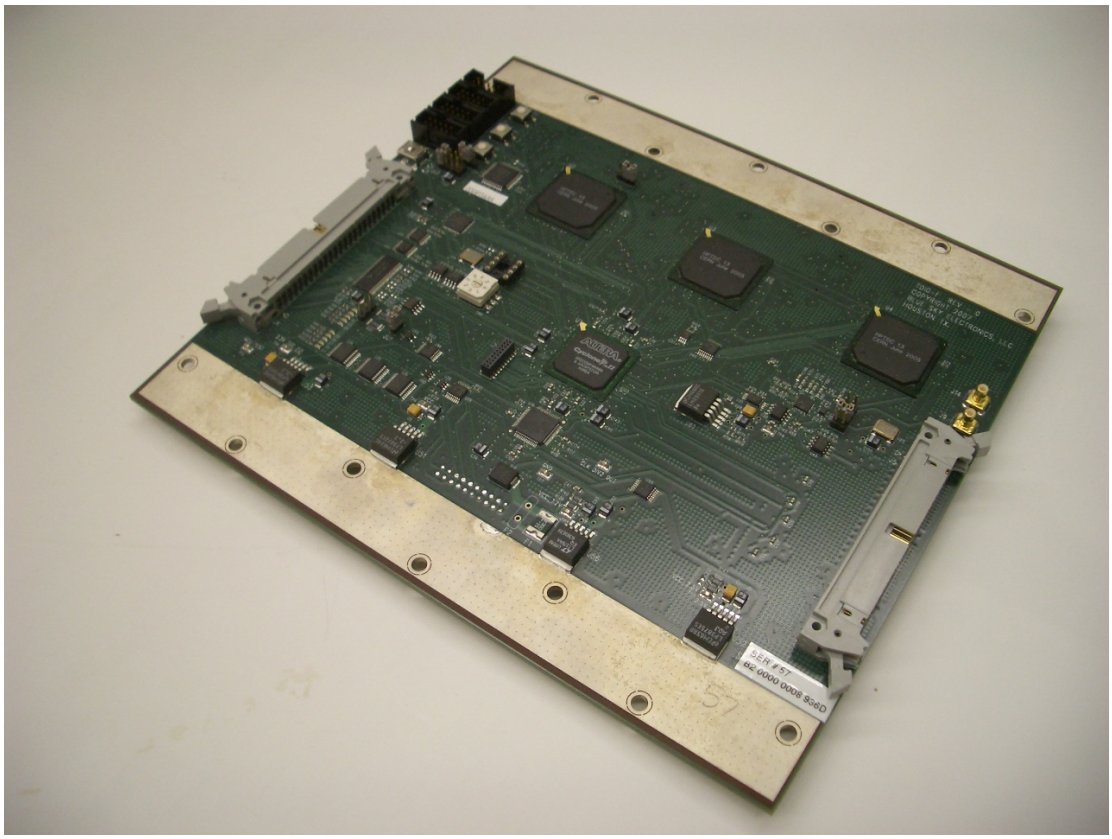

Figure 3.13: Picture of TDIG.

3.3.6 TPMT/D

The TPMT and TPMD are new generation front-end boards for the start side detectors. Their basic functionality is equivalent to that of the original TFEEb design: receiving input signal from PMT, discriminating it with a fixed value threshold, and sending the output logic signal to TDIG. Figure 3.14 shows a top level block diagram of TPMT, and Figure 3.15 shows a picture of TPMD.

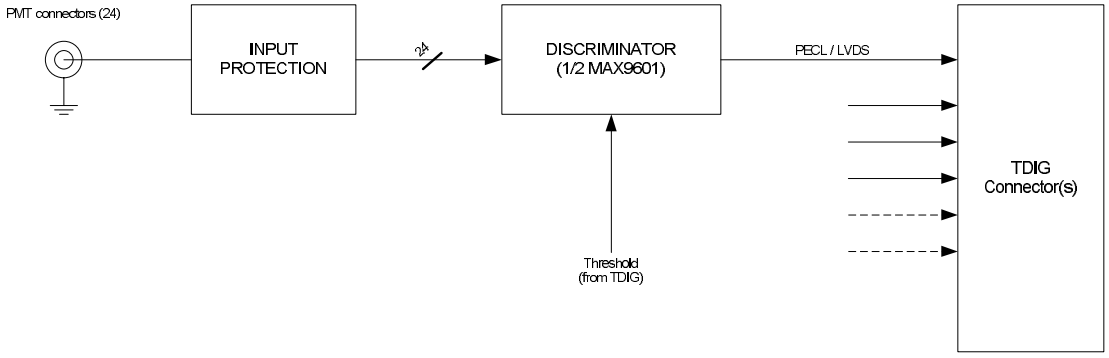

Figure 3.14: Top level block diagram of TPMT

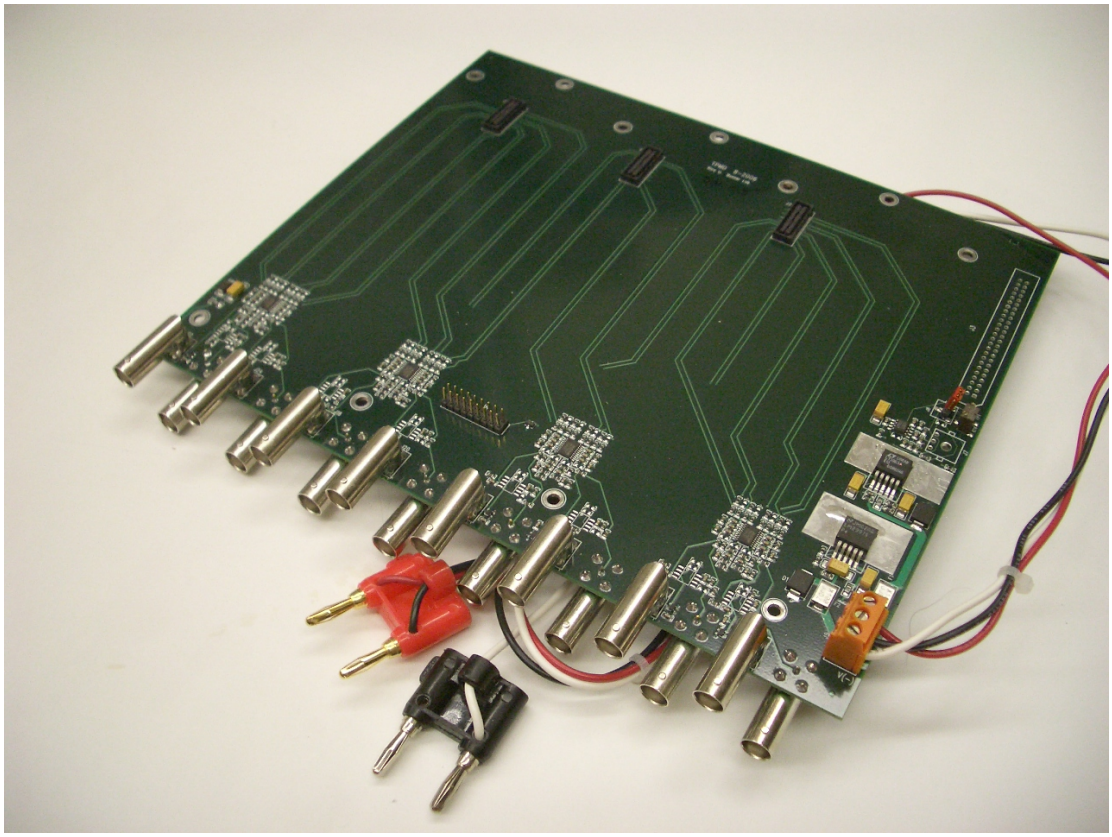

Figure 3.15: Picture of TPMD

3.3.7 TCPU

The TCPU board acts as a data collector at the tray level and is an interface between the TDIG boards and THUB. There are 120 TCPUs on the stop side, one for each TOF tray, and 2 TCPUs on the start side, one for East and one for West. The TCPU board communicates with TDIGs via two bus cables, in which up to 4 TDIGs can be daisy chained. The TCPU itself is on a CAN-bus network and provides gateway functionality for the TDIGs. Figure 3.16 is a top level block diagram of TCPU. Figure 3.17 shows a picture of the latest version of TCPU. The TCPU performs the following functions.

- **Multiplicity** – Calculates the total number of hits from all 8 TDIG channels and sends them to the STAR Level 0 trigger.
- **HPTDC readout** – Provides readout signals from the 32 HPTDCs on the tray. It receives data from the TDCs, buffers the data, formats it, and then sends it out to the THUB via SerDes connection.
- **System management** – Receives from the CAN-bus network configuration information for the TCPU and TDIG boards. The configuration information includes TCPU mode selection, discriminator threshold values and settings parameters for the HPTDCs. The information can be applied to the current setting or stored in the EEPROMs on the TDIGs to be loaded during a later boot stage.

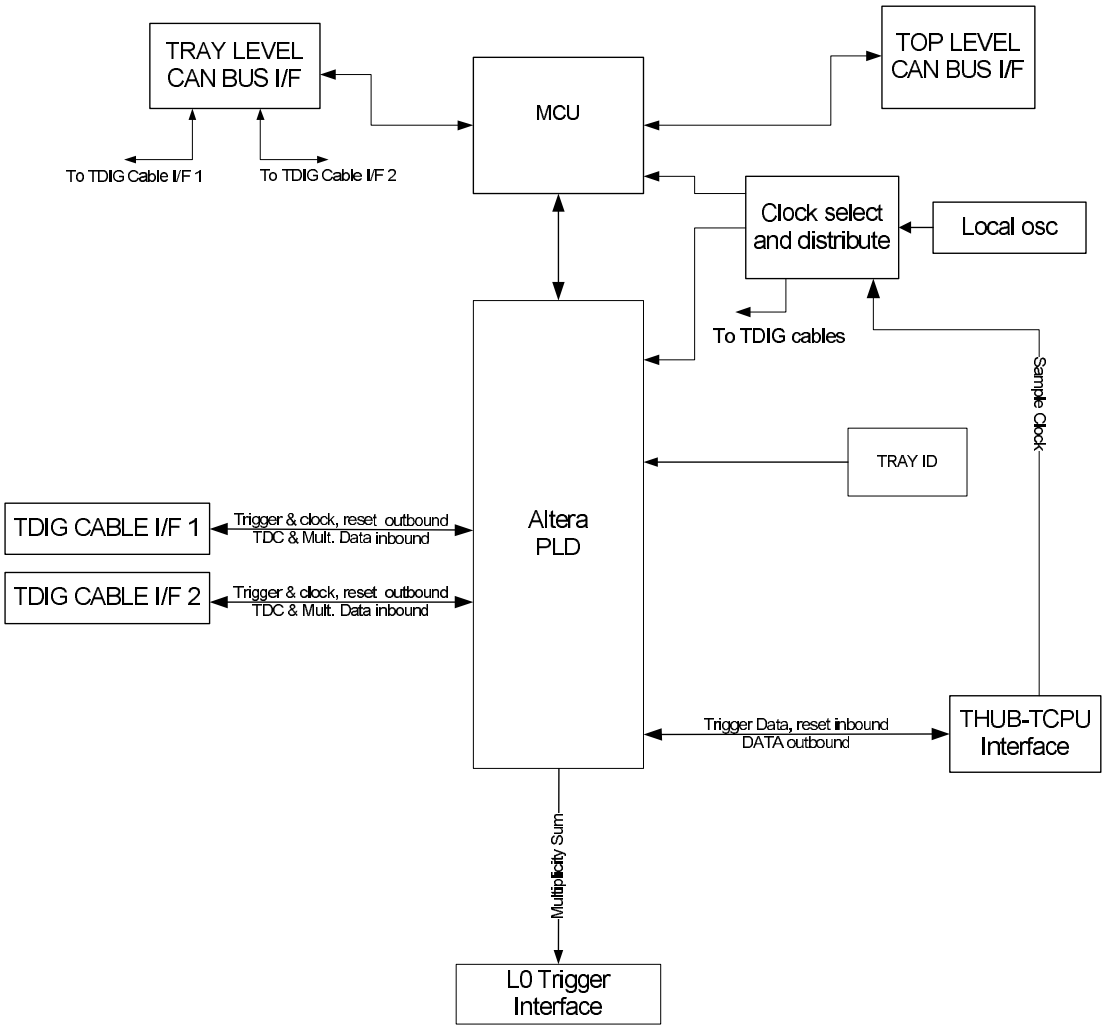

Figure 3.16: Top level block diagram of TCPU

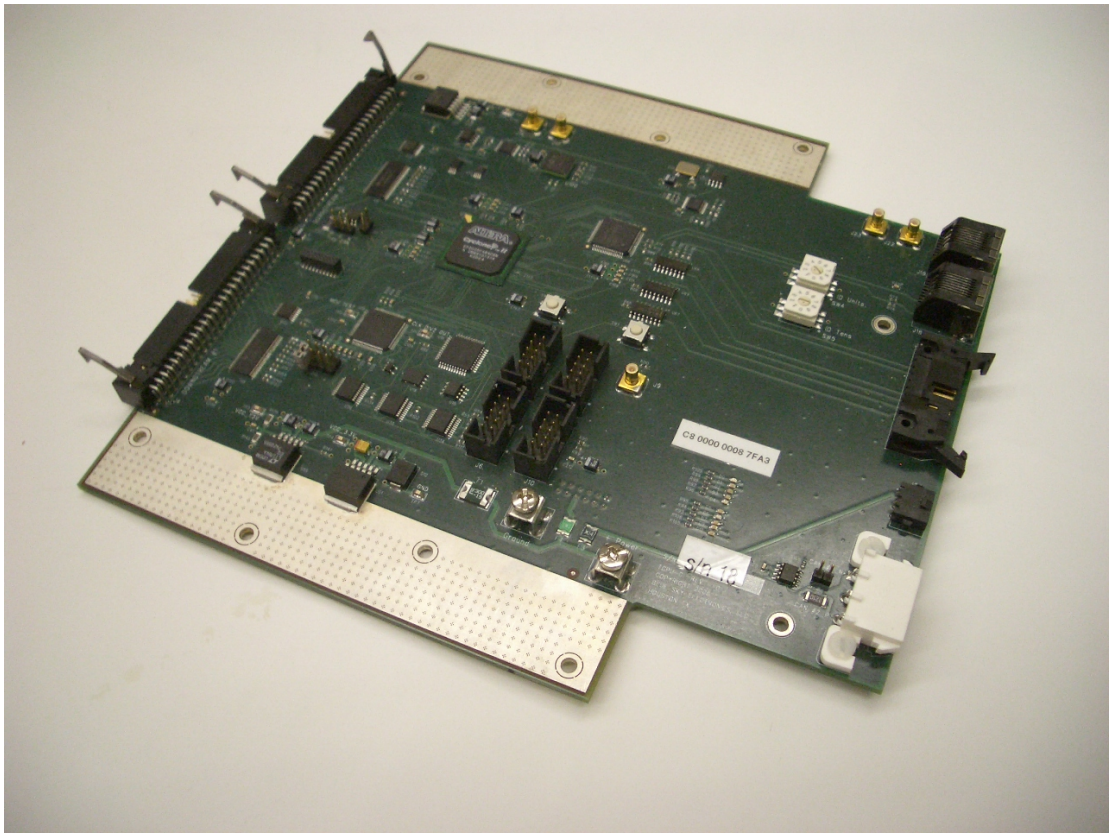

Figure 3.17: Picture of TCPU.

- **Trigger command processing** – Receives and processes commands from the STAR trigger. It also handles some commands like Abort and L2 Accept to the DAQ.

3.3.8 THUB

The THUB, as the name indicates, acts as hub for data and trigger signal transportation. There are 4 THUBs which are identified by their installation locations on the ends of the STAR magnet: NW, NE, SW, and SE. Figure 3.18 is a block diagram of the THUB, and Figure 3.19 shows a picture of one of the THUBs.

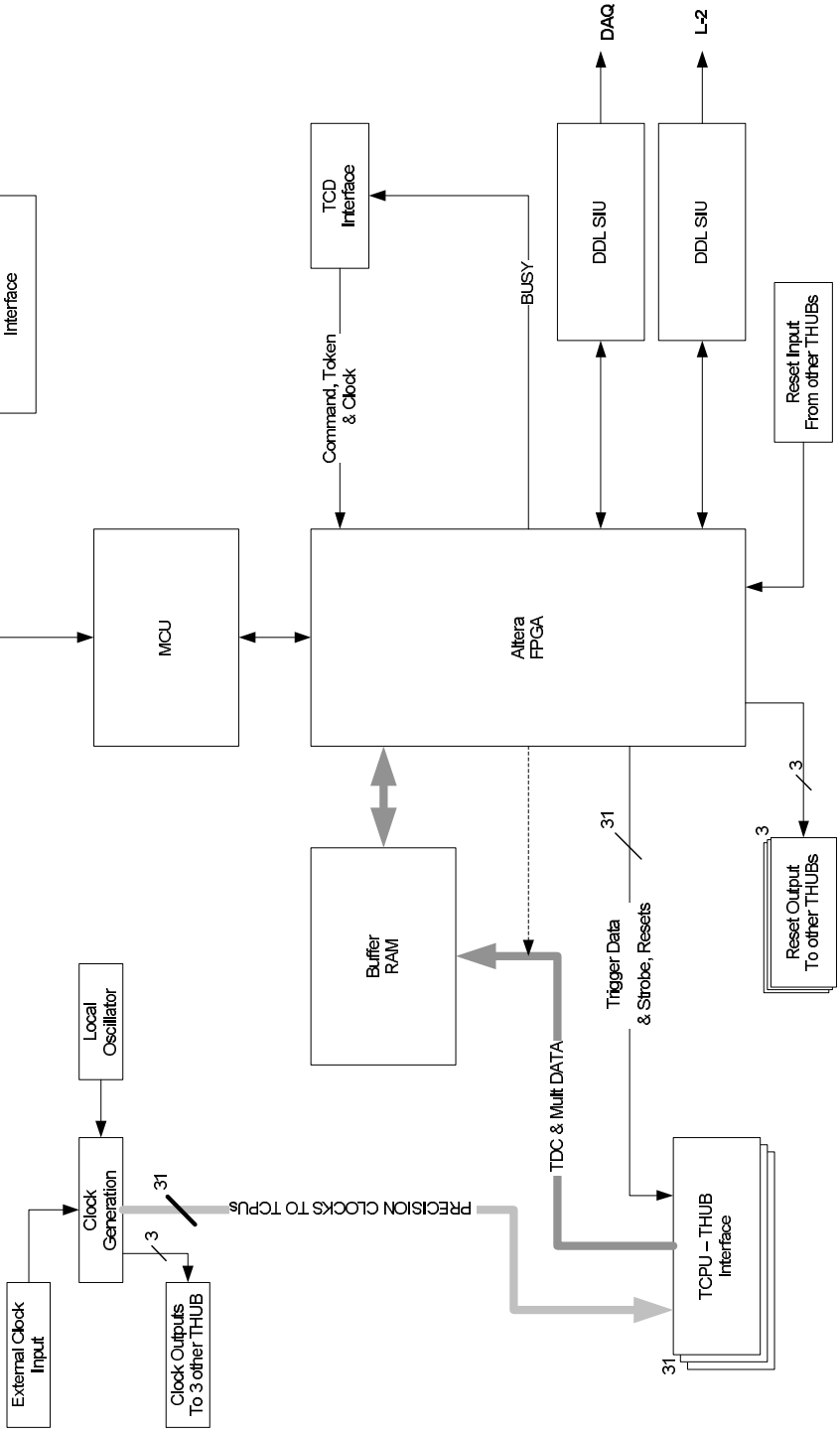

Figure 3.18: Block diagram of THUB.

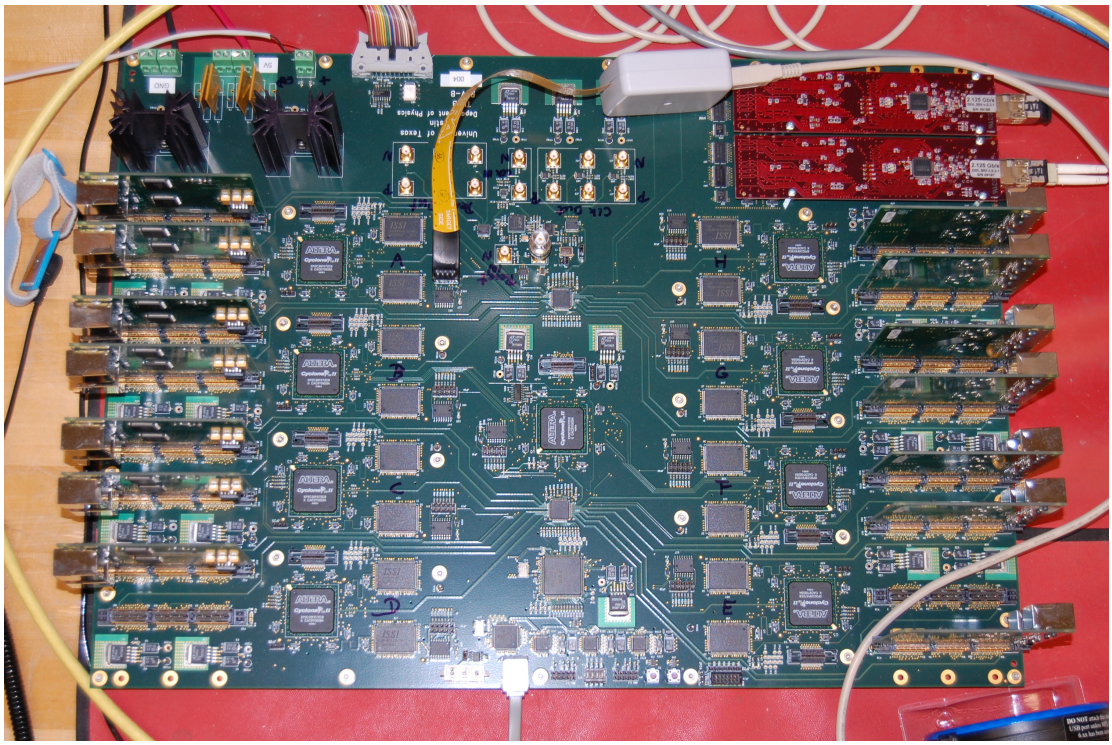

Figure 3.19: Picture of THUB.

3.3.8.1 SERDES Board

The SERDES board is a daughter card on the THUB mother board. Each SERDES provides two SerDes ports. The physical connection between the card and the TCPU is archived by using a Category 6 cable. This cable carries the trigger signals and a 40 MHz clock signals from the experiment to the serialized data signal. A full THUB can have at maximum sixteen SERDES cards installed on its mother board, supporing 32 SERDES links. A picture of the SERDES card is shown in Figure 3.20.

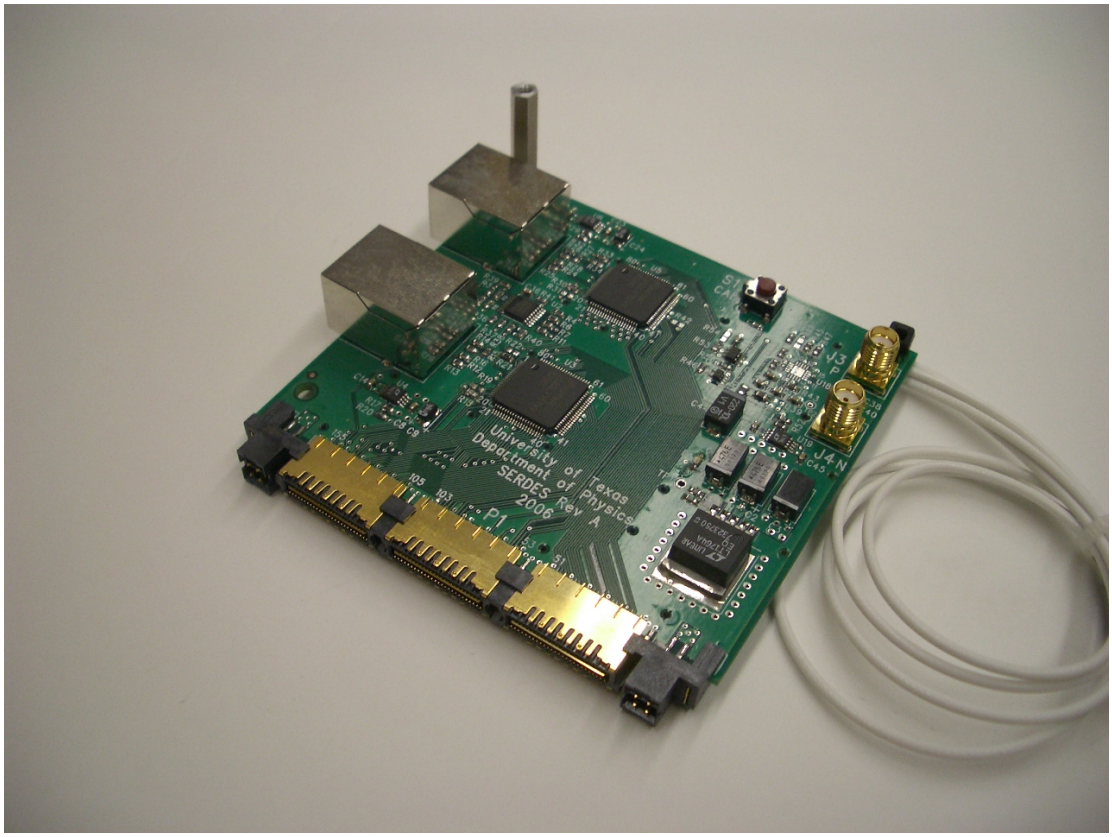

Figure 3.20: Picture of SERDES.

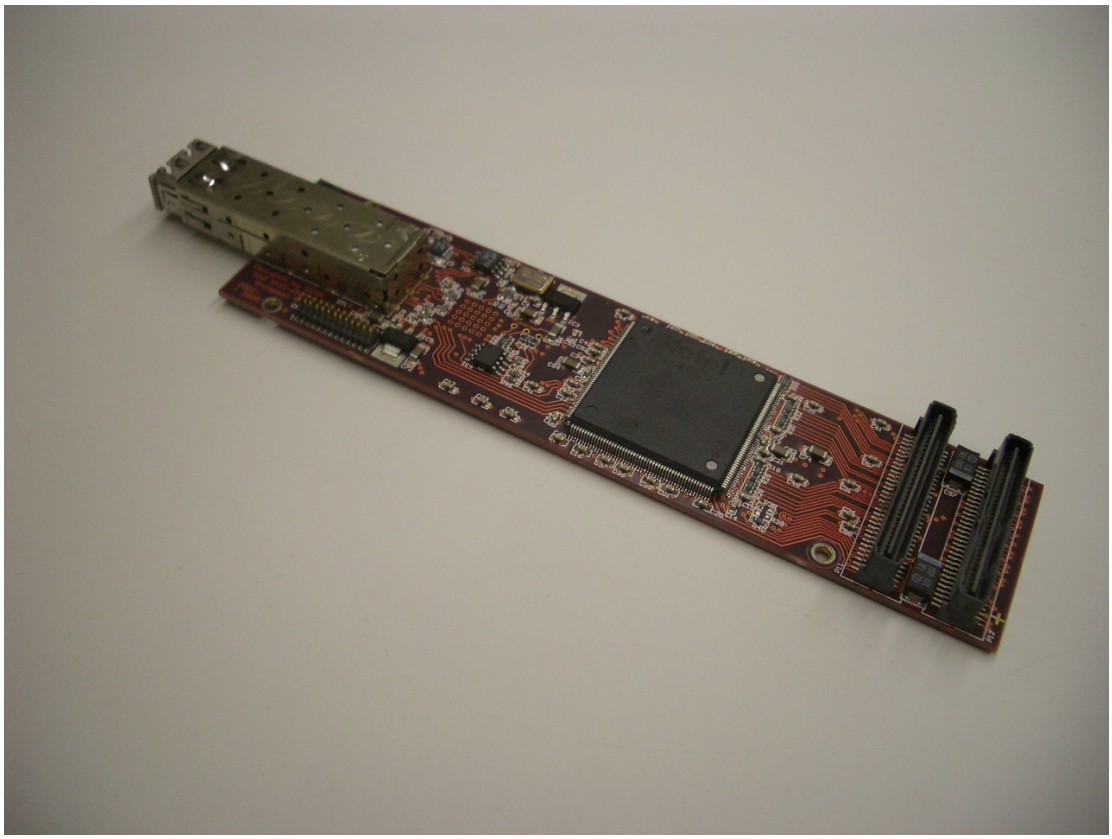

Figure 3.21: Picture of ALICE DDL SUI.

3.3.8.2 ALICE DDL SUI

The ALICE detector data link (DDL) source interface unit (SUI) is equipped as a daughter card to the THUB mother board and provides a fiber link to the STAR DAQ. This card was also developed at CERN for ALICE. Figure 3.21 shows a picture of a SUI card.

3.3.9 TOF DAQ Receiver

The TOF DAQ receiver is a Linux PC with several hardware interfaces used to interact with STAR's DAQ system and the TOF detectors. The interfaces are: one Myrinet interface, 4 fiber optic interfaces, Read Out Receiver Cards (RORC) which are designed around DDL DIU and developed by CERN for ALICE. The PC has a PCI-X bus, which is relatively uncommon in the standard commodity sphere, but necessary to meet the RORC's requirements.

3.3.10 TOF Controller

The TOF controller is a Linux PC with 6 CAN-bus interfaces using PCAN-USBs[1]. The controller is used as a root of the TOF slow control system.

3.3.11 Inter Connections

The electronics components described above are connected to each other by wires that form a multi-layered network. There are five type of networks in the system as shown in Figure 3.22.

- **Data Network** starts from either the MRPC modules in the trays or the PMT of a pVPD, and ends at STAR DAQ system. Its physical connection differs at each stage of the propagation. The raw signal from the MRPC to the TINO is carried by a bundle of twisted pairs of wires. Connections at the TINO side are made using a 34-pin pigtail. The TDIG to TCPU connec-

[1]PCAN-USB adapter by PEAK-System Technik GmbH.

tions are done using 50-pin ribbon cables. The cables carry all information both downstream and upstream between the TCPU and TDIGs. From the TCPUs to THUB, the data is carried by CAT-6 cables.

- **CAN-bus Network** provides connections used to configure and monitor the status of trays. There are six independent CAN-bus networks for the STAR TOF system. The TOF controller is connected to the all networks via its CAN-bus adapters. Two of them are dedicated to East and West side at the start side TCPUs, and the rest are used for interface between the THUBs and TCPUs on the TOF trays. On each TOF tray a CAN-bus network lives on 50-pin ribbon cables that connect TCPUs to TDIGs through two sets of daisy-chain.

- **Trigger Network** connects the STAR Level-2 Trigger and all the THUBs with DDL links of four dual optic fibers.

- **Clock Distribution Network** has a single root tree structure that begins from a master THUB (THUB-NW for the Run-9 configuration) and ends at the TDIGs. The interlayers consist of slave THUBs, TCPUs, and several layers of TDIGs. A 40 MHz clock signal propagates on RG-58 coaxial cables from the master THUB to the slave THUBs and across shielded CAT-5 cable from the master/slave THUBs to TCPUs, and finally on 50-pin ribbon cable from TCPU/TDIGs to TDIG.

- **Multiplicity Network** starts from the NINO chips and ends at DSM of the STAR Level-0 Trigger. The path shares the same physical connection

as the data path up to the TCPU; however, it goes directly to the DSM interface on a copper ribbon cable.

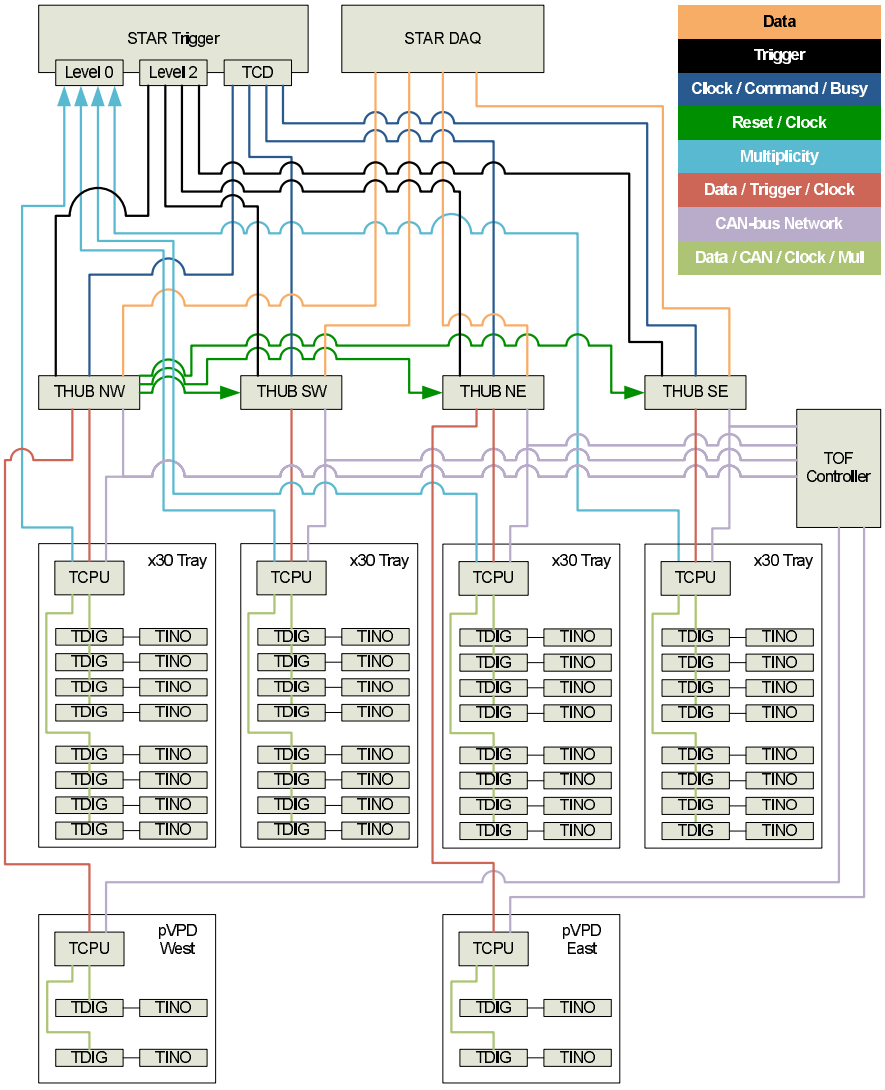

Figure 3.22: Schematic diagram of the interconnections.

Chapter 4

MRPC Testing

The MRPCs were built at two universities in China, Tsinghua University and University of Science and Technology of China (USTC), and then shipped to UT. At UT several Quality Assurance (QA) activities were performed as discussed in this chapter.

4.1 MRPC size

The first QA activity was to measure the dimensions of the MRPC's to insure that they met the design specifications shown in Table 4.1. This was done during summer 2006 for modules TM001-090 and modules UM001-040)[1]. Figure 4.1 shows where measurements were made. A summary of results is shown in Table 4.2. Subsequent batches of modules were checked with custom made sizing jigs. Two of the sizing jigs can be seen in Figure 4.2.

4.2 Signal Cable Connection Test

As described in Section 3.2, each MRPC module has 6 pairs of copper pick up pads, and each pair is redundantly connected to two pairs of twisted signal

[1]Results are available at http://www.rhip.utexas.edu/~tofp/module/size.php

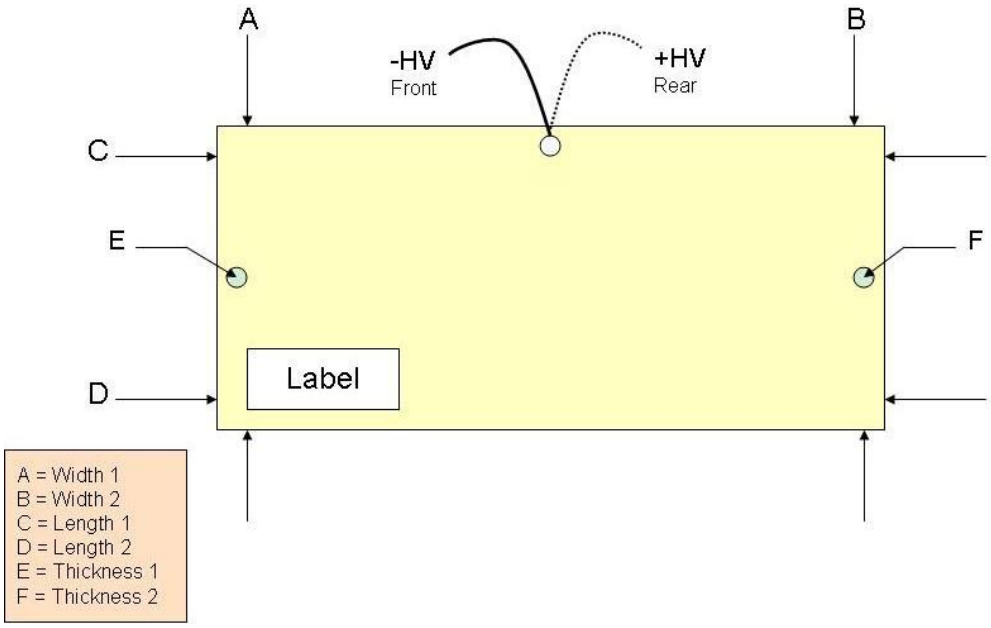

Figure 4.1: MRPC dimensions measured as part of QA activities.

	nominal	minimum	maximum
MRPC overall length (mm)	212.0	211.5	212.5
width (mm)	94.0	93.5	94.5
thickness (mm)	17.9	16.9	18.9

Table 4.1: Specification of MRPC module geometry.

	mean	sigma
length (mm)	211.94	0.101
width (mm)	94.04	0.062
thickness (mm)	18.21	0.141

Table 4.2: Summary of MRPC module geometry measurements

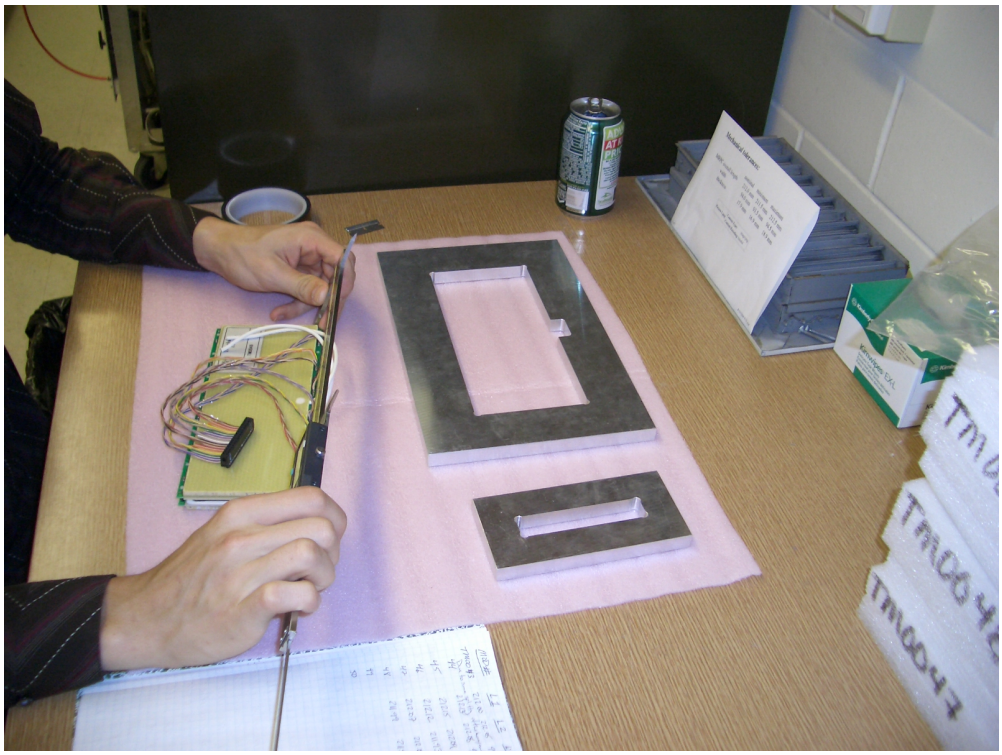

Figure 4.2: Picture of MRPC QA activity; sizing jigs are window frame shapes on table.

cables which are soldered to the pad. A total of 12 pairs of twisted cables are connected to a 34-pin ribbon cable connector, leaving 10 unused pins. A test apparatus utilizing a microcontroller and multiplexers was designed and constructed to test for shorts, broken wires, and the connectivity of the solder joints.

The 16 bit microcontroller (PIC16F913) manages four 16-channel multiplexiers (MAX306), and systematically measures the resistance between every pair of pins. If the module passed the tests a green LED is lit, while failure is indicated by a red LED.

The circuit design and prototype development for the microcontroller was done from December 2006 to January 2007. During this period, firmware was also developed; the firmware was written in the PIC assembly language using MPLAB IDE[2]. A picture of the tester and diagram of the circuit are shown in Figure 4.3 and Figure 4.4, respectively. See Figure 4.5 for the main algorithm of the firmware.

4.3 High Voltage Test

In the spring of 2007 we found that some of the modules drew large currents; this was especially noticeable during voltage rampup. Since all 32 modules in a tray share the same high voltage bus a single module with high voltage problems could affect the entire tray. We therefore decided to perform high voltage tests on every module. An aluminum box was buildt that held 6 MRPCs.

[2]Source is available at http://www.rhip.utexas.edu/~tofp/documents/files/mctester.tgz

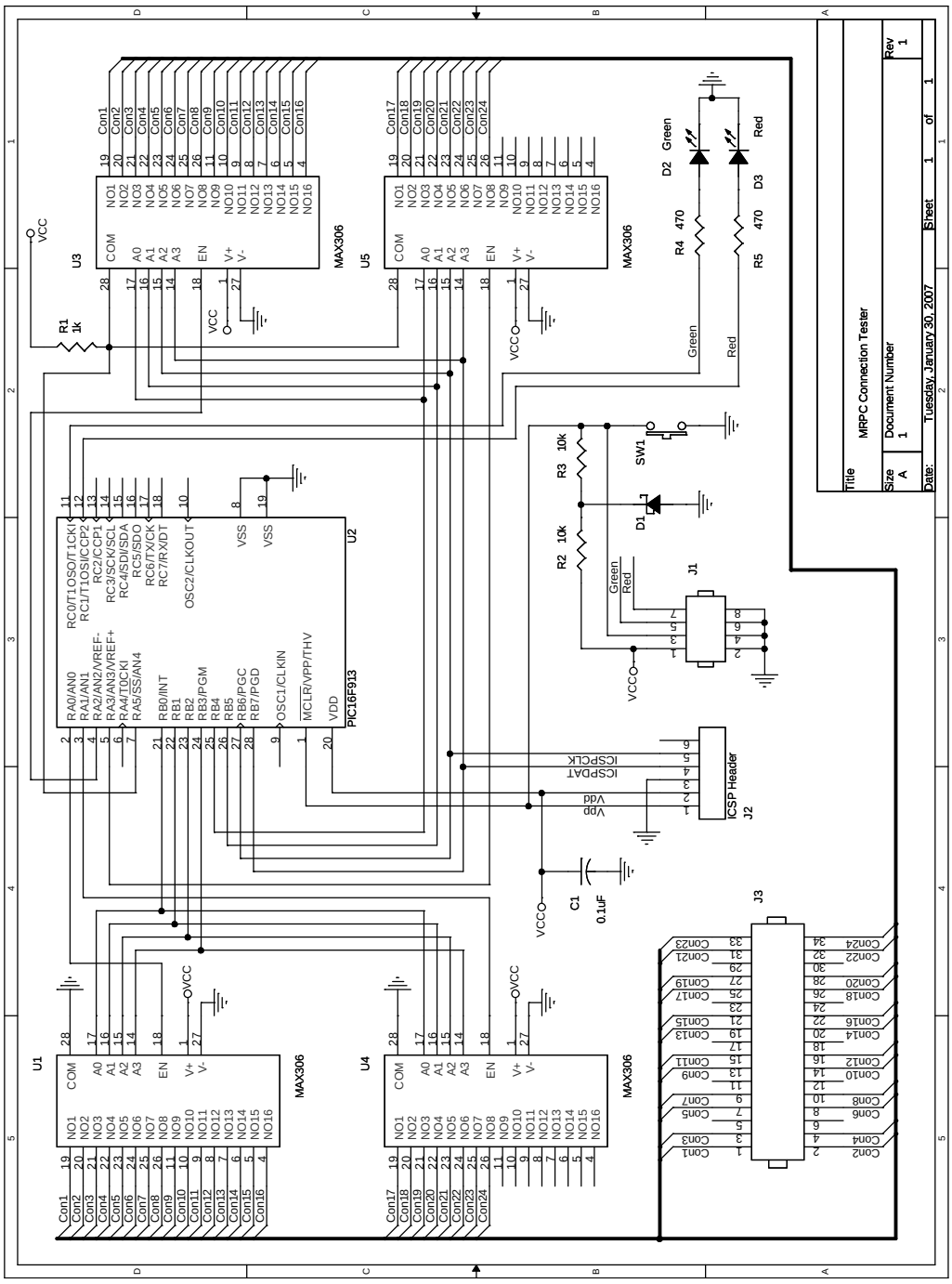

Figure 4.3: Circuit diagram of MRPC connection tester.

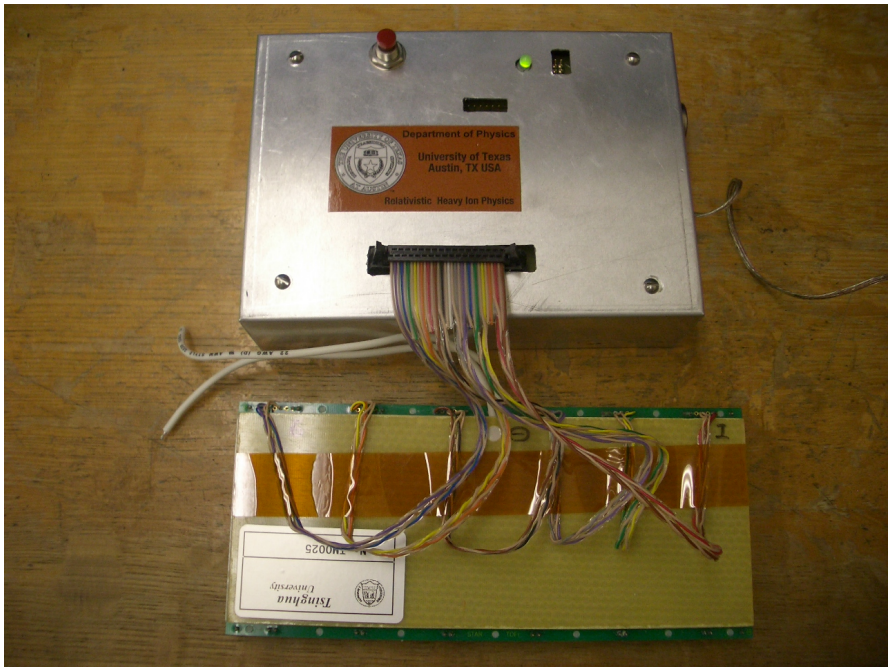

Figure 4.4: Picture of MRPC connection tester.

```
#define THRESHOLD_LOW   2
#define THRESHOLD_HIGH  4
for(i = 23; i >= 0; i--)
  for(j = 24; j > i; j--) { // loop over all pin pairs
    set_multiplexer(i, j);
    if( same_pad(i, j) ) {
      if(measure_voltage() < THRESHOLD_LOW) return ERROR;
    } else {
      if(measure_voltage() > THRESHOLD_HIGH) return ERROR;
    }
 }
return SUCCESS;
```

Figure 4.5: Pseudo-code for the main algorithm.

After placing the modules in the box, a roughing pump was used to quickly remove air from the box so that at atmosphere of pure freon (R134a) could quickly be established in the box. Typically, the procedure took about 5 minutes before HV ramping could start.

From July 16, 2007 to October 11, 2007, 682 MRPC modules were tested, and 3 modules (TM0101, TM0107 and TM0151) were found unable to hold high voltage[3]. A picture of the test apparatus is shown in Figure 4.6. The QA activity was discontinued when the "submarine" cosmic test station, which will be described in Section 4.4.4, came online.

4.4 Cosmic Ray Testing

Three cosmic ray test stands, each equipped with STAR TOF prototype electronics, were built during the summer of 2003. Initially, the primary purpose of the cosmic ray tests was to evaluate the performance of the MRPC modules while using the prototype electronics. That focus eventually evolved into a quality assurance proceedure that checked every MRPC module before tray assembly.

4.4.1 Cosmic Rays and Muons

At sea level, muons make up almost all of the charged particles originating from cosmic rays. The ratio of vertical flux muons to protons (the second most abundant cosmic ray) is of order 10^2 [1]. Therefore when detecting cosmic rays

[3]Full results are available at http://www.rhip.utexas.edu/~tofp/hvtest/

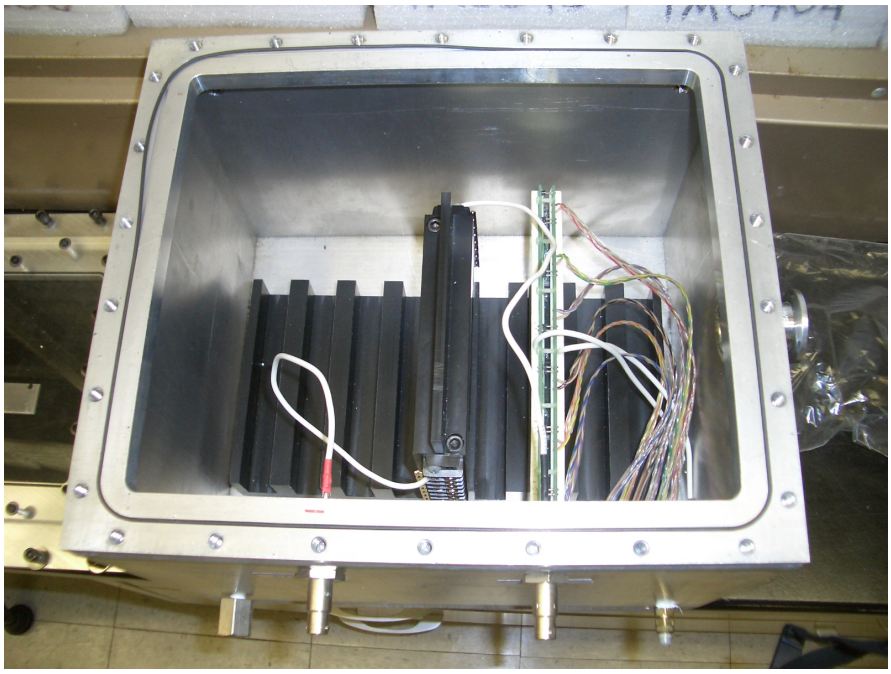

Figure 4.6: The high-voltage test box.

in the lab one can assume that all charged particles are muons. The integrated intensity of vertical muons above 1 GeV/c at sea level is reported as follows[1]:

$$I(E_\mu > 1\text{GeV}/c) \approx 70\text{m}^{-2}\text{s}^{-1}\text{sr}^{-1}\,. \tag{4.1}$$

Assuming the full upper sphere $\Omega = 2\pi$ is sensitive and taking into account the MRPC pad size $A = 6.1\text{mm} \times 3.1\text{mm} = 1.89 \cdot 10^{-5}\text{m}^2$, the cosmic ray incidence rate for a pad can be estimated as

$$f \approx 70 \times 2\pi \times 1.89 \cdot 10^{-5} \approx 8.31 \cdot 10^{-3}\text{Hz}\,. \tag{4.2}$$

It is worth mentioning that the frequency roughly corresponds to one hit every two minutes for a given pad.

4.4.2 First 'Small' Box

The first cosmic ray test stand was designed to hold 3 MRPC modules. The detector system consisted of a gas box containing 3 MRPCs, 3 trigger scintillators, and a data acquisition (DAQ) system. Figure 4.7 and Figure 4.8 show the geometry and electronics setup, and Figure 4.9 shows the aluminum stand on which the box and scintillators were placed.

The stand has dimensions 39"h×48"w×24"d and has 3 shelves. It sits on a base made of square aluminum tubing. The MRPC box was placed on the middle shelf. 3 MRPC modules are mounted horizontally inside the box about 1" apart from each other. A gas inlet and outlet allowed for flowing R134a, and two high voltage feedthrus supplied the positive and negative high voltage to the modules.

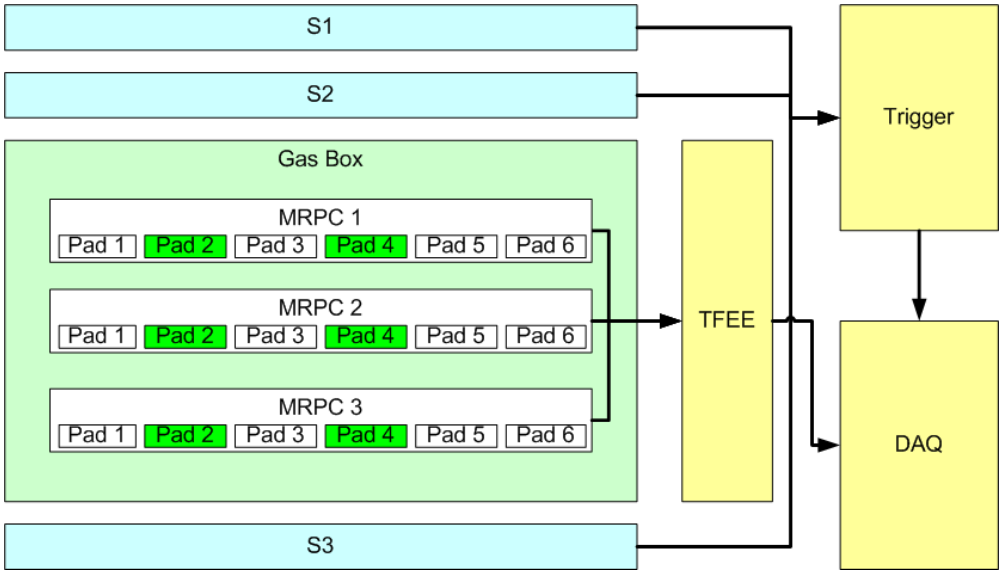

Figure 4.7: Block diagram of the first small cosmic ray setup.

Finally a TFEE prototype card was mounted over a hole in the the top of the box. An O-ring between the TFEE and the box made the setup gas tight. During the data taking Freon (R134a) flowed at a rate of 20 sccm through the gas inlet/outlet. The TFEE was designed to be gas tight, and its backside was exposed to the inside of the aluminum box. The signal wires from the MRPC modules were connected to the backside of the TFEE. Because the TFEE was a prototype, only 6 channels could be read out at a time. Instead of reading out a single 6 channel MRPC, the signal cables from pads 2 and 4 of each of the three modules were connected to the TFEE, and the noise rate measurements and timing resolution tests were made for only those 2 channels on each module. The trigger was made from three plastic scintillators coupled to EMI9813B photomultipliers with tube bases. Two of the scintillators (S1 and S3) had dimensions $3'' \times 3'' \times 6''$, and the third (S2)

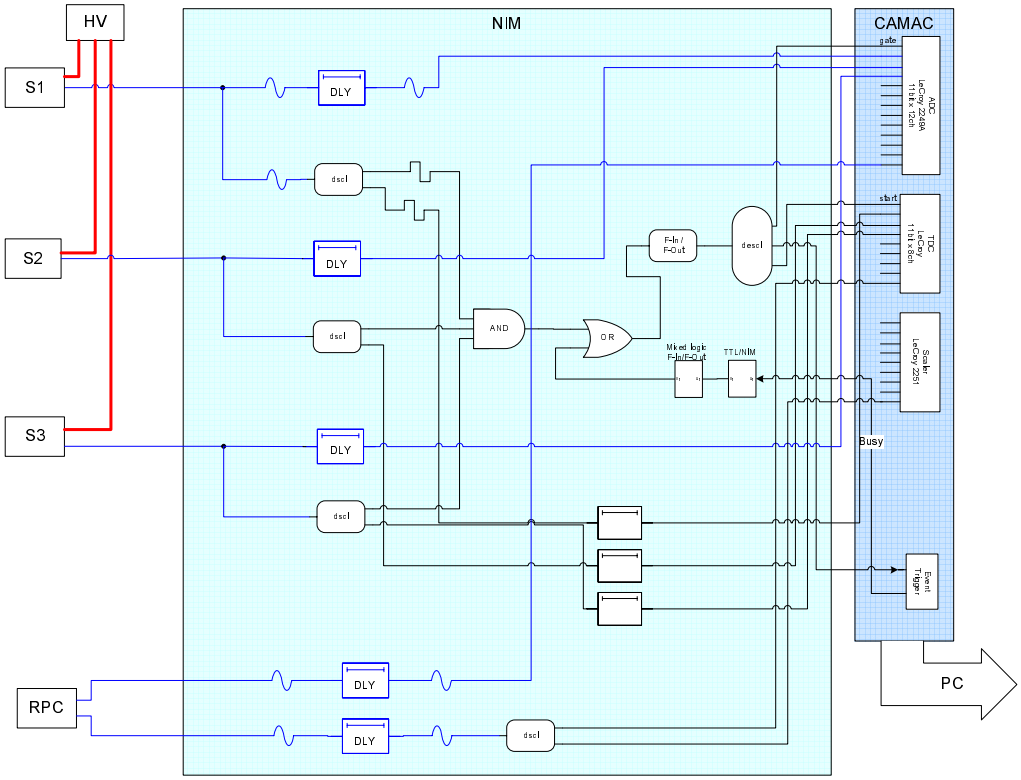

Figure 4.8: Schematic of trigger electronics for the first cosmic ray setup.

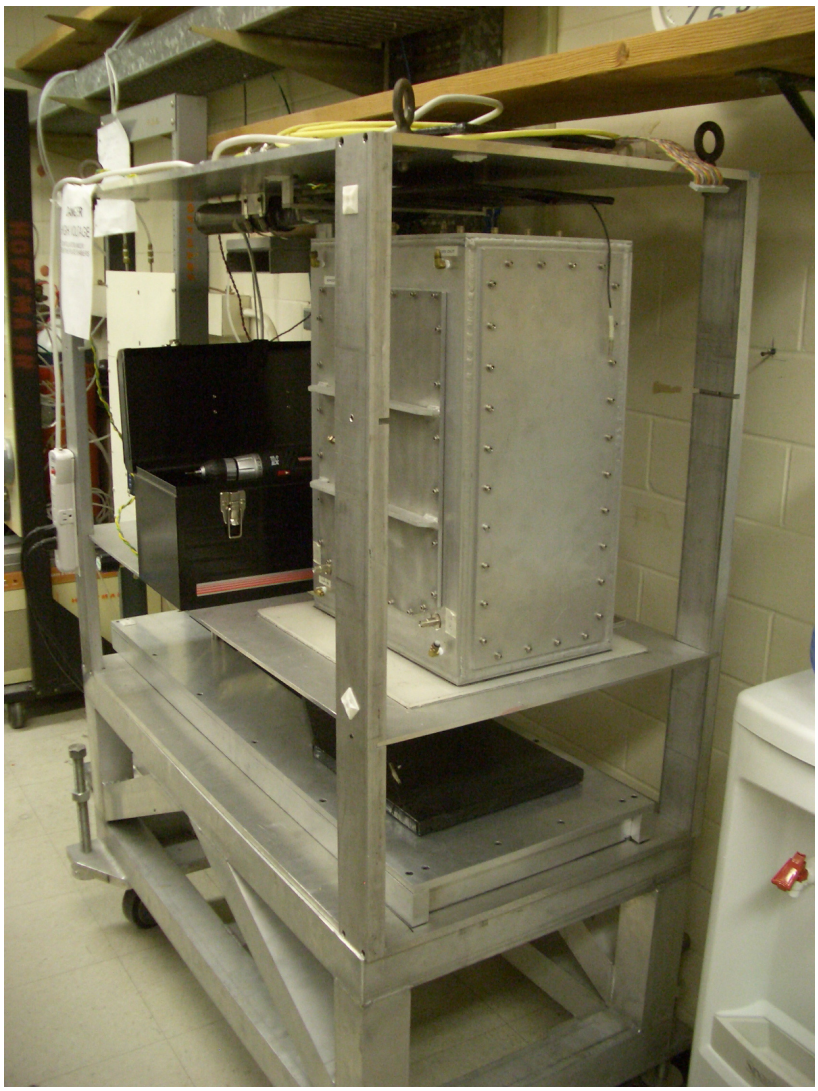

Figure 4.9: The aluminum test stand and dolly. Picture was taken after the setup had been changed to the second 'big' box, and the gas box and paddle scintillators shown in the figure are not for the first setup.

had dimensions $6'' \times 6'' \times 1/4''$. S1 and S2 were mounted on the top shelf and the S3 on the bottom shelve. The three scintallators, labeled S1-S3 from top to bottom, were aligned vertically as shown in Figure 4.7.

A triple coincidence among the three scintillators defined the trigger. The trigger logic was implemented through a series of NIM and CAMAC modules that were set up in a separate 19" rack.

Because the horizontal area of S2 was larger than that of the S1 and S3, the distance (23.2") between S1 and S3 determines the solid angle of the detector as follows:

$$\Omega = 3" \times 6"/(23.2")^2 = 3.3 \times 10^{-2}\text{sr}\,. \tag{4.3}$$

The DAQ system is a combination of NIM and CAMAC modules and a Linux PC. As mentioned above, a trigger is generated when signals from the three plastic scintillators are all above a given discriminator threshold (LeCroy 623), and within a given time interval at a coincidence module (LeCroy 821). This condition is most likely satisfied when a charged particle goes through all three scintillators. Once an event is triggered, the ADCs (LeCroy 2248A) and TDCs (LeCroy 2228A) start recording signals from the MRPCs and the scintillators. A Kinetic System 2915 CAMAC Controller was used to read ot the data. During the readout the event trigger (BiRa 2206) and several NIM modules, including the OR logic module (PS 794), implement a block function that vetoes events until the current event is recorded.

The data stream is also show in Figure 4.7 by arrows.

Pad	#(top & bottom)	#(top & middle & bottom)	efficiency
4	2665	2316	86.9 %
2	2140	1939	90.6 %

Table 4.3: Number of events satisfying two conditions: the particle hits on the top & bottom pad or hits on the all three pads.

With the setup described we demonstrated that the timing resolution was at least 90 ps when using prototype electronics. This test setup was used throughout 2004, before the "big box" setup was developed.

4.4.2.1 Example of Analysis and Results

For the data taken from September 4 to September 11, 2003, the running time was 578,116 seconds ($\sim$ 188 hours), the total number of events was 23,324, and the average event ratio was 4.034×10^{-2} event/sec.

The following analysis is focused on events where the charged particle passes vertically through the 3 MRPCs modules, i.e it only hits the #4 pads in each module or only the #2 pads. Because any particle that hits both the top and the bottom pad must also pass through the middle pad, so it was possible to estimate the efficiencies of the middle pads. The results are show in table 4.3.

Figure 4.10 shows the ADC1 dependence of TDC1-(TDC0+TDC2)/2 where 'ADC1' means 'readout from the channel 1 of the ADC module', 'TDC1' stands for 'readout from the channel 1 of the TDC module', and so on. The curve is obtained using the assumption that the TDC values depend exponentially on the corresponding ADC values.

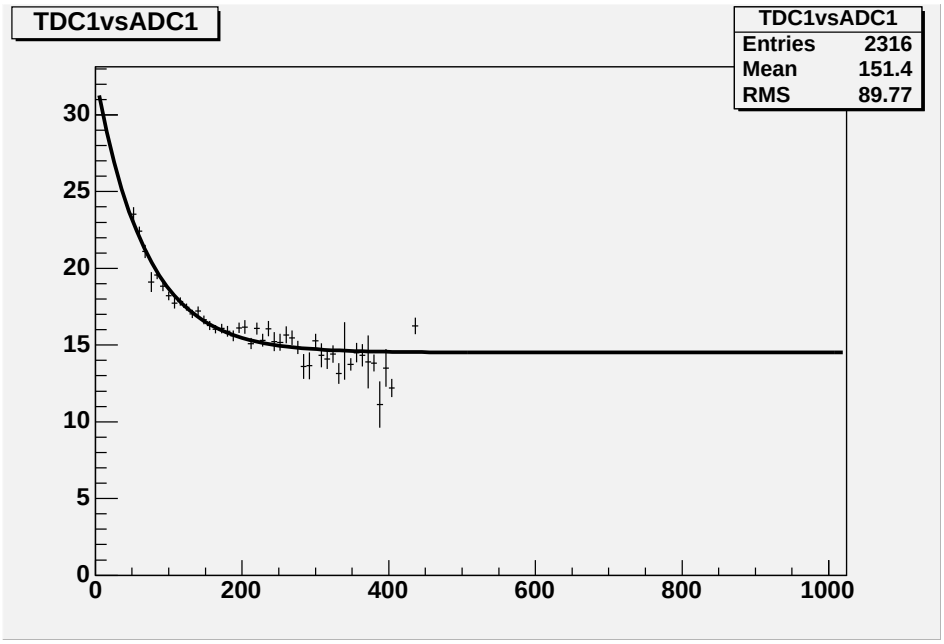

Figure 4.10: Plot of TDC1-(TDC0+TDC2)/2 vs. ADC1 and fitted curve.

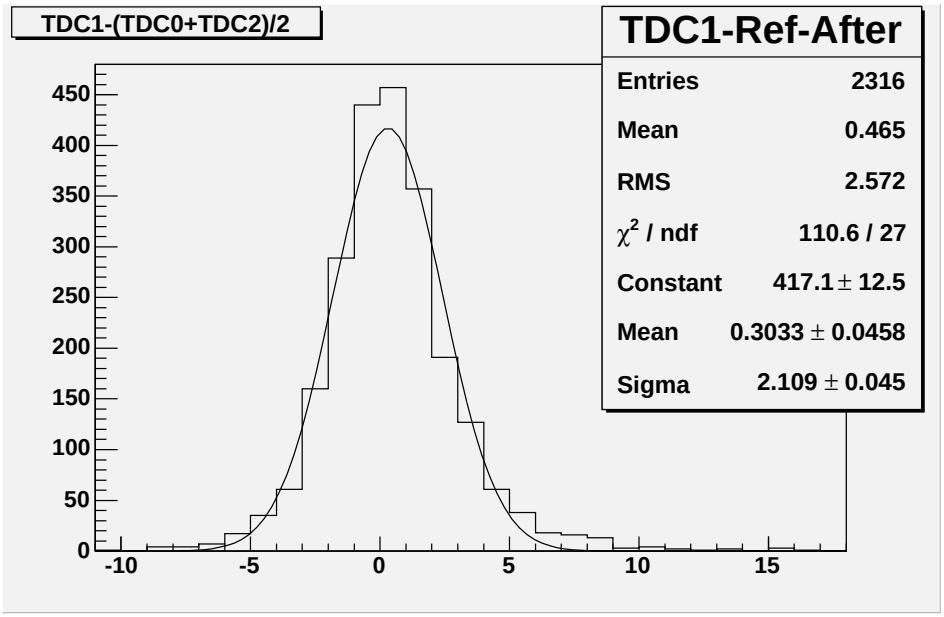

Figure 4.11: Corrected TDC1-(TDC0+TDC2)/2 Histogram.

A "slewing" correction for TDC1 can be made by removing its ADC1 dependence, thereby making the fitted curve flat. This will still leave ADC0 and ADC2 dependences in the corrected graph, which are due to TDC0 and TDC2 "slewing". So to correct for these dependences, the same method must be applied recursively, rotating the role of three channels cyclically in each step. Figure 4.4.2.1 presents the results after all the corrections were made and shows that the detector, a combination of the three pads, has a resolution of 2.1 bins (105 ps), or 1.7 bins (86 ps) for each pad. Similarly the corrected graph for the pad #2's (Figure 4.4.2.1) shows its resolution is 2.2 bins (110 ps), or 1.8 (90 ps) bins for each pad.

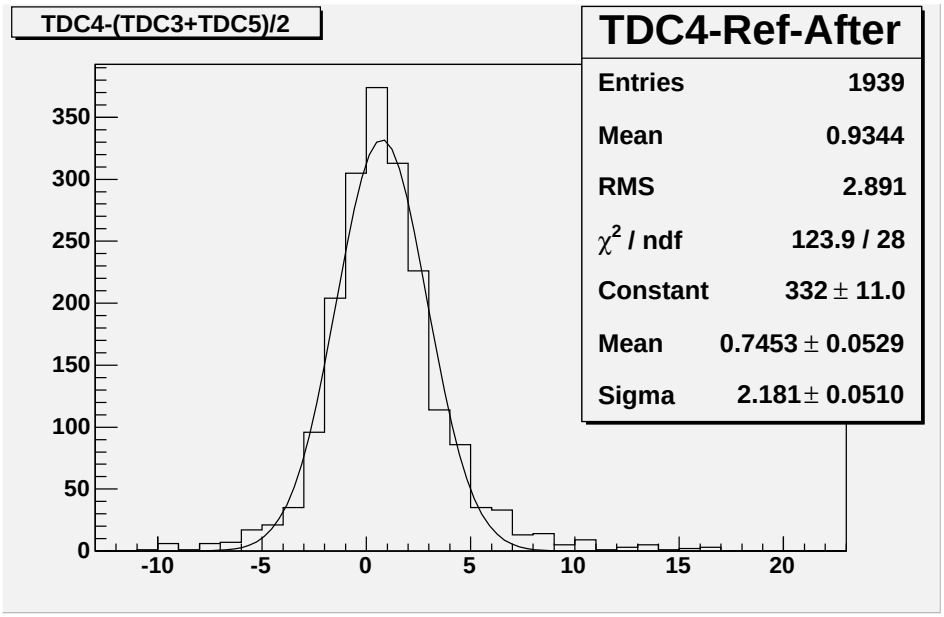

Figure 4.12: Corrected TDC4-(TDC3+TDC5)/2 Histogram.

4.4.3 The Second 'Big' Box

The purpose of the 'big' box was to use the new front-end electronics (TAMP, TDIG and TCPU) with a cosmic ray setup to demonstrate that these electronics performanced as required. The work was started in Spring 2004, and the first data were taken in late July. The gas box on the old stand was replaced with a larger box, and larger trigger scintillators were used. A picture of the 'big' box is shown in Figure 4.14.

A TFEE card was located on the gas box's side wall and was connected to NIM and CAMAC modules as done for the "small" box. In April 2005 the TFEE card and the downstream electronics were replaced with the newly developped

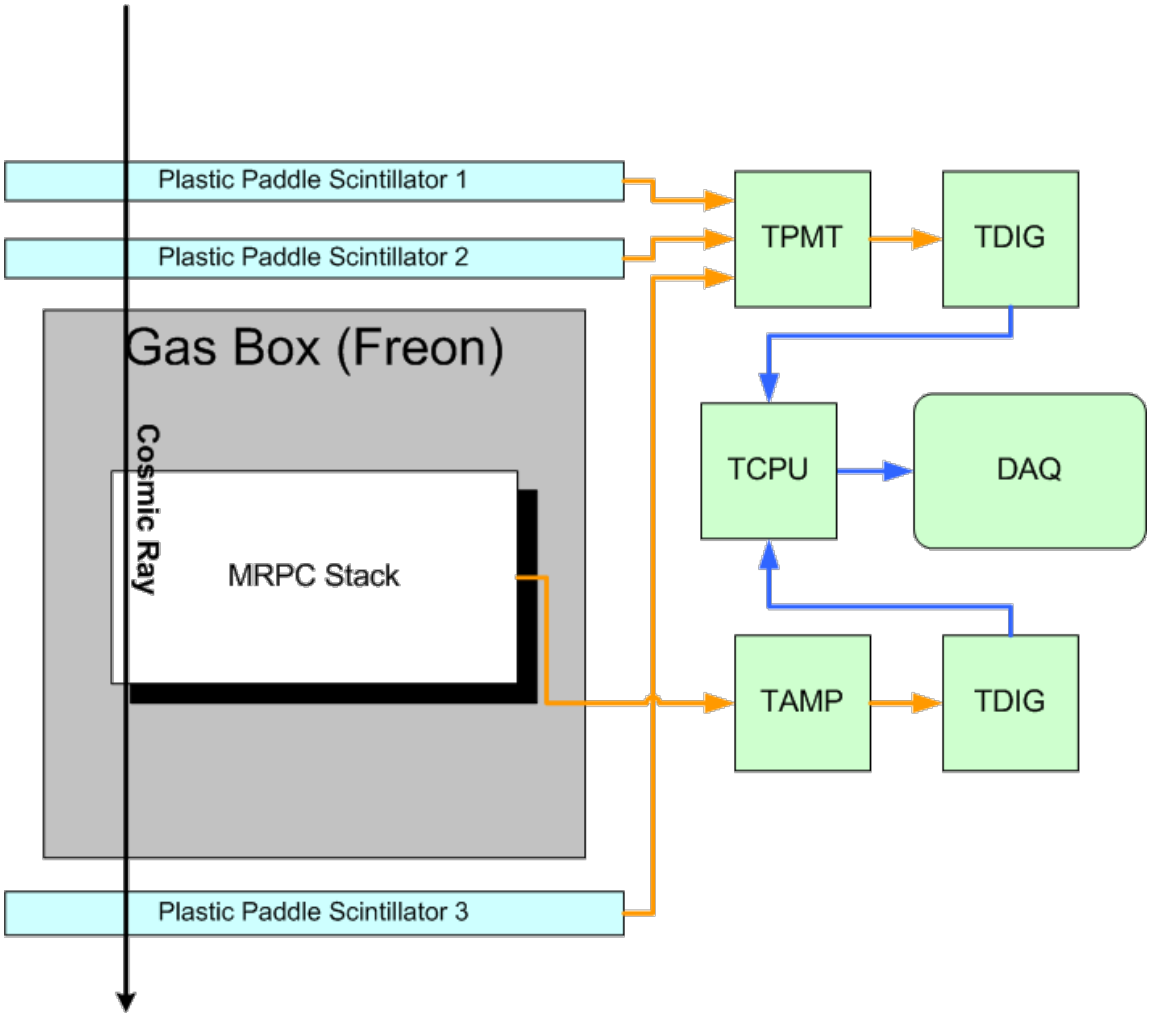

Figure 4.13: Block diagram of the second cosmic ray box.

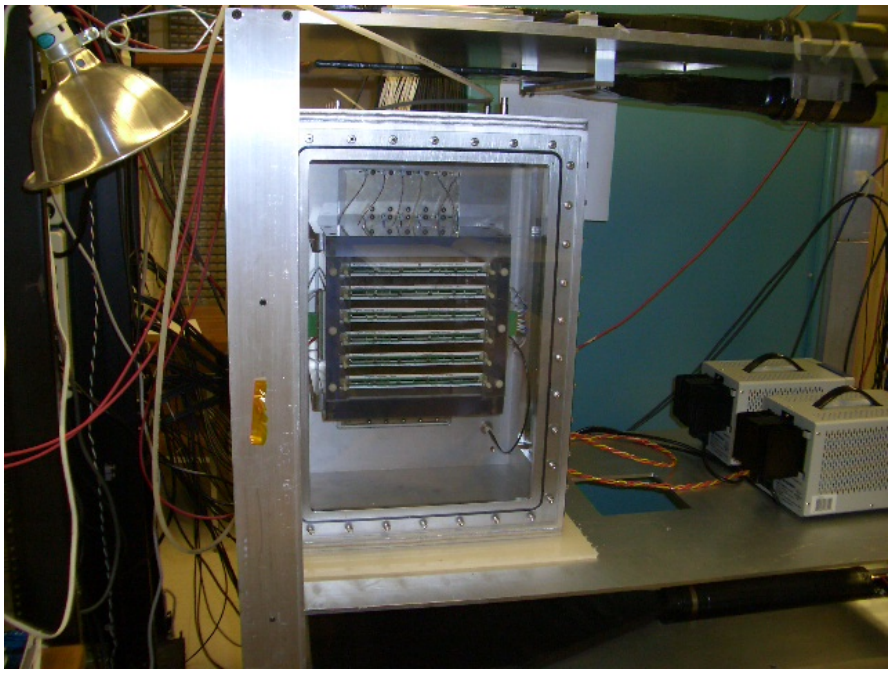

Figure 4.14: Picture of the second cosmic ray box.

TAMP, TDIG and TCPU cards, and the same test was repeated. Shortly after the reconfiguration, a newly developed TINO card was installed. But this TINO prototype only had 9 active channels, so the cosmic ray and noise rate measurements had to be done using a 3×3 configuration of pads. A new DAQ system was implemented in which signals from each MRPC module were digitized by TDIG, transmitted to TCPU, and sent to a Linus PC in packets via a CAN-bus network.

A daemon called 'pcanloop'[4] ran on the Linux PC and monitored the CAN-bus network, including the data packets sent from TCPU or TDIG. The daemon also accepted inputs from users via a UNIX FIFO interface that sent CAN-bus packets to the TCPU or TDIG cards, providing a means to interactively configure the setup. To control data taking, a graphical user interface was developed for the pcanloop. Until the final test stand was built in October 2007, the "big box" tested about 197 modules over a period of more than 6000 hours. All results were recorded in a MySQL database that was accessible over the internet[5]. Analysis methods and results from the tests are described in later sections.

4.4.4 The Third 'Submarine' Box

The submarine is the name given to an aluminum box the contains 32 MRPC modules and near final design TOF readout electronics. The submarine can be evacuated so that a Freon atmosphere can be established quickly. The modules are stacked four high in eight sets of Lexan holders. Two STAR CTB

[4]pcanloop was written by J. Schambach
[5]http://www.rhip.utexas.edu/~tofp/

S1-1	S1-2	S2-1	S2-2	trigger
hit	*	hit	*	yes
*	hit	*	hit	yes
others				no

Table 4.4: Trigger condition for the submarine. Asterisk means ignoring the channel.

scintillator trays were used for the cosmic ray trigger. One CTB tray was above the submarine and the other was below it. Each CTB tray consists of two p large plastic scintillators with photomultipliers and tube bases. A coincidence between overlapping scintillators in the top and bottom CTB trays defined the trigger. This is show in table 4.4. The top of a production STAR TOF tray was used to provide the submarine with TINO, TDIG and TCPU electronics and was attached at bottom of the submarine. Signal cables from the MRPC's lead to the TINO cards via 34-pin vacuum feedthrus. A delayed (5 μs) trigger signal started event readout. The raw analog signals were processed as they would be for the actual STAR TOF tray; both leading and trailing edges were discriminated by TINO, and TDIG did the time digitization. The TCPU then generated a series of 24-bit word packets which are then propagated through the CAN-bus network and sent to the Linux PC where they are stored.

4.4.5 Noise Rate Tests Using Submarine

MRPC noise measurements were also made before and after submarine cosmic ray runs.

Triggering for the noise data was done using the HPTDC on the TDIG. The

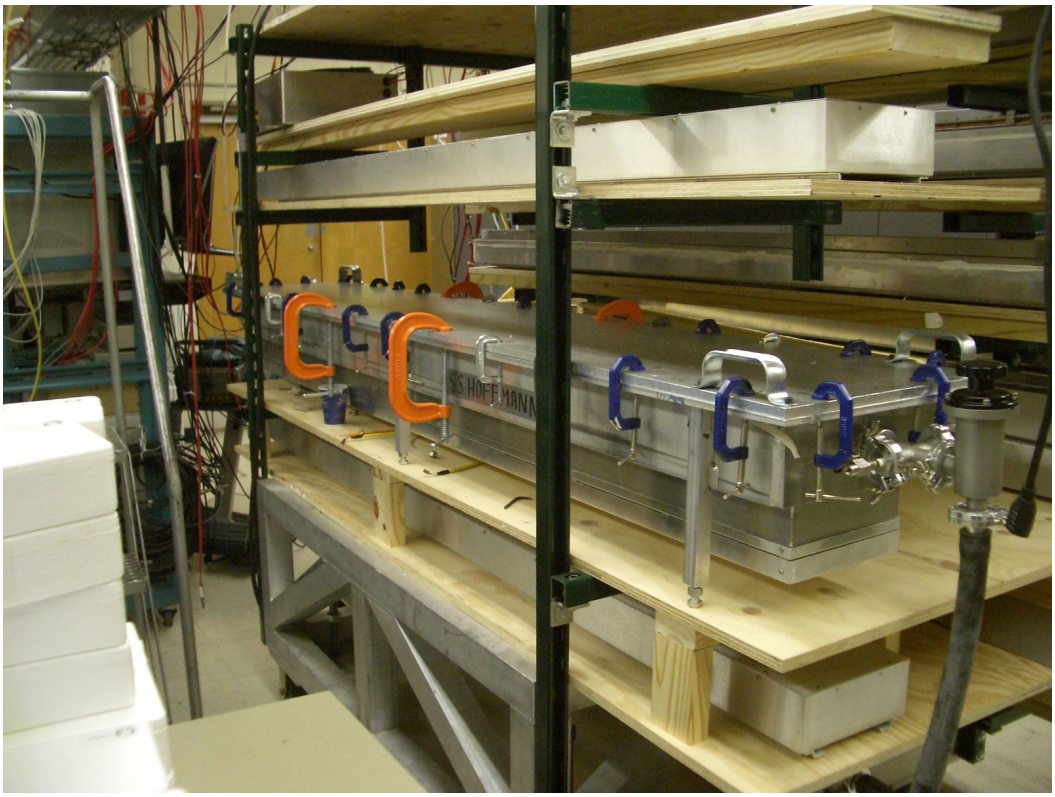

Figure 4.15: Picture of the submarine. Two CTB trays, above and below the submarine, generate the trigger.

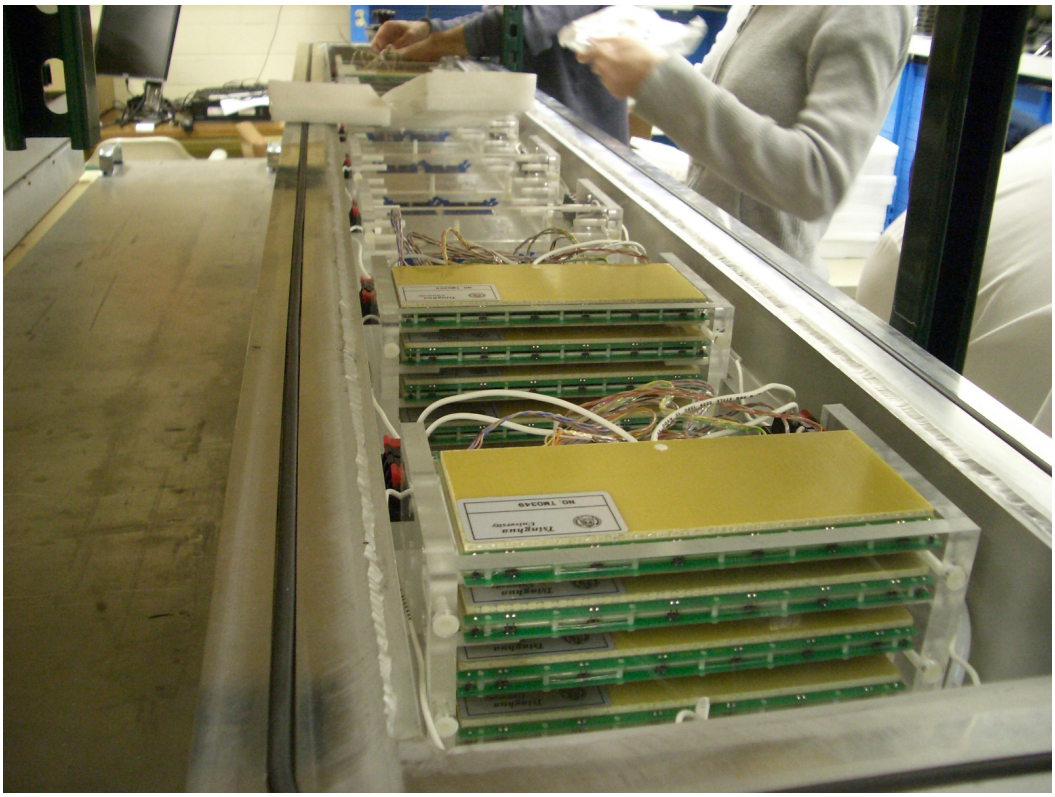

Figure 4.16: Picture of inside the submarine.

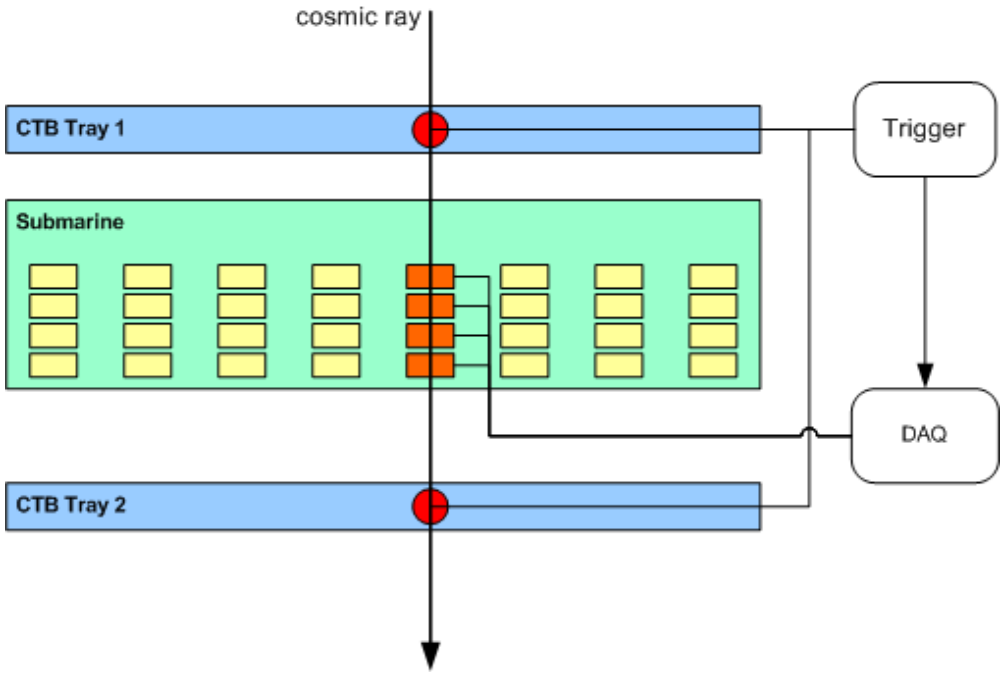

Figure 4.17: Schematic of the submarine. Small blocks inside the submarine represent MRPC modules. Total of 32 modules are placed as 8 stacks of 4 modules.

frequency of the triggers could be run at a much higher rate than that of cosmic rays so there was no need to mask out the triggers during noise rate measurements. The noise rates were estimated by counting the number of hits occuring at each channel (defined as crossing threshold) divided by the active running time. The active running time was determined by multiplying the read-in window size of the HPTDC, 50 μs by the number of triggers. The explicit rate calculation is given by,

$$r = \frac{c}{t} = \frac{c}{50\mu\text{sec} \cdot c_{\text{trig}}} = 2 \cdot 10^4 \left(\frac{c}{c_{\text{trig}}} \right) \text{Hz} \ , \tag{4.4}$$

where r is the average noise rate, c is noise counts, and c_{trig} is trigger counts. Typical data taking time was 1000 s, and noise rates were typically 10 Hz.

Noise rates were usually higher, $\sim$ 100Hz, shortly after the high voltage was ramped up. This is thought to be due to insufficient purging and/or dust/dirt on the glass surfaces of MRPC modules. Usually with 24 hours of sustained high voltage and Freon circulation at ($\sim$50 sccm) noise rates settled down to stable values ($\sim$ 10Hz).

Noise measurements were always performed longer than required for reliable measurements. The minimum condition can be expressed as $r \cdot t \gg 1$, that is, average noise cannot be 'measured' unless there is a significant number of hits on each channel. Running the external trigger at the hypothetical value of $r_{trig} = 100\,\text{Hz}$, with an intrinsic noise rate of $r = 10\,\text{Hz}$ the wall-clock running time is

$$t_{\text{wall}} \gg \frac{1}{r \cdot (50 \cdot 10^{-6} r_{\text{trig}})} = 20\,\text{s} \ , \tag{4.5}$$

where the relation $t = 50 \cdot 10^{-6} \times r_{\text{trig}} \times t_{\text{wall}}$ is used. Table 4.4.5 shows several t_{wall} values for various combinations of noise and trigger rates. Typical noise tests at UT ran for 20 to 30 minutes.

$r \times r_{\text{trig}}$	5 Hz	10 Hz	50 Hz	100 Hz
5 Hz	800 sec	400 sec	80 sec	40 sec
10 Hz	400 sec	200 sec	40 sec	20 sec
50 Hz	80 sec	40 sec	20 sec	4 sec
100 Hz	40 sec	20 sec	4 sec	2 sec

Table 4.5: Minimal wall-clock time for various combinations of noise and trigger rates.

4.4.6 Analysis Methods

Two steps are required to determine timing resolution from the MRPC cosmic ray data: (1) event selection, and (2) timing corrections, namely slewing corrections. In the following sections, the two parts are described sequentially.

4.4.6.1 Event Selection

The cosmic ray trigger is a coincidence between the CTB trays, and is independent of the MRPC modules. An additional constraint in selecting cosmic rays to require hits on MRPC pads. A reasonable minimal requirement is to have a vertical coincidence between the pads, 2-4 pads, depending upon the configuration being tested. Additionally, some events may be excluded for certain hit patterns, signal amplitudes or time-over-threshold (TOT) values. TOT is determined by subtracting the time of the trailing edge from the time of the leading edge. The

TOT of a hit is strongly correlated to the amplitude of the signal; therefore, we can use the TOT and signal amplitude almost interchangeably.

The maximum TOT method (MaxTOT) accepts events with one or more hits per MRPC, but only considers the single pad with the maximum TOT values on the MRPC, disregarding all the smaller TOT hits. A second requirement is that the maximum values must align vertically between all of the stacking modules. This method assumes that the largest TOT signal comes from the pad that the cosmic ray is nearest.

In order to further reduce the number of false cosmic events, a cap can be placed on the maximum number of pads that can "fire" in an event. Since an MRPC has 6 pads the intrinsic range of the number hits allowed by the MaxTOT method is $1 \leq N_{\text{hit}} \leq 6$. By introducing a new parameter, $N_{\text{hit}}^{\text{max}}$, we can exclude events out of the region $1 \leq N_{\text{hit}} \leq N_{\text{hit}}^{\text{max}}$. This filter is complementary to MaxTOT, and both are implemented in the analysis.

4.4.6.2 Slewing Correction

The TOT values have a slewing error from statistical fluctuations of the signal amplitudes generating them. The standard TDC-ADC correlation method is used to correct for slewing, except that we use the TOT values from our data in place of the normal ADC value.

An absolute time is not used in this analysis. The time difference calculated is the difference between the time of the signal from the pad of interest to the average time of the other(usually 3) pads vertically aligned above and/or below

the signal pad.

$$dt_{ij} = t_{ij} - \frac{1}{N-1}\sum_{k\neq i} t_{kj} \ , \tag{4.6}$$

where t_{ij} is time stamp of the j-th pad of the i-th module, and N is number of pads in the vertical direction. The value dt_{ij} is defined for each pad of the array for each event. We are interested in the fluctuation of this value. The time stamps' t_{ij} contain slewing errors that are dependent on the amplitudes of the signals. It is clear that dt_{ij} is dependent on multiple amplitudes because each term in the sum is dependent on a different amplitude. Instead of trying to solve for all of the dependencies at once, we apply individual corrections iteratively. First the correction for t_{1j} is estimated from the correlation plot dt_{1j} versus tot_{1j}.

$$t_{1j}^{(1)} = t_{1j} - f_{1j}(tot_{1j}) \tag{4.7}$$

Now all of the original values for t_{1j} are replaced by the value $t_{1j}^{(1)}$. Next we correct t_{2j} from the correlation of this new dt_{2j} and tot_{2j},

$$t_{2j}^{(1)} = t_{2j} - f_{2j}(tot_{2j}) \tag{4.8}$$

and so forth. Once all values in the j-th row are corrected, the same procedure is repeated using the corrected values and the higher order corrected values are obtained for $t_{ij}^{(2)}$, $t_{ij}^{(3)}$, and so on. In principle more iterations lead to more precise values; however we found in practice that all interations past the first did not improve the timing resolution. This is largely due to the statistical error on the fitting functions. All results discussed below use a single round of interations on the data.

Polynomial and exponential fits are used in the analysis discussed here; however, spline fits are used in the more recent STAR productions.[6]

$$f_1(x) = \sum_{i=0}^{n} a_i x^i \tag{4.9}$$

$$f_2(x) = a_0 + a_1 \exp(-a_2 x) \tag{4.10}$$

To obtain robust fits, it is necessary to restrict the region being fitted based on the quality and statistics of data. This range restriction is implented by only looking at one σ around raw TOT distributions. An example of both a TOT cut region and a fit region are shown in the Figure 4.18 as colored regions. In this example, the TOT cut region is 2σ and the TOT fit region is 1.5σ, where σ is the standard deviation of the original TOT distribution.

4.4.6.3 Correlation Method

After observing a significant amount of noise from cross-talk between modules, we began looking for ways to visualize and quantitatively describe the degree of cross-talk. We settled on using a Pearson correlation to describe the frequency of cross talk between any two given pads. Our observable is the binary variable, $h_i = 0, 1$, associated with the i-th pad, that either does (1) or does not (0) have a TOT signal. Using that input, the definition of the correlation is the following:

$$corr(i,j) = \frac{\langle h_i h_j \rangle - \langle h_i \rangle \langle h_j \rangle}{\sigma(h_i)\sigma(h_j)} \ , \tag{4.11}$$

where the bracket $\langle \cdot \rangle$ means average over all events. The correlation function of each pad pair is denoted by indices (i, j), is bounded by the region, $-1 \leq$

[6] TSplineFit http://gentit.home.cern.ch/gentit/litrani/AllModules/SplineFitCode/TSplineFit.html

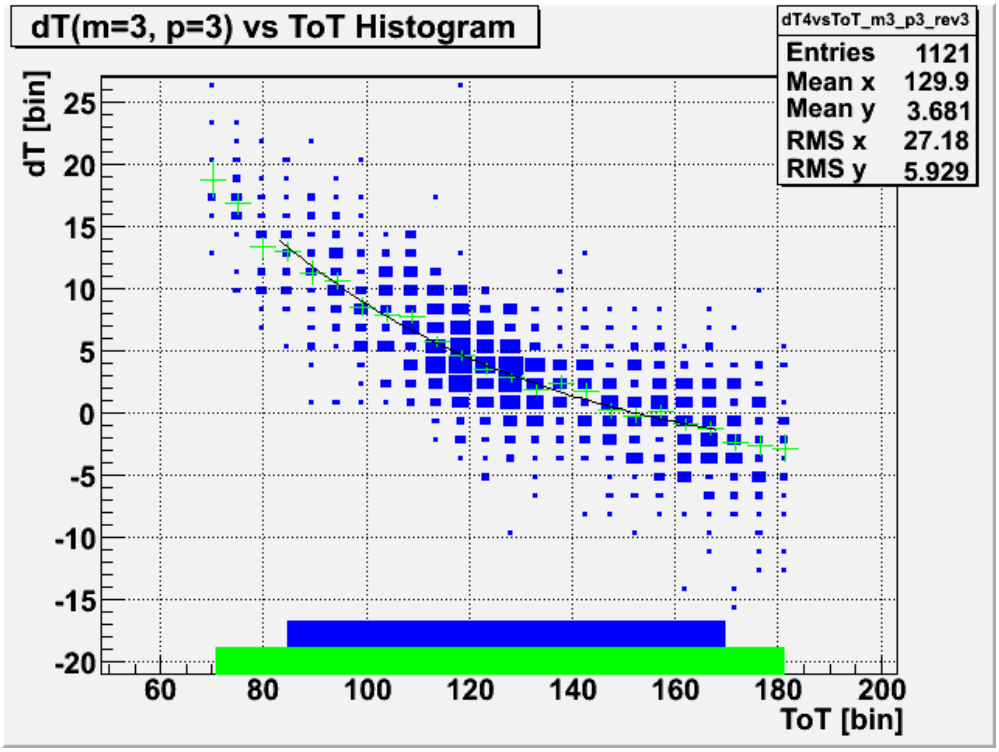

Figure 4.18: Regions used for slewings.

$corr(i, j) \leq 1$, and is normalized to unity on the diagonal elements where $i = j$, i.e. everything is perfectly correlated with itself. If each pad on a module was completely independent of the others, the function would be 0 for all non-diagonal elements. In the extreme case that all pads were electrically connected together, the values for the whole matrix would be unity (1) everywhere. In reality, the value varied between 1 to 0 gradually as they went further and further off-diagonal, visually creating a ridge shape in each module block. Larger scale correlation were also observed between pads on different modules for various reasons including: trigger condition, geometrical alignment, and cross-talk in electronics such as TINO and TDIG.

4.4.7 Results

As an example, a set of results from the cosmic ray tests, is shown here using data from run 10000352[7]. The run summary is listed in Table 4.6. The timing resolution for each pad on the module set in slot 2, *i. e.* the second module from top (TM0320[8]) is listed in Table 4.7. As can be seen in the table, a smaller number of tracks are found in the peripheral pads. This is due the edges seeing a smaller solid angle owing to the trigger acceptance.

Figure 4.19 shows the correlation plot for this run. There are 4×6 blocks in this plot corresponding to the array of four modules in the stack, each module with 6 channels. The diagonal correlations mean that the majority of hits occurred

[7] http://www.rhip.utexas.edu/~tofp/run/show.php?id=10000352
[8] http://www.rhip.utexas.edu/~tofp/module/show.php?sn=tm0320

Start Time	2007-08-09 16:45:37
Stop Time	2007-08-14 09:39:28
Running Time	406431 second
Total Events	250506
Average Event Rate	0.616 event/second
Total Tracks	3443

Table 4.6: Summary of Run 10000352.

	pad 1	pad 2	pad 3	pad 4	pad 5	pad 6	all
Number of tracks	466	604	775	658	556	384	3443
Timing resolution (ps)	83.9	65.1	70.9	75.5	66.3	94.2	74.4

Table 4.7: Detailed record of TM0320 in Run 10000352.

simultaneously in the vertically aligned pads. This indicates that the hits are likely caused by cosmic rays passing through the detector vertically. The width of the ridges indicates both the incidence angle of the cosmic rays and the cross-talk between channels. The broader light green region in module 2 indicates that it has more cross-talk than the other modules.

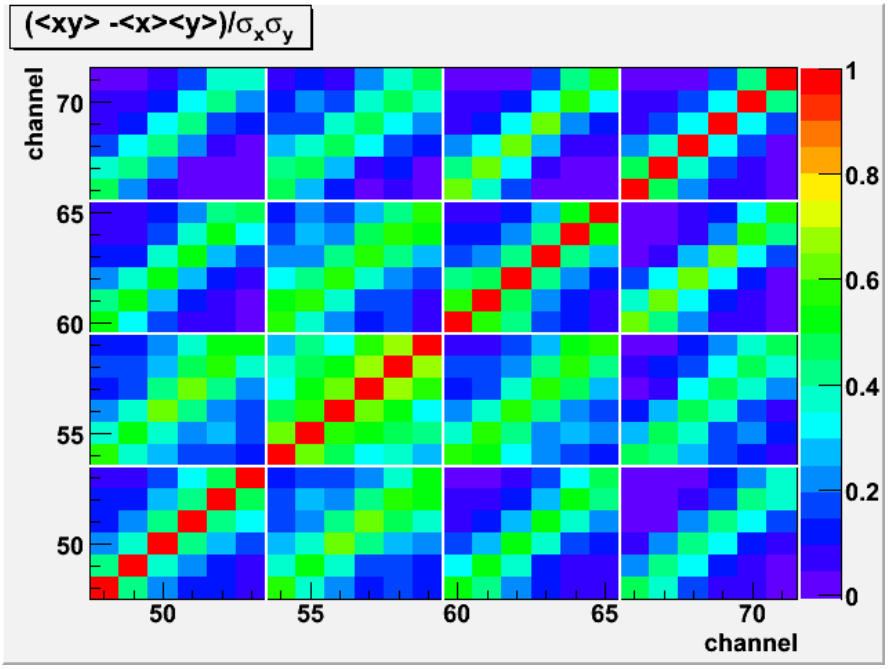

Figure 4.19: Correlation plot of Run 10000352. There is an offset of 48 in the channel numbering, so channel 48 corresponding to pad 1 of module 1, channel 49 to pad 2 of module 1, and so on.

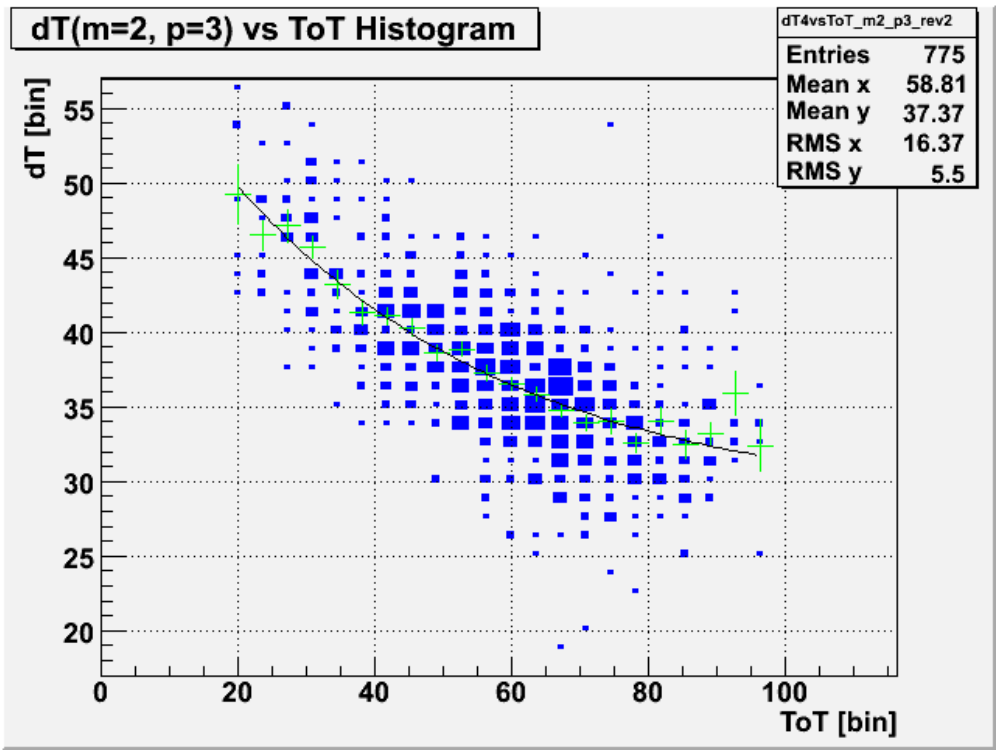

Figure 4.20: Slewing Correction in Run 10000352. One bin unit is 25/1024 ns in both axes (dT and ToT).

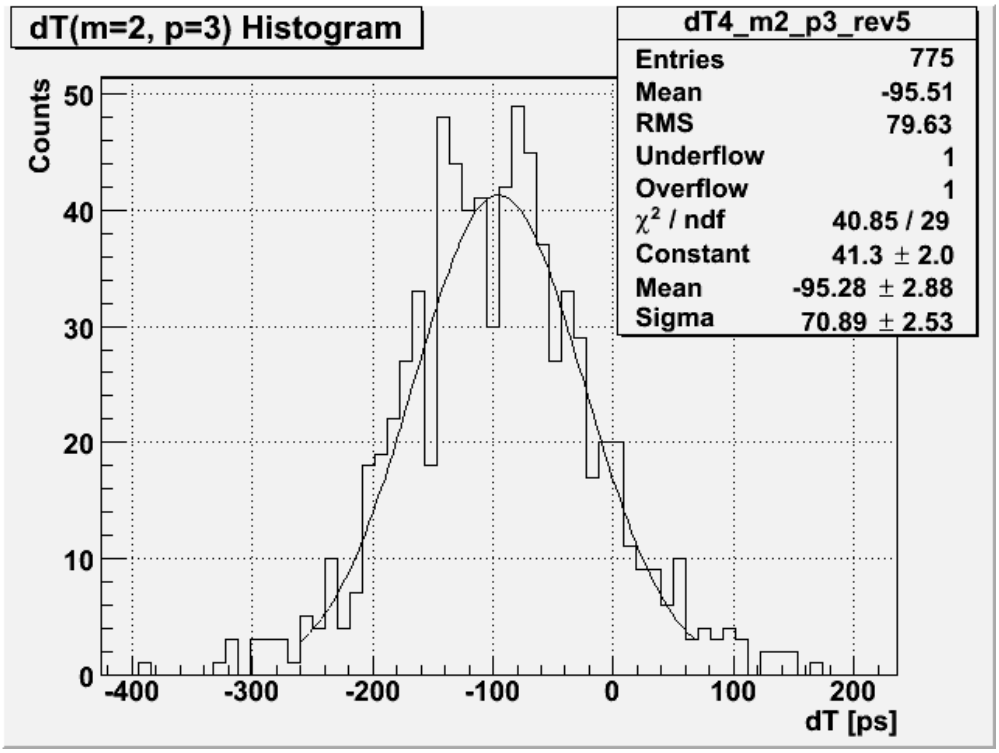

Figure 4.21: dT histogram of pad 3 of module 2 of Run 10000352 after slewing correction.

Chapter 5

Tray Assembly and Testing

5.1 Tray Assembly

All production STAR TOF trays were assembled at UT using parts gathered from multiple suppliers. MRPC modules were supplied by two Chinese Universities, Tsinghua University and the University of Science and Technology of China (USTC). Aluminum tray box sets consisting of bottom, top, cover, and feet were manufactured by Oaks Precision Fabricating, Inc. in Houston. Delivered box sets are shown in Figure 5.1. The TINO boards were designed at Rice University, manufactured by multiple vendors, and tested at Rice University before being shipped to UT. The TCPU and TDIG boards were designed and manufactured by Blue Sky Electronics, LLC. in Houston. The TDIG boards were calibrated at Rice, and calibration data (INL tables) were generated before being sent to UT. Since the INL tables are unique to each HPTDC chip on the TDIG board, it was important to keep record mapping between tray and TDIGs. Other parts including copper cooling loops with house fittings on each end, Lexan MRPC holders, shims, and cable strain relief blocks were designed at UT and manufactured by the UT machine shop.

Assembly steps are described below. A checklist (See Figure 5.2) was used

Figure 5.1: 126 aluminum tray box sets were amnufactured by Oaks Precision Fabricating, Inc.in Houston.

to make sure that every critical step in the assembly procedure was "checked" by someone other than the person who performed the procedure. The checklist had to be signed and dated. All important data, such as which MRPC modules, TCPU, TDIGs, and TINO boards are used in a particular tray, starting date, sealing date, etc., were stored in a database system developed and maintained by the UT group.

Tray Number:														
Module Type:														
Tray Assembly RLM 10.318	Clean Parts	Bottom (feet, UHMW, sealant, kapton)	Top (sealant, TINOs)	HV (polarity, soldering, fusion tape)	Tray Resistance (Ohms)	Tray Capacitance (Farads)	Ready for Final Seal	Cooling Loop Pressure Test	TINO LV Power/ Ground/ Pigtail	Cooling Loop, Shims, TDIGs, Spreaders	TCPUs	TDIG/TCPU Ribbon Cables/ Terminators / Jumpers	Strain Relief Block	Pressure Test with Magnehelic
Date/Time:														
Initials:														
														Leak Rate (in /hr):

Figure 5.2: Checklist for tray assembly.

The following are the main steps in assembling each tray:

1. Clean the aluminum tray box set to remove dust and grease. This process is important because the sealing processes require clean contacting surfaces.

2. Install two feet on tray bottom with aluminum rivets and seal rivets with Freon proof sealant (DC430). Four strips of Tefron tape are placed on the inner side of the feet and their opposite face of the tray bottom to reduce friction in sliding them into the STAR CTB/TOF slots.

3. Install bulkhead connectors for HV cables and gas tubes at high-eta side of a tray top. The contacting surfaces between the connectors and the top are filled with DC430 sealant. The gas connectors are installed with rotation cleats. Sealant is also placed on the bases of the embedded studs.

4. Install TINO boards on the tray top with nuts screwed onto the studs. The contacting surfaces between the TINOs and the top are filled with DC430. Figure 5.3 shows under surface of a tray top after this step.

5. Install two MRPC module holders on the other side of the tray top.

6. Install 32 MRPC modules into the holes on the holders which were installed in the previous step. Each 34-pin connector from a MRPC module is plugged into a male connector on under surface of a TINO board.

7. Connect positive and negative high-voltage cables, solder and form a positive and a negative HV-bus. Solder the two ends of the buses to the HV

connectors on the bulkhead. Solder all HV cable junctions and wrap with fusion tape for insulation. Fix the HV-buses with Kepton tape to reduce a chance of contact with the aluminum walls of the tray box. Figure 5.4 shows a tray top after this step.

8. Attach a 1/4" polyflow tray-length gas tube on inner side of the intake gas connector on the bulkhead.

9. Attach the tray bottom to the tray top and seal the junction with DC430. Heal the seal for about one week.

10. Install a cooling loop, a LV harness, 8 TDIGs, a TCPU, and data bus ribbon cables. Sandwich the cooling loop between the TINOs and TDIGs, and tighten nuts on the studs through the TINOs and TDIGs. The specification torque of the nut tightening is 4.5 inch-pounds. Figure 5.5 shows installing a TDIG at the lower-end of a tray.

5.2 Initial Tray Test

In this section a series of standard tests conducted before shipment is described. Typical results from actual tests are also included. One obsolete test, namely the RF test, is in the list for completeness.

5.2.1 Cooling Loop Leak Test

A cooling loop is installed between the TINO and TDIG cards on every STAR TOF tray. Chilled water flowing in the loop carries out heat from the TINO

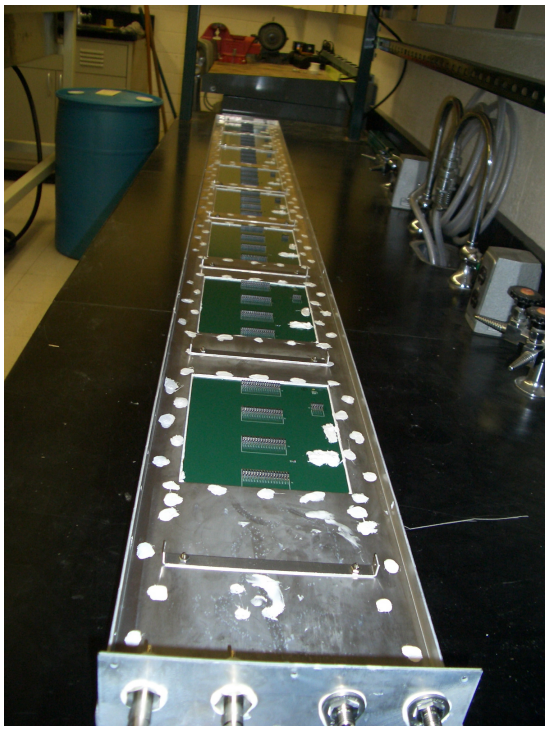

Figure 5.3: TINO boards are sealed and locked on a tray top. Bulkhead connecters for HV cables and gas lines are installed and sealed. Stud bases are sealed with DC430. Four male connectors on each TINO board for the MRPC signal cable connection are seen.

Figure 5.4: 32 MRPC modules are installed into the two Lexan module holders which stand vertically at the end of the box, and HV-cables are connected, wrapped with fusion tape, and fixed with Kepton tape.

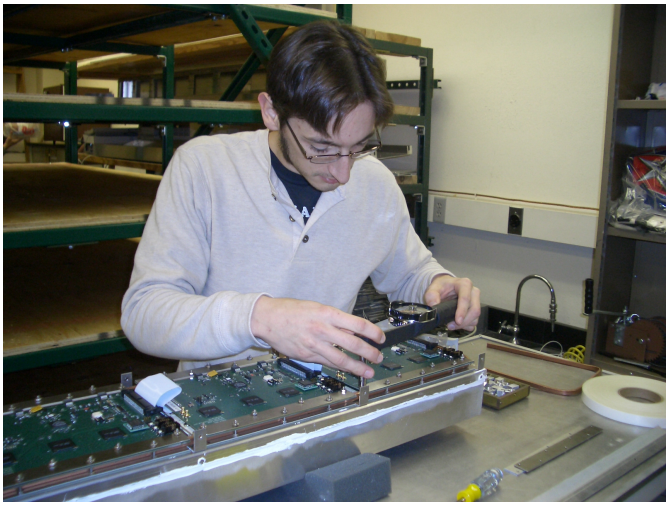

Figure 5.5: Installing TDIGs on TOF tray.

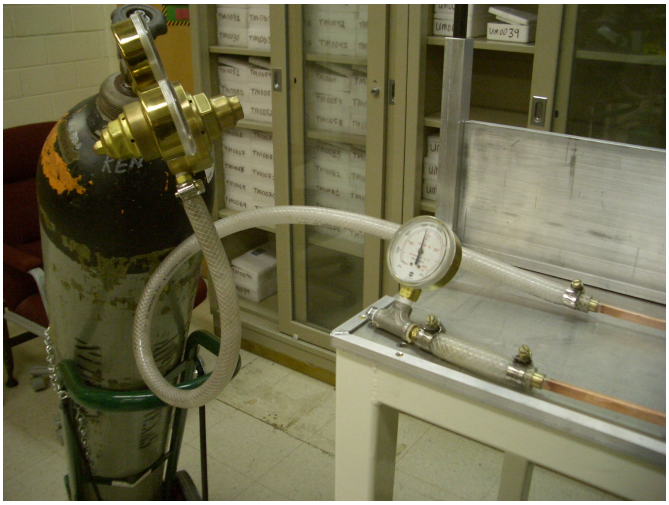

Figure 5.6: Cooling loop leak test with high pressure nitrogen.

and TDIG cards and keeps them in the appropriate temperature range. The loop is fabricated from 1/4"×3/8" copper tubing. A special bending tool was made for the sharp bends at the end of the tray. Brass barbed fittings are soldered on the ends. The fittings are located at high-η side of a tray. Every cooling loop is tested for leaks by submerging the loop in a water tank and pressuring the loop to 200 psi of nitrogen. If no bubbles are observed for two hours the loop passes the test. Figure 5.6 shows the setup for this test.

5.2.2 Tray Gas Leak Test

Each STAR TOF tray is filled with R134a freon and must be gas tight. The requirement is rigorous because freon leaks can affect the performance of other detectors in STAR. We have conducted two gas tests. The first test is to pressurize a tray and measure pressure as a function of time with a high precision pressure

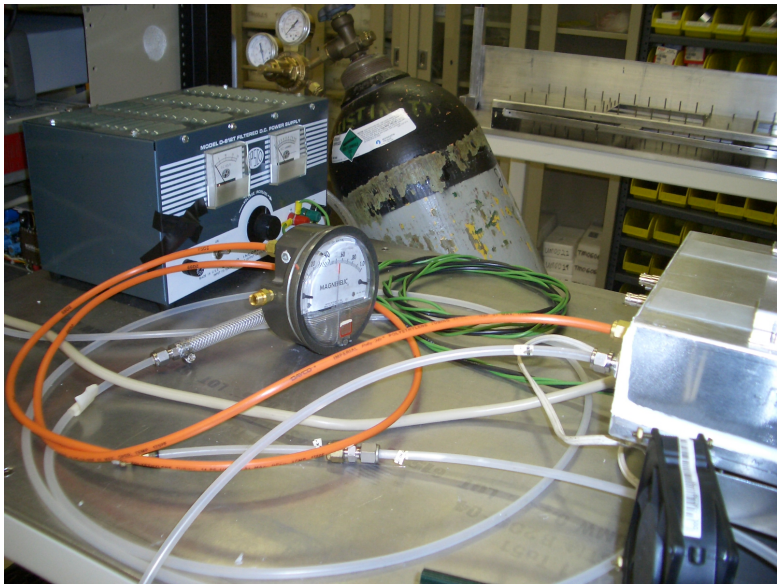

Figure 5.7: Picture of gas leak pressure test.

gauge (see the Figure 5.7). The measurements have to be stable after correcting for meteorological atmosphere pressure change over relatively long time, at least a day. The second test is filling the chamber with R134a freon and scanning all surface of the tray with a freon leak detector. The standard was that the sniffer did not alarm with its full sensitivity.

5.2.3 RF Test (obsolete)

The prototype (TOFr) and first batch of production trays are made with air-core transformers on the high voltage buses. Supplying RF pulses on the transformer generates RF waves in a tray box that acts as a wave guide and induce signals on the MRPC modules. Observing output from the TINO cards

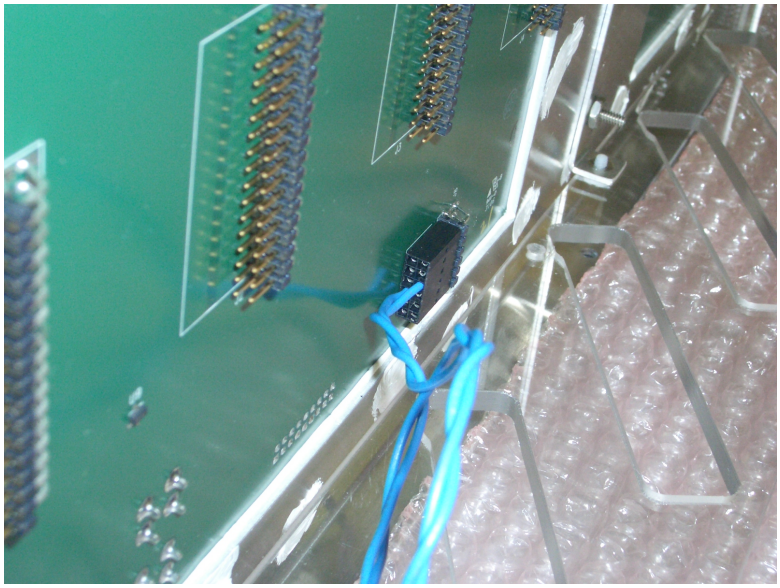

Figure 5.8: The air-core transformer for the RF test. Its blue cable will be laced in the high voltage buss. The green PCB is the TINO card from backside and the clear Lexan plate is the MRPC holder.

probes defects in the MRPCs and/or connection failures in the signal stream between there and MRPCs. The test was discontinued because we found some channels were not responding even though those channels had no problem during the production of the first five trays. Another reason is that this test is superseded by the tray level noise rate test and cosmic ray timing rest. One slight advantage of this test is that less preparation time is needed because it is not necessary to fill a tray with freon and apply high voltage.

5.3 Final Tray Testing at UT

5.3.1 Noise Rate Test

Noise rate tests at tray level were conducted in order to assure that all MRPC channels were active. Two methods used for the test are described in the following subsections.

5.3.1.1 Manual Measurement

As described in Section 3.3.4, a raw signal from an MRPC is discriminated by TINO and the TINO signal is passed to TDIG as a logic signal whose length corresponds to the time-over-threshold (TOT) of the raw signal. Therefore, noise rates of MRPC modules can be measured by counting the logic signals with a scalar via a read-out adapter shown in Figure 5.9. We used this method to measure noise rates for the first six trays (Trays A–C, 1–3) (beginning of tray production) while TDIG was still under construction. NIM scalars were readout manually and recorded. They are available in Excel format[1] on the UT TOF web under each tray's document section.

Figure 5.10 shows the results of the measurements on Tray A made on December 1, 2006. Pads are color coded as connector number (J5 – J7) on each TINO board in the figure.

Note that we found that some channels were, indeed, not active. In particular some versions of TDIG-F required a special extender on the connection

[1] e.g., http://www.rhip.utexas.edu/~tofp/tray/view.php?sn=A

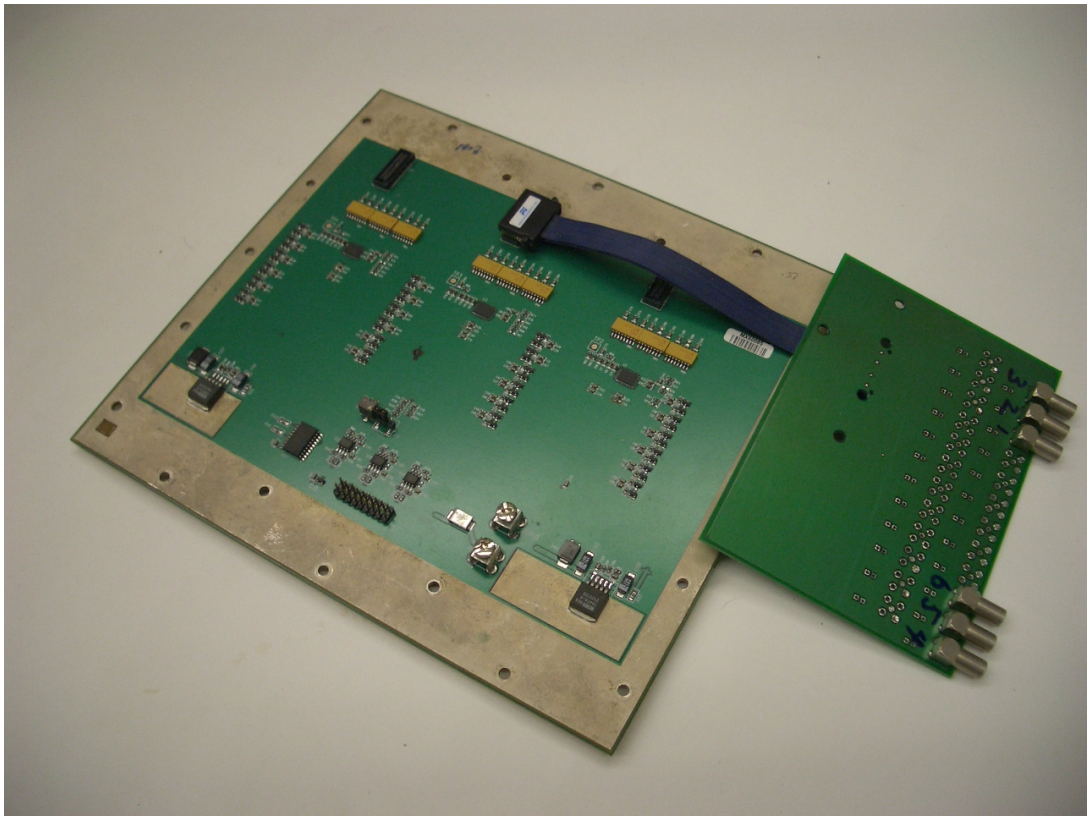

Figure 5.9: Read-out adapter is attached to TINO.

MRPC	Pad 1	Pad 2	Pad 3	Pad 4	Pad 5	Pad 6	TINO RPC #	TINO #	Connector
32	47	33	28	35	48	49	TINO-1		J5
31	24	20	20	17	19	22	TINO-2	8	J6
30	38	23	28	32	43	65	TINO-3		J7
29	38	20	21	22	25	35	TINO-4		
28	55	45	41	44	39	49	TINO-1		
27	49	43	50	48	48	43	TINO-2	7	
26	46	31	35	35	25	30	TINO-3		
25	29	35	41	48	38	40	TINO-4		
24	33	20	17	25	28	37	TINO-1		
23	37	29	33	39	38	45	TINO-2	6	
22	31	32	25	25	25	35	TINO-3		
21	24	18	24	28	30	44	TINO-4		
20	49	35	45	55	44	60	TINO-1		
19	30	30	31	32	24	30	TINO-2	5	
18	44	33	36	36	34	41	TINO-3		
17	44	31	37	38	42	39	TINO-4		
16	33	29	30	28	30	35	TINO-1		
15	33	29	29	25	26	26	TINO-2	4	
14	27	22	23	22	23	25	TINO-3		
13	34	23	23	17	23	27	TINO-4		
12	33	26	26	25	26	22	TINO-1		
11	30	24	30	32	30	24	TINO-2	3	
10	30	32	32	37	38	31	TINO-3		
9	28	25	24	20	26	29	TINO-4		
8	41	24	22	20	19	30	TINO-1		
7	46	26	25	23	22	42	TINO-2	2	
6	30	19	18	15	19	35	TINO-3		
5	23	20	26	21	20	22	TINO-4		
4	30	20	21	20	19	18	TINO-1		
3	23	15	13	16	19	28	TINO-2	1	
2	40	18	20	25	18	20	TINO-3		
1	34	22	20	23	20	30	TINO-4		

Figure 5.10: Manual noise measurement on Tray A taken on December 1, 2006.

between TINO and TDIG and missing them caused obvious dead channels (8 continuous). The color pattern in Figure 5.10 shows exactly the same pattern when one of the connections is lost.

5.3.1.2 Computerized Measurement

Once TDIG was installed and working properly, noise measurement were easier through counting hit packets from HPTDCs on TDIG. There are two ways to capture the packets: 1) using the regular data stream system up to THUB and connecting a DAQ PC and THUB with an optic fiber link, or 2) using the debug feature of TDIG with which data packets can be read out on the CAN-bus network, capturing the packets from the network with a DAQ PC. We used both methods according to situations. The former requires a complex setup, however, but has advantage in bandwidth and therefore can operate at higher trigger rate and/or with multiple trays simultaneously. The latter has exactly opposite features: it is simple but has less scalability. Since the bandwidth of the CAN-bus network is fairly limited, the trigger rate setting had to be lower than ≤ 180 Hz or less. We used internal trigger of THUB in the former setup and that of TCPU in the latter. Since HPTDC has preset timing window size Δt, average noise rate during a measurement r_{noise} were calculated from number of events n_{event} and packet count n_{count} as follows:

$$r_{\mathrm{noise}} = \frac{n_{\mathrm{count}}}{n_{\mathrm{event}} \cdot \Delta t}. \tag{5.1}$$

The window size is defined in TDIG firmware. $\Delta t = 25\,\mathrm{usec}$ for tray tests and $\Delta t = 5\,\mathrm{usec}$ for physics runs are nominal values.

Typical test results for Tray SN 3 in UT-Run 10000376[2] (September 28, 2007) are shown in Figure 5.11. Noise rates for module 13 are distinctly higher than those of others, and the tray average is higher than the specification. Throughout the entire project results for individual modules differed typically by this amount, but higher noise rates in early stages of testing eventually settled down. Unfortunately we didn't have enough time to observe the reduction in noise for the first five trays. We suspect that the freon purity in the tray is not good at first due to air contamination and out-gassing of the DC430 sealant and that it gradually gets better as time goes on, leading to lower noise rates. Another hypothesis is that avalanches/streams between the gaps of the MRPC modules burn dust on the resistive plates and that this leads to lower noise rates. We don't have clear evidence for the latter. Another remark is that we notice higher noise rates for peripheral pads than for middle pads. This trend has been seen throughout the project.

The example shown in Figure 5.12 suggests that the test is relevant for detecting defect in tray electronics. The module 28 of Tray 22 was inactive in the UT Run 10000640 and the following HV-reversed run revealed that polarity of the HV cables of the module was reversed.

5.3.1.3 Summary

We performed two types of tray-level noise rate tests for the 126 trays (24192 channels) assembled at UT. The minimum noise rates of all measured

[2]http://www.rhip.utexas.edu/ tofp/run/show.php?id=10000376

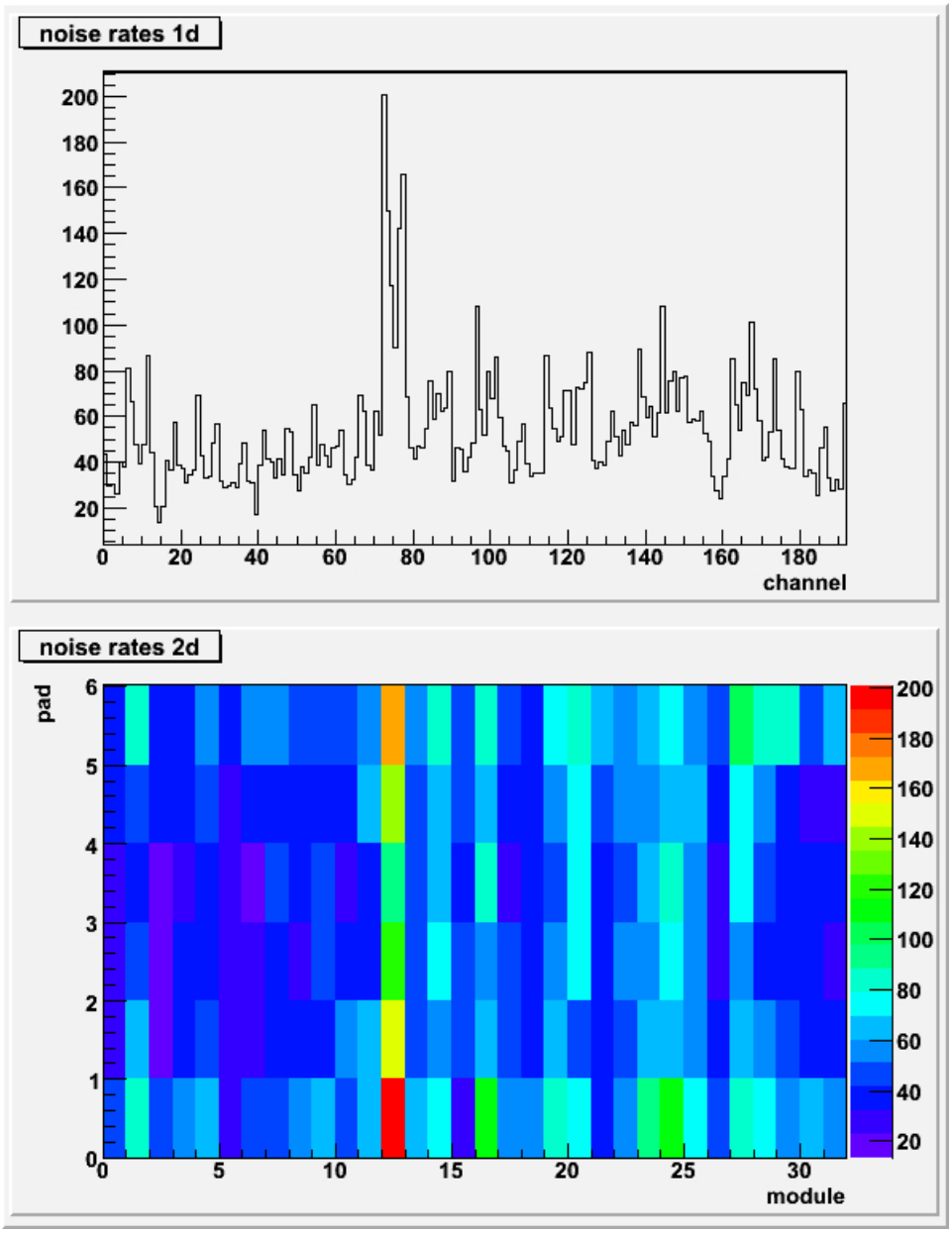

Figure 5.11: Noise rates from UT-Run 100000376. Upper panel shows 1d histogram and down panel shows color-coded 2d histogram. Unit of both histograms is Hz.

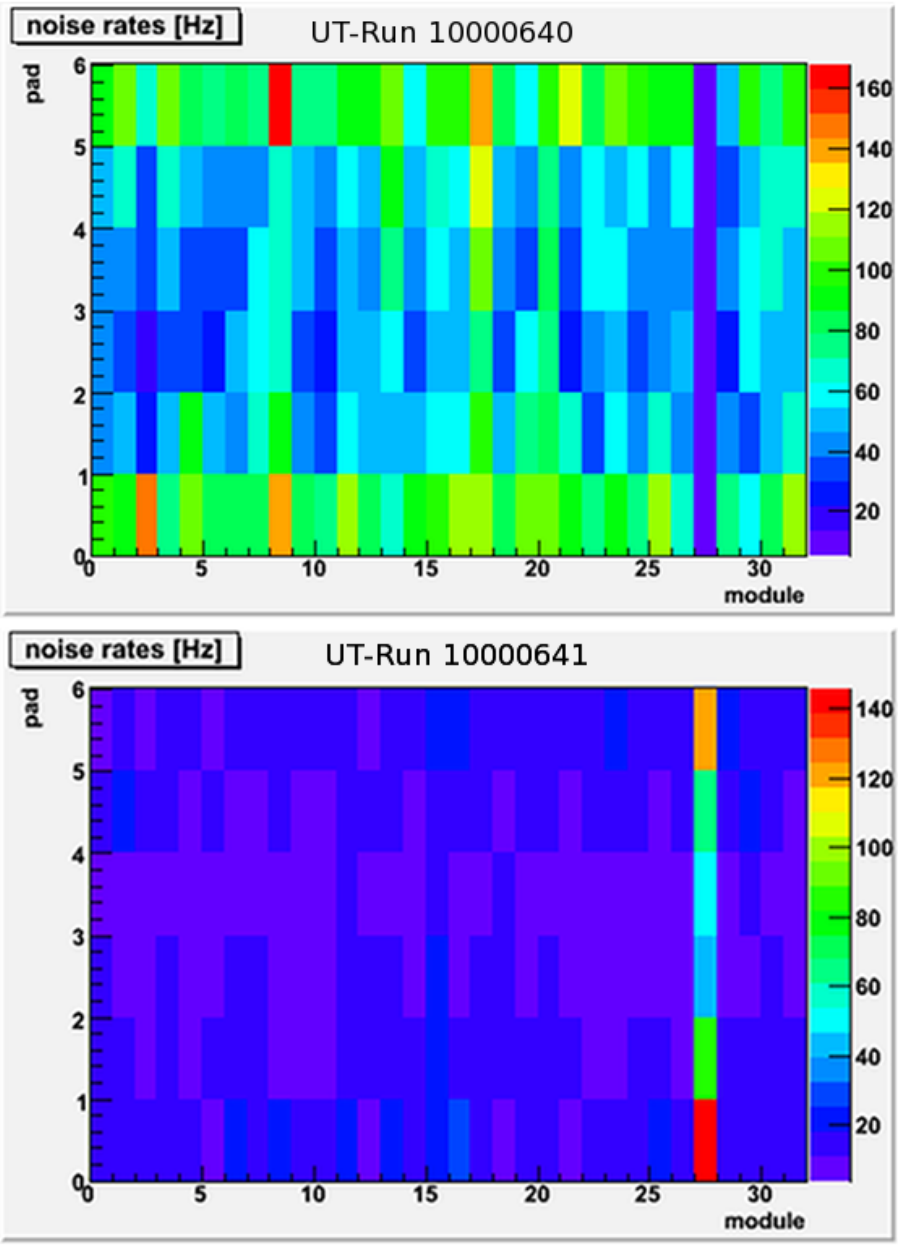

Figure 5.12: HV Polarity Comparison for Tray 22

channels with the computerized method and a histogram of the minimum values are shown in Figure 5.13. Channel number is coded as follows:

$$\text{channel} = 192 \cdot (\text{tray\_sn} - 1) + 6 \cdot (n_{\text{module}} - 1) + (n_{\text{pad}} - 1) \ , \qquad (5.2)$$

where tray_sn for Tray A, B, C is 124, 125, and 126 respectively. Table 5.1 shows all trays that have at least one channel whose reading was above 50 Hz. All results from the manual method and some earlier results from the computerized method are not included in the figure.

Note that results of this type of measurement are dependent on discriminator threshold settings. Higher threshold values make the noise rate lower and *vice versa*. We used 2500 mV throughout, except some for special cases, *e.g.* threshold dependence study. The measurements also depend upon gas purity and temperature; lower purity and higher temperature lead to higher noise rates.

The following assembly mistakes were found during the noise rate tests:

- Tray 8: HV leads of module 1 were connected opposite and two pairs of signal cables for module 3 were connected opposite.
- Tray 22: HV leads of module 28 were connected opposite.

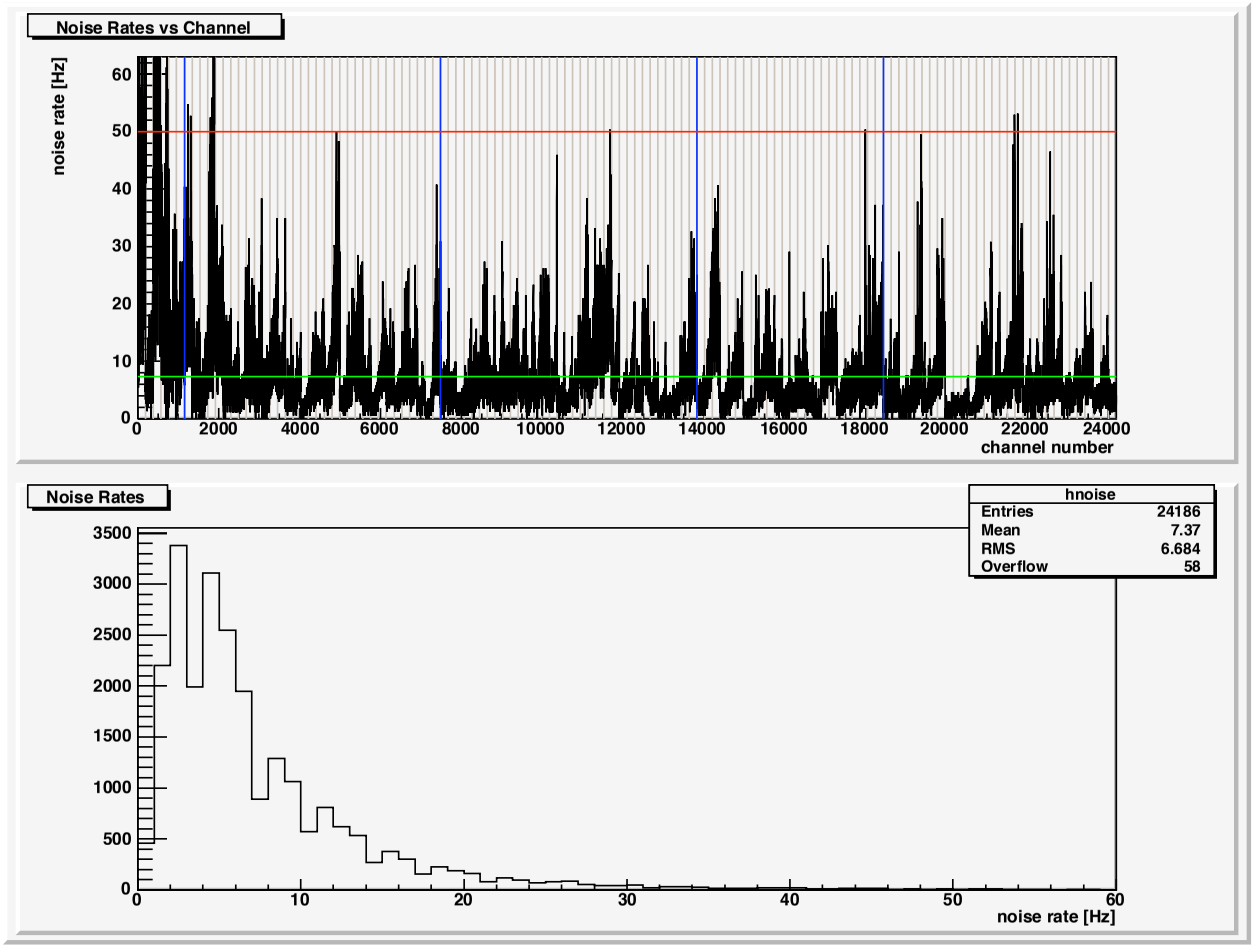

Figure 5.13: Minimum noise rates of all measured channel. The green and red lines in the upper panel show average value and specification requirement, respectively.

Tray SN	No. of Channels (> 50 Hz)	Note
1	40	0.7–36 Hz at BNL
3	27	2.5–172 Hz at BNL
4	7	21–41 Hz at BNL
7	2	3.5–31 Hz at BNL
10	20	1.1-13 Hz at BNL
26	1	
61	1	
94	1	
112	1	
114	1	
Total	101	0.417 % (101/24192)

Table 5.1: Trays with Noise Rates Greater Than 50 Hz

5.3.2 Cosmic Ray Test

The tray level cosmic ray test is conceptually the same as the cosmic ray test for MRPC modules described in Section 4.4. Figure 5.14 shows a block diagram of this setup, and Figure 5.15 shows a block diagram of the trigger circuit implemented in a NIM crate. We built two test stands. Figure 5.16 shows a picture the first test stand. It has 3 TOF trays and 3 CTB scintillators which generate a trigger as a 3-fold conincidence. The second stand, set up next to the first stand, has only two CTB trays, and a slightly different trigger system.

A summary of results from UT Run 10001303 is shown in Figure 5.17. It shows hit pattern, 3-fold coincidence track pattern, timing resolution of each channel, distribution of the timing resolution, channel correlation map, and packet ID distribution from top to bottom, and from left to right in the bottom row. With the hit pattern, the efficiency of each pad can be checked. The underlying pattern

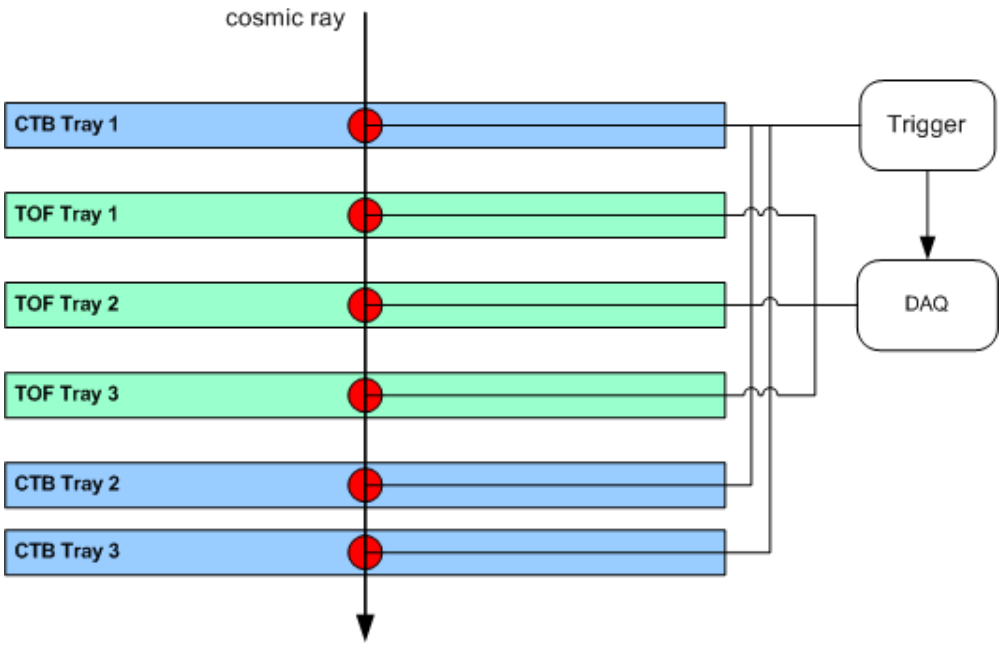

Figure 5.14: Schematic view of cosmic ray test setup.

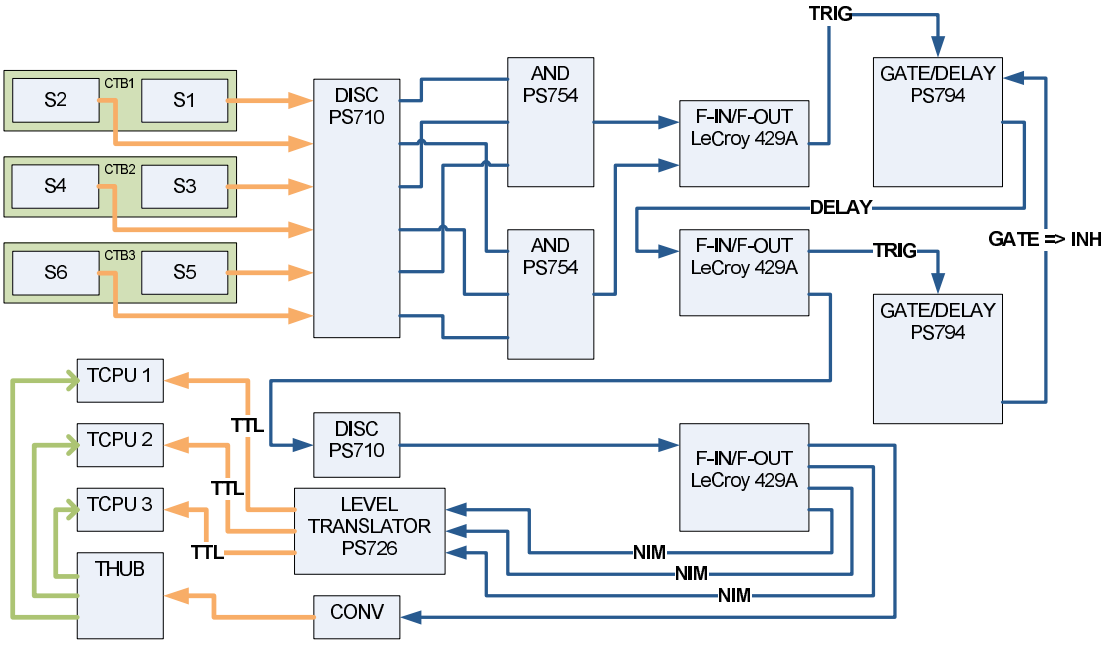

Figure 5.15: Block diagram of trigger circuit for cosmic ray test stand. Inverted gate from the second trigger module is used to make the first in busy state.

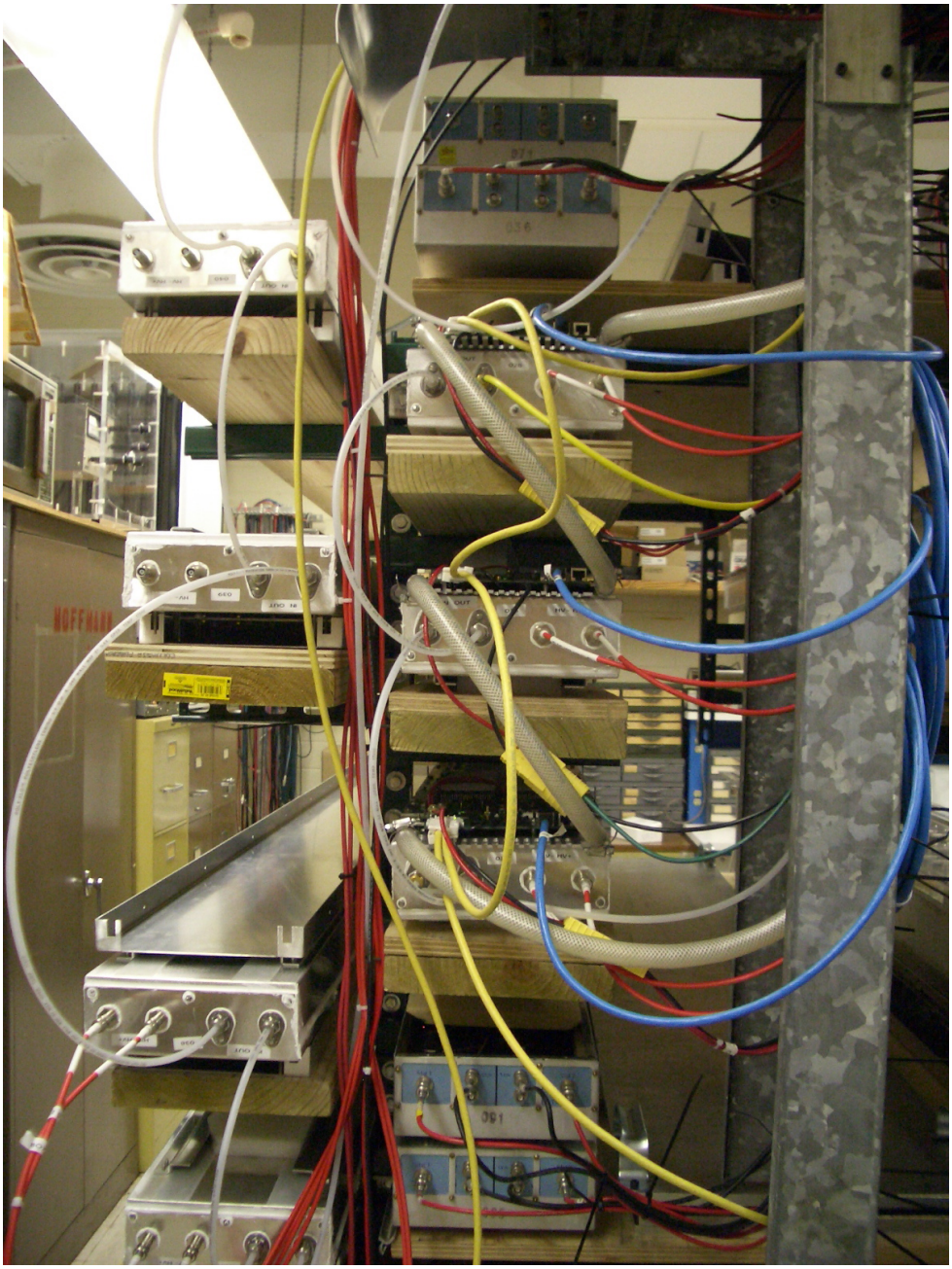

Figure 5.16: Cosmic Ray Test Stand.

with two distinct periods (6-channel and 96-channel) originates in the geometry of the test stand geometry for the TOF and CTB trays. The 6 pads on each MRPC module are aligned perpendicular to the TOF tray's long side, and peripheral pads have less solid angle as defined by the trigger geometry, *i. e.*, CTB trays are above and below the MRPCs. While almost vertical cosmic rays can see both peripheral and middle pads, cosmic rays tilted in the perpendicular direction can only see the middle pads because width of the CTB tray is about the same as that of the TOF tray. The same explanation explains the longer 96-channel period which originates in the geometrical trigger restriction from the two independent slats in each CTB tray. The 6-channel period can be seen in the 3-fold coincidence track figure. This plot is the most relevant for channel efficiency. The other plots are construed as explained earlier. The large values, 250–350 psec are the result of 1) absence of slewing correction and 2) large vertical displacement between modules. The latter allows a wide range of hit points on MRPC pads, and the difference of signal propagation paths on each pad broadens the time difference distribution. This effect is slightly balanced out when taking average of two time stamps from top and bottom, so the timing resolution of middle tray is smaller than for the top and bottom tray in general.

5.3.3 Summary

With two cosmic test stands we have tested and measured the timing resolution of 120 trays out of the total 126 trays assembled at UT. The 6 untested trays are A and 1–5. All measured timing resolutions are plotted in Figure 5.18

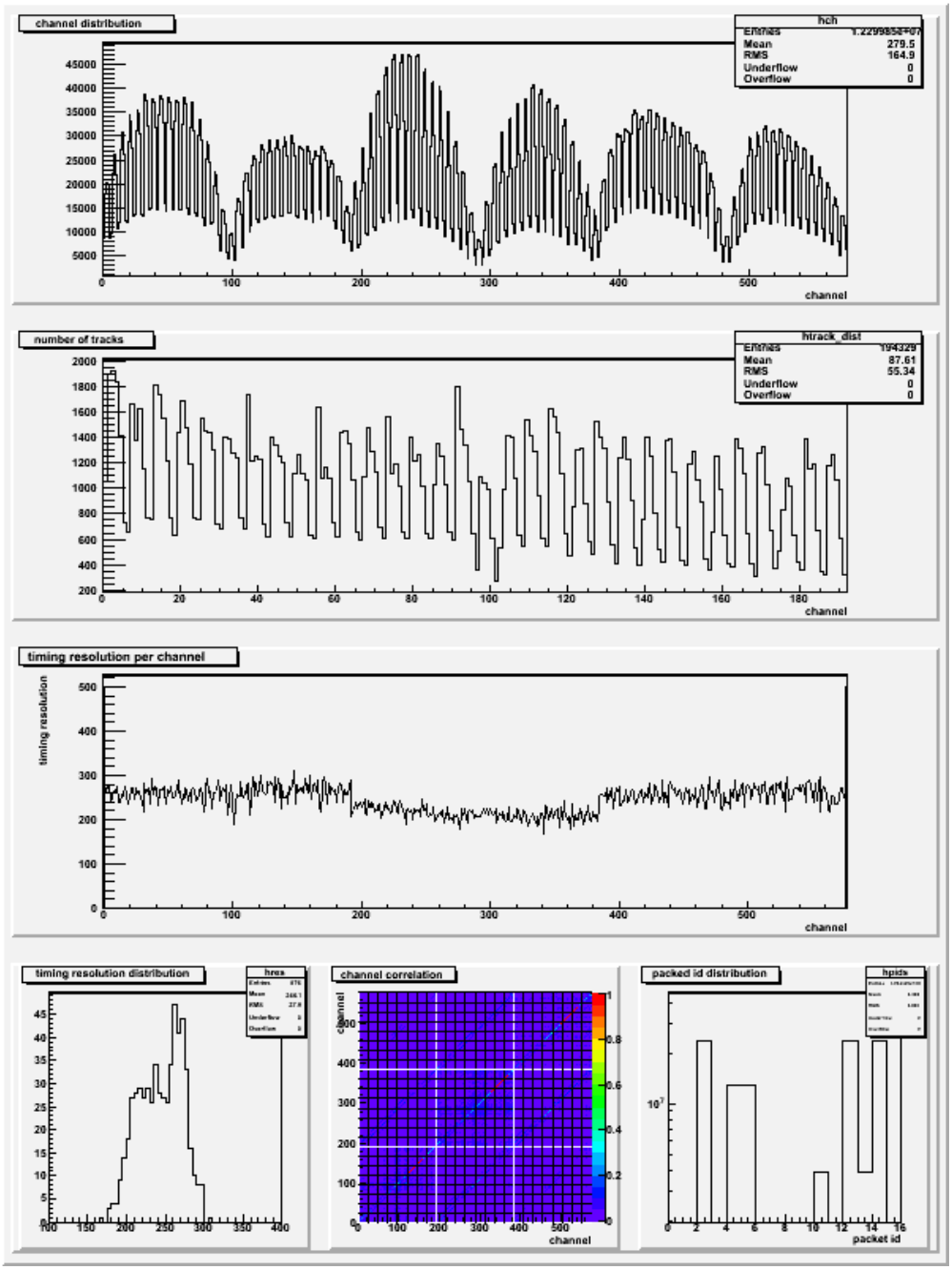

Figure 5.17: Summary Graph of UT Run 1001303.

where channel coding is the same as in Section 5.3.1. The test scheme itself was under development when the measurements were made for the first 12 trays, and their results do not correctly reflect the quality of these trays. Shorter run times and insufficient statistics was the main reason. Longer run times (1–2 weeks) gave better results.

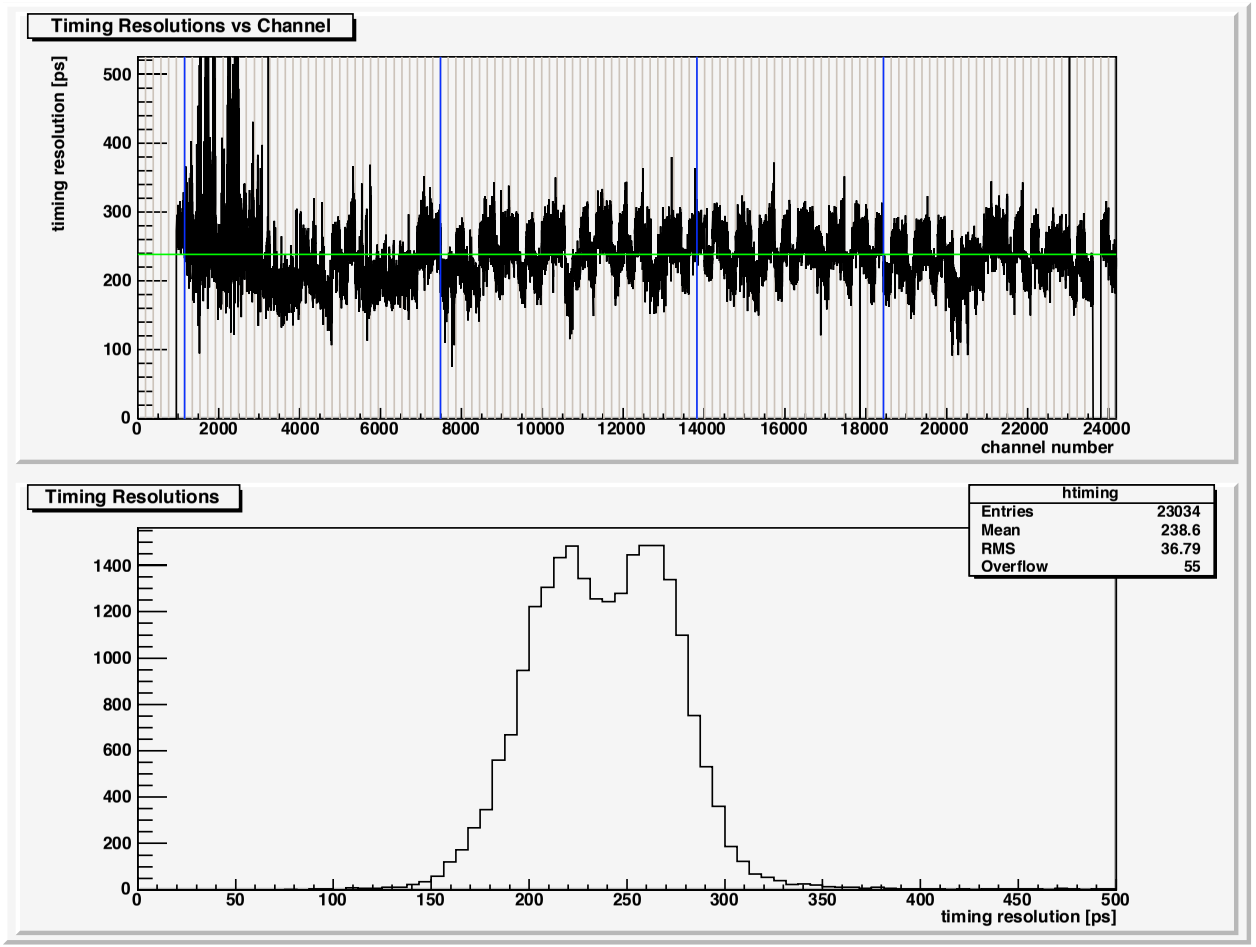

Figure 5.18: Minimum timing resolution for all measured channel. The green line in the upper panel indicates the average value.

5.4 Final Test at WAH

After transportation from UT to BNL another quick QA test at BNL was done. The trays were put on a test stand, and noise rates and high voltage currents were measured. Figure 5.19 shows a picture of the test stand. Results of the noise rate tests have been placed in the UT database. A summary of the noise rate test are show in Figure 5.20.

5.5 Miscellaneous Tests

5.5.1 Discrimination Threshold Scan Test

A discrimination threshold scan test was performed on Tray 114 at UT from January 21 to 22, 2009. As long as noise rate stays low and noise signals do not mask real signals, a lower threshold is preferable because it lead to higher efficiency. Although final optimization has to be done at STAR with actual tracks from collisions, this test was sufficient to establish a noise rate reference for a given threshold value for RHIC Run-9. Figure 5.21 shows tray average noise rate versus threshold from the test. The first run, UT Run 100001382 was at 2500 mV, and the following runs went down the x-axis by 100 mV. A total of 26 runs were conducted in succession at 1 hour/run. Except for the first two or three points, the data follow an exponential trend until about 300 mV. The first few points are suspect because the cooling system was turned on just before the first run, and the temperature of the system was higher than its stable value. The drop at the last two points is due to data overflow in electronics system.

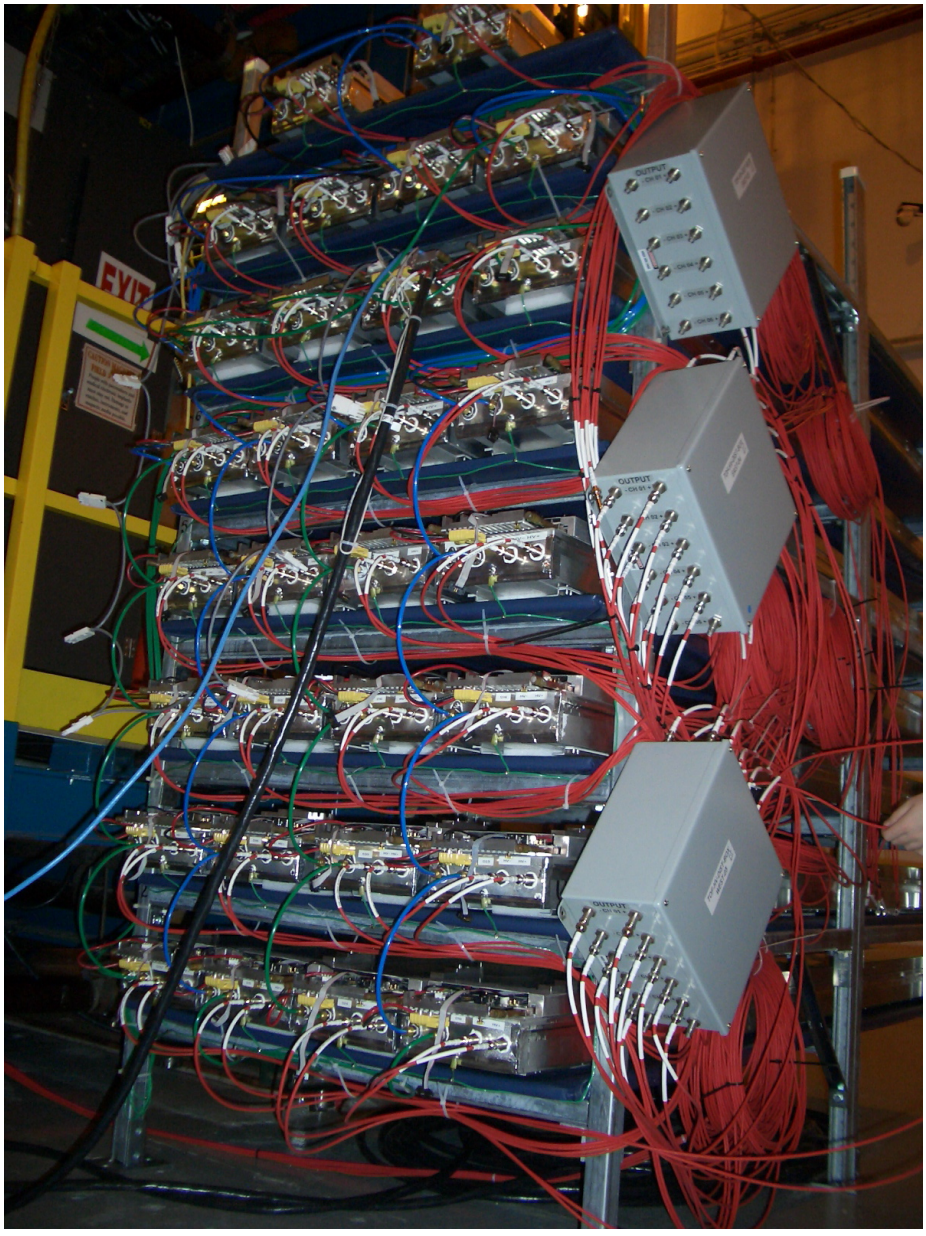

Figure 5.19: The test stand for final test at WAH. All 30 trays are connected with gas (green or blue polyester) tubes and HV (red) cables.

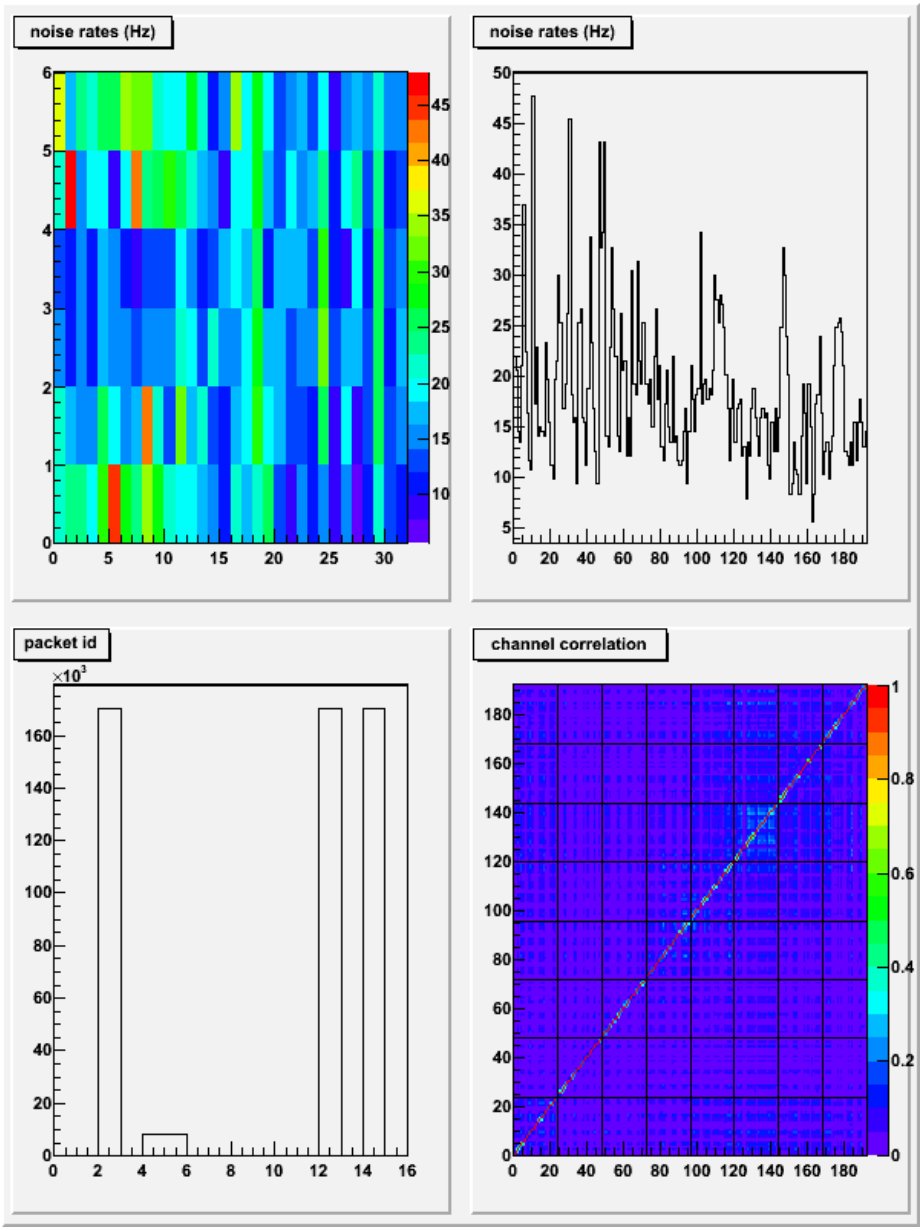

Figure 5.20: Summary of WAH noise rate tests; noise rates in 2d map (module no. × pad no.) (top-left), noise rates in 1d plot (top-right), packet id histogram (bottom-left), and channel-correlation plot (bottom-right).

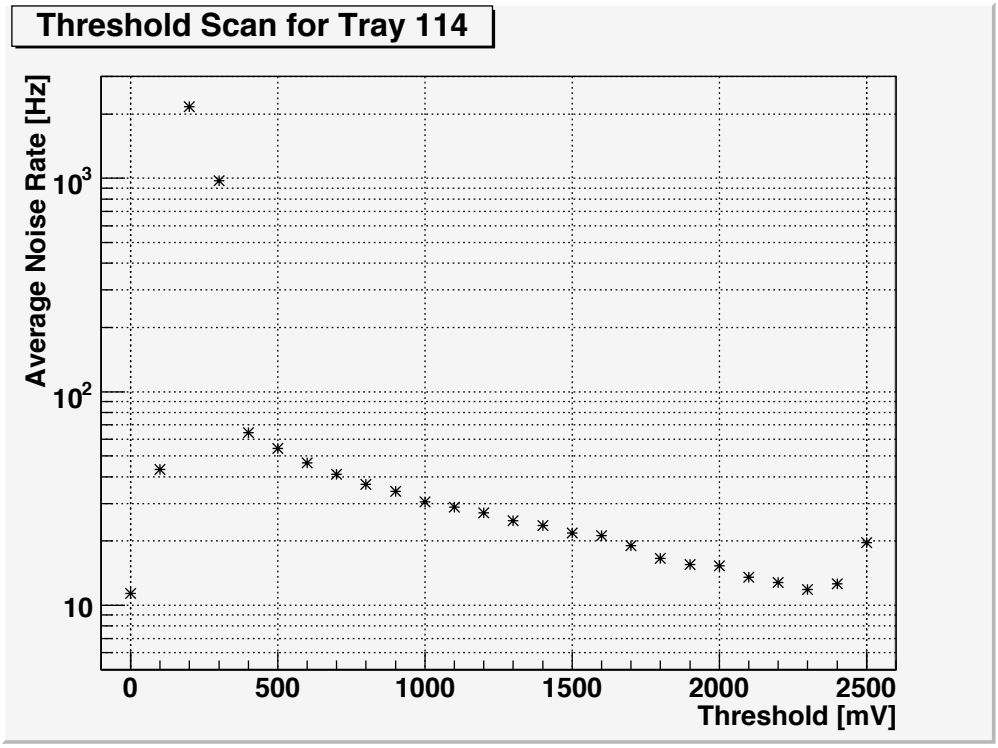

Figure 5.21: Threshold scan result for Tray 114.

Chapter 6

Status

As of August 7, 2009, all 126 TOF production trays were assembled and 122 of the 126 were equipped with production electronics. Trays A–C and 121–123 were assembled with a prototype aluminum body, and had to undergo slight modifications in order to mount the production electronics. A total of 125 TOF trays were delivered to BNL from UT over the course of 5 shipments beginning October 2007 and July 2009. A summary of the TOF tray shipments is shown in Table 6.1. Note that Tray 6 was originally delivered without TCPUs and TDIGs, returned to Texas, and the re-delivered in the third shipment.

For the RHIC Run 8, 5 trays (4.2 % of TOFs full design) were installed at STAR in the CTB/TOF positions 76–80. For Run 9, 94 trays (78 %) were installed at positions 1–12, 15–41, 44–72, 75-78, 97–101, 104-120. A map of STAR CTB/TOF positioning is defined in STAR TOF Note No. 229[33]. Currently eight slots (position 13, 14, 42, 43, 73, 74, 102 and 103) are left empty due to interference/obstruction from the STAR TPC support structures. A special fixture is under development to support the TPC detector without those structures so that they can be taken off and the TOF trays can be installed in those slots.

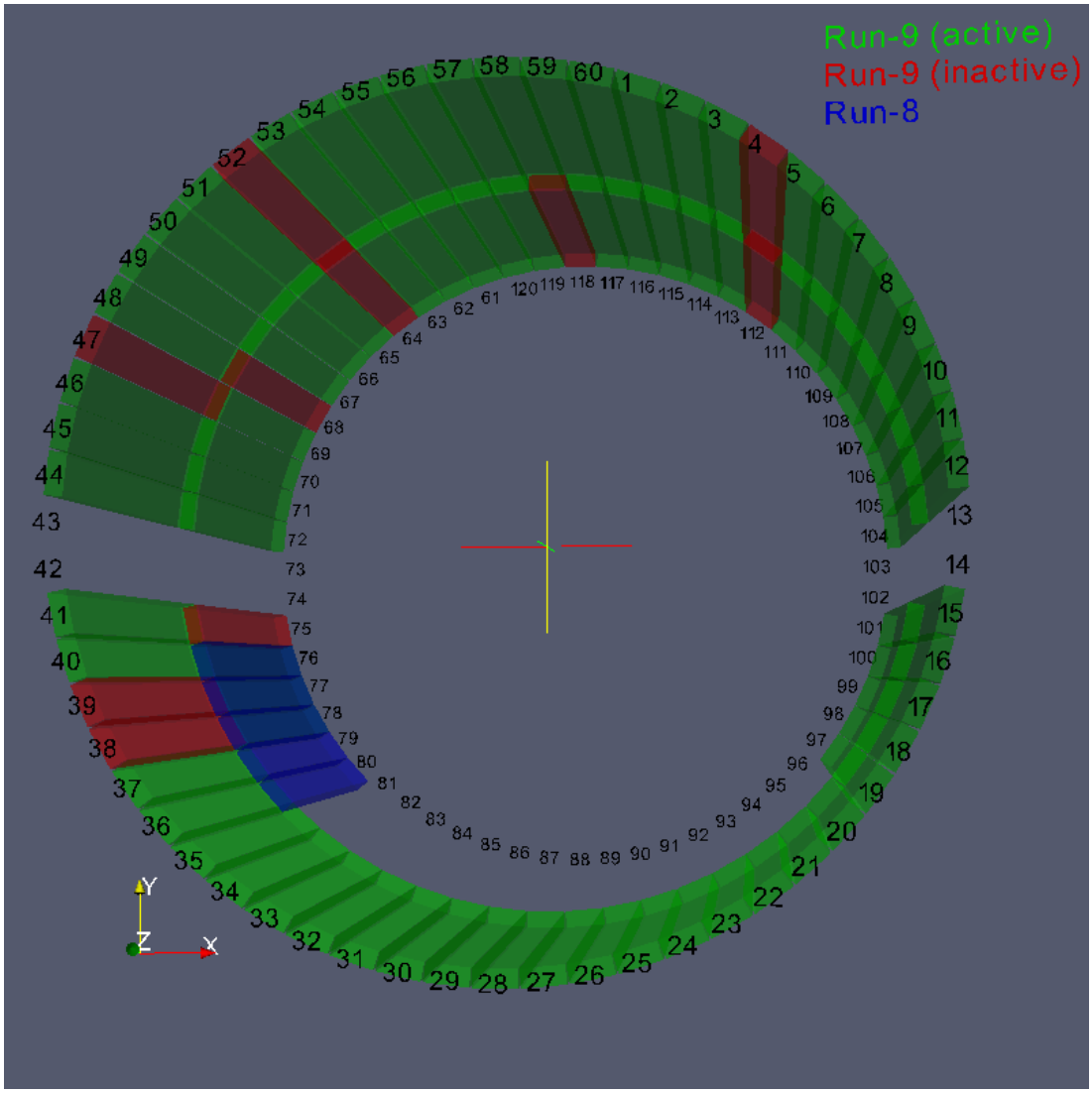

Figure 6.1: STAR TOF Configuration for Run 8 and Run 9.

No.	Date	Driver	No. of Trays	Catalog
1	Oct 5, 2007	D. Thein	6	Tray SN 1–6
		RHIC Run 8		
2	Jun 25, 2008	D. Thein	30	Tray SN 7–21, 23–25, 27–37, 39
3	Sep 18, 2008	G. Epply	32	Tray SN 6, 22, 38, 40–42, 45–55, 57–68, 70–72
4	Nov 17, 2008	D. Thein	27	Tray SN B, C, 43, 69, 78–87, 89–96
		RHIC Run 9		
5	Jul 9, 2009	D. Thein	31	Tray SN 26, 44, 56, 88, 97–123

Table 6.1: The Summary of TOF Tray Shipment

Position No.	Tray SN	Channel No.	Module No.	Pad No.
77	2	130	22	4
79	4	168	28	6

Table 6.2: Dead channels in Run 8.

6.1 Run 8

Two dead channels out of the 960 channels installed were found. Table 6.2 shows the specifics of those two channels. After Run 8 was complete, all TOF trays were uninstalled from STAR, and the TDIG boards for trays 1 and 2 were replaced. Also TDIG 4 of tray 49 was replaced from SN328 to SN254. Table 6.3 details which electonics boards were installed on the 5 trays before and after Run 8.

SN	Board	Run 8	Run 9	SN	Board	Run 8	Run 9
1	TCPU	145	145	4	TCPU	149	149
	TDIG 1	36	837		TDIG 1	70	70
	TDIG 2	26	838		TDIG 2	51	51
	TDIG 3	27	850		TDIG 3	75	75
	TDIG 4	29	852		TDIG 4	65	65
	TDIG 5	25	853		TDIG 5	76	76
	TDIG 6	23	862		TDIG 6	77	77
	TDIG 7	22	863		TDIG 7	71	71
	TDIG 8	21	864		TDIG 8	68	68
2	TCPU	146	146	5	TCPU	147	147
	TDIG 1	30	865		TDIG 1	46	46
	TDIG 2	31	884		TDIG 2	62	62
	TDIG 3	33	891		TDIG 3	72	72
	TDIG 4	35	896		TDIG 4	69	69
	TDIG 5	28	906		TDIG 5	61	61
	TDIG 6	32	913		TDIG 6	58	58
	TDIG 7	34	918		TDIG 7	42	42
	TDIG 8	37	910		TDIG 8	43	43
3	TCPU	148	148				
	TDIG 1	74	74				
	TDIG 2	63	63				
	TDIG 3	49	49				
	TDIG 4	73	73				
	TDIG 5	64	64				
	TDIG 6	53	53				
	TDIG 7	59	59				
	TDIG 8	52	52				

Table 6.3: Electronics board replacements before Run 9.

6.2 Run 9 Timeline

The following is the timeline of actions during Run 9. A summary of tray status given shown in Tables 6.4 and 6.5.

- Day 8 (January 8, 2009): The low voltage (LV) as well as high voltage (HV) distribution boxes number 2 and 3, were turned on in the afternoon. The first set of noise data was taken for STAR runs 1008033, 4, and 5. These data used a trigger matching window of 25 us and a discrimination threshold of 2500 mV. [NH-1630]

- Day 9 (January 9, 2009): A second set of noise runs was taken. Results indicated that there were HV problems for trays 15 and 32. [NH-1630/1]

- Day 12 (January 12, 2009): J. Schambach reported that he was unable to program the "bad" TCPU FPGA on tray 75. [NH-1631]

- Day 14 (January 14, 2009): L. Ruan *et al.* reported that they checked the 38 trays installed on the West side and found a small gas leak coming from the area near trays 97–100. They were able to track down and fixed the leak. [NH-1639/2]

- Day 16 (January 16, 2009): The East poletip of STAR was closed (the West poletip had already been shut on December 15, 2008). Several TOF pedestal runs with HV off were taken. [NH-1644]

- Day 22 (January 22, 2009): A small water leak was found in the TOF system caused by an incomplete clamp. The East pole tip was opened to fix the leak.

- Day 23 (January 23, 2009): All trays were powered up and a set of noise data was taken. We found that 1) trays 47, 49, 50, 51, 53, 54, 55, 56, 57, 58, 59, 60, 68, 112, and 118 in addition to the previous trays 15 and 32 had distinctly low noise rates, 2) tray 52 in addition to known problematic trays 38, 39 (bad LV connection), 75 (bad TCPU board) did not produce any hit signals, and 3) tray 46 showed distinctly high noise rate $\sim 50\,\mathrm{Hz}$. Note that trays 49–60 were connected to the HV distribution box 5. [NH-1650]

- Day 28 (January 28, 2009): L. Ruan *et al.* examined tray 52 and HV distribution box 5 and concluded "the problem for tray 52 is either the bad short HV cables or connection at tray end." It is worth to mention that the examination involved the disconnection/reconnection of all HV cables from/to the box "except the cable 54WPOS." [NH-1657]

- Day 30 (January 30, 2009): Another set of noise data was taken. From this we saw the problems on the trays connected to HV distribution box 5 were solved except for trays 52 and 54. [NH-1658]

- Day 36 (February 5, 2009): L. Ruan *et al.* swapped the HV polarity for trays 32 and 47 and took noise data in runs 100036044, 5, and 7. The attempt solved tray 32's problem but not tray 47. They switched back the cables at the end of the day. L. Li reported bunch id errors on tray 68. They

encountered an error on the 2nd fiber and reconnected the CAT-6 cable for pVPD East to port H0. [NH-1671]

- Day 43 (February 12, 2009): L. Ruan *et al.* swapped the HV polarity for trays 15, 32, 54, 68, 112, 118 and took some noise runs. The attempt solved the problems for tray 15, 32 (again), and 54 but failed for 112 and 118. Trays 66–78 could not be tested due to an optic fiber connection issue. [NH-1676]

- Day 50 (February 19, 2009): W. J. Llope *et al.* conducted the threshold scan study discussed in Section 6.3.1. [NH-1688]

- Day 53 (February 22, 2009): The first set of beam data was taken in runs 10053001–8. Dead channels were seen on trays 4 (6 channels), 10 (2), 60 (1), 63 (1) and 76 (1). The hit rates of tray 46 were significantly high. The four problematic trays 47, 68, 112 and 118 had significantly low hit counts. [NH-1694]

- Day 56 (February 25, 2009): The second set of beam data was taken in runs 10056164 and 165 with TPX. Tray 31 and first TDIG/TINO of tray 97 were missing. The electronics were not configured correctly. Two TOF pedestal with HV off were taken in runs 10056247 and 248. The LVs for trays 52 and 75 were left powered off since this day. The dead channels were still seen on trays 4 (6 channels), 10 (2), 60 (1), 63 (1) and 76 (1). The hit rates of tray 46 were significantly high. [NH-1700] [NH-1703]

- Day 58 (February 27, 2009): Several beam runs were taken with two different trigger settings with BBC and ZDC. Possibility of gas purity problem / leak

for one sector of trays, 111–115 was reported. The dead channels were still seen on trays 4 (6 channels), 10 (2), 60 (1), 63 (1) and 76 (1). The hit rates of tray 46 was significantly high. [NH-1709]

- Day 60 (March 1, 2009): A set of ZDC coincidence data was collected. The dead channels were still seen on trays 4 (4 channels), 10 (2), 60 (1), 63 (1) and 76 (1). The hit rates of tray 46 were significantly high. [NH-1712]

- Day 63 (March 4, 2009): Noise data was taken in runs 10063144, 145, and 146. [NH-1723]

- Day 64 (March 5, 2009): HV polarity of trays 68, 112, 118 was switched back to its original configuration. HV cables for Tray 47 were reconnected from HV4-11 to HV4-7. [NH-1729]

- Day 66 (March 7, 2009): East HV sectors 1 and 5 were turned off after run 10066169 due to poor gas quality and high HV currents. [NH-1732]

- Day 69 (March 10, 2009): Four runs were taken in runs 10069032–35. Trays 1–20, 51–60 were out of the run due to the THUB SW firmware problem. [NH-1733]

- Day 71 (March 12, 2009): The THUB SW was back in service after new FPGA firmware was uploaded. [NH-1738]

- Day 76 (March 17, 2009): The matching window was set to 5000 ns (200 coarse counts) and the trigger offset was set to 5200 nsec (208 coarse counts)

for the start electronics and to trays 66–72, 76–78 since run 10076027. The other trays still had the orignal match window 250025 ns (1001) with a trigger offset of 25225 ns (1009). Every tray was set to 5000 ns (200) and 5200 ns (208) before 10076113 in the evening. [NH-1742] [NH-1748]

- Day 77 (March 18, 2009): East HV sectors 1 and 5 were put back in the run. The HV cables were disconnected for trays 68, 112 and 118. [NH-1751]

- Day 78 (March 19, 2009): A set of noise data was taken in runs 10078007-011. The low-η half of tray 61 showed significantly low noise rates. Trays 9, 10, 61–65, 77, 110, 113–115, 117, 119, 120 showed high noise rates. Tray 47 was not functioning correctly. [NH-1753]

- Day 85 (March 26, 2009): A set of beam data set was checked by the TOF analysis group. The dead channels were still seen on trays 4 (6 channels), 10 (1), 60 (1), and 76 (1). Note that one dead channel on tray 60 and tray 63 which had been observed in previous runs looked normal.

- Day 87 (March 28, 2009): In beam runs 10087041, 51, and 63, the dead channels were still seen on trays 4 (6 channels), 10 (1), 60 (1), and 76 (1).

- Day 89 (March 30, 2009): In beam run 10089023, the dead channels were still seen on trays 4 (6 channels), 10 (1), 60 (1), and 76 (1).

- Day 91 (April 1, 2009): The HV cables for tray 47 were disconnected and the tray is out of run since run 10091070. Noise data was taken in runs 10091070–73 with the HV on and 74–77 with the HV off. [NH-1774]

- Day 96 (April 6, 2009): New TCPU firmware was installed on the trays 19, 20, 27, 28, 37, 66, 67, 69, 70, 71, 72, 78 and both start detectors. The update was done for fixing a HPTDC problem which happens when it receives a trigger command too close to a clock edge. The first run with the firmware was run 10096139. [NH-1784]

- Day 98 (April 8, 2009): The new TCPU firmware was installed on all trays. The first run with the firmware was run 10099055. [NH-1784]

- Day 105 (April 15, 2009): Two noise rate runs 10105009 and 10105017 were taken. Trays 10, 37, 50, 76, 77, 110, 114, 117, 120 seemed to have higher noise rates than 50 Hz. [NH-1789]

- Day 109 (April 19, 2009): Two 200 GeV commissioning runs were taken in runs 10109062 and 10109063.

- Day 133 (May 14, 2009): Two noise rate runs 10133078 and 10133079 were taken at the end of the access. [NH-1818]

- Day 139 (May 20, 2009): The TDIG 7 MCU of tray 64 became corrupted while downloading a new firmware. The tray LV was kept off. [NH-3281]

- Day 159 (June 8, 2009): Tray 4 was taken out of the run due to electronics errors.

- Day 195 (July 14, 2009): T. Nussbaum and G. Eppley investigated the physical connection of the LV and HV cables after shutdown.

- Trays 38 and 39 had no LV connection since west poletip was closed.
- Tray 47 appeared to be connected properly. To check short cables, tray-48 cables were connected to tray 47.
- Tray 52 was connected but neither HV cable was mated (locked).
- Tray 68 appeared to be connected properly. To check short cables, tray-68 cables were connected to tray 69.
- Tray 112 was not connected with positive HV cable.
- Tray 118 was not connected with positive HV cable.

Noise data was taken after this investigation and it was found that trays 47, 68, 112, 118 were fine while trays 38, 39, 52 remained non-functional, probably because the new firmware was not uploaded for those trays. Trays 77, 117 and 120 which showed high noise rates during the run were uninstalled from STAR and sent back to UT for repair. Trays 4, 58, and 64 were uninstalled and intalled with new electronics boards. It was decided that tray 75, which needs a new TCPU, would not be removed until the TPC support is removed. Trays 112 and 118 were removed to take out trays 4 and 58. Trays 5 and 47 were reported to not respond to TCPU MCPU programming. [NH-1882]

6.3 Run 9 Results

The hit count per tray of Run 10087063 (March 28, 2009) is shown in Figure 6.2. The flat trends of the tray maximum (green box), tray average (black

Pos.	SN	HV	9	23	30	36	43	50	53*	56*	58*	63	77	79
4	6	1-4	-						d	d	d		-	
10	60	1-10	-						d	d	d		-	
15	63	2-3	L	L	L	L							-	
31	8	3-7								D			-	
32	20	3-8	L	L	L								-	
38	29	4-2	-	O	O	O	O	O	O	O	O	O	O	O
39	34	4-3	-	O	O	O	O	O	O	O	O	O	O	O
46	23	4-10	-	H	H	H	H	H	H	H	H	H	-	
47	32	4-11	-	L	L	L	L	L	L	L	L	L	-	O
49	24	5-1	-	L									-	
50	18	5-2	-	L									-	
51	59	5-3	-	L									-	
52	66	5-4	-	D	D	D	D	D	D	O	O	O	O	O
53	70	5-5	-	L									-	
54	38	5-6	-	L	L	L							-	
55	41	5-7	-	L									-	
56	45	5-8	-	L									-	
57	52	5-9	-	L									-	
58	54	5-10	-	L									-	
59	53	5-11	-	L									-	
60	55	5-12	-	L					d	d	d		-	
63	94	6-3	-						d	d	d		-	
64	91	6-4	-										-	
68	22	6-8	-	L	L	LB	-	L	L	L	L	L	O	O
75	1	7-3	-	O	O	O	O	O	O	O	O	O	O	O
76	4	7-4	-						d	d	d		d	
77	3	7-5	-											
97	77	9-1	-							P			-	
112	79	10-4	-	L	L	L	L	L	L	L	L	L	O	O
118	92	10-10	-	L	L	L	L	L	L	L	L	L	O	O
120	78	10-12	-							P			-	

Table 6.4: Summary of problematic trays; B=bunch ID error, D=dead, L=low noise rate/hit counts, H=high noise rate/hit counts, O=out of the run, P=partially dead, d=dead channel.

Pos.	SN	HV	112*	139	159	195
4	6	1-4	d	-	O	U
10	60	1-10		-	-	
15	63	2-3		-	-	
31	8	3-7		-	-	
32	20	3-8		-	-	
38	29	4-2	O	O	O	
39	34	4-3	O	O	O	
46	23	4-10		-	-	
47	32	4-11	O	O	O	
49	24	5-1		-	-	
50	18	5-2		-	-	
51	59	5-3		-	-	
52	66	5-4	O	O	O	
53	70	5-5		-	-	
54	38	5-6		-	-	
55	41	5-7		-	-	
56	45	5-8		-	-	
57	52	5-9		-	-	
58	54	5-10		-	-	U
59	53	5-11		-	-	
60	55	5-12	d	-	-	
63	94	6-3		-	-	
64	91	6-4		O	O	U
68	22	6-8		-	-	
75	1	7-3	O	O	O	
76	4	7-4	d	-	-	
77	3	7-5		-	-	U
97	77	9-1		-	-	
112	79	10-4	O	O	O	U
118	92	10-10	O	O	O	U
120	78	10-12				U

Table 6.5: Summary of problematic trays; B=bunch ID error, D=dead, L=low noise rate/hit counts, H=high noise rate/hit counts, O=out of the run, P=partially dead, U=uninstalled, d=dead channel.

inverted triangle), and tray minimum (blue triangle) plots indicate that all of the working trays except for four are in healthy state in terms of efficiency cross-talk. The four trays with significantly lower minimum values, at positions 4, 10, 60 and 76, have one or more dead channels.

Figure 6.3 and Figure 6.4 are raw hit patterns for Tray 4 from the Run 10087063 represented as a 1d histogram and 2d histogram respectively. As the figures shows, there are 6 dead channels in Tray 4. The sequential channel numbers (module number, pad number) of the dead channels are 43 (8, 1), 71 (12, 5), 72 (12, 6), 80 (14, 2), 106 (18, 4), and 108 (18, 6). The exact same analysis performed on other trays revealed that there was only one dead channel on each tray. A summary of the dead channel search is presented in Table 6.6. The total number of dead channels is 9 out of 16152 channels (from the 86 installed trays that were functional). The rate of occurrence is an impressive 0.55%.

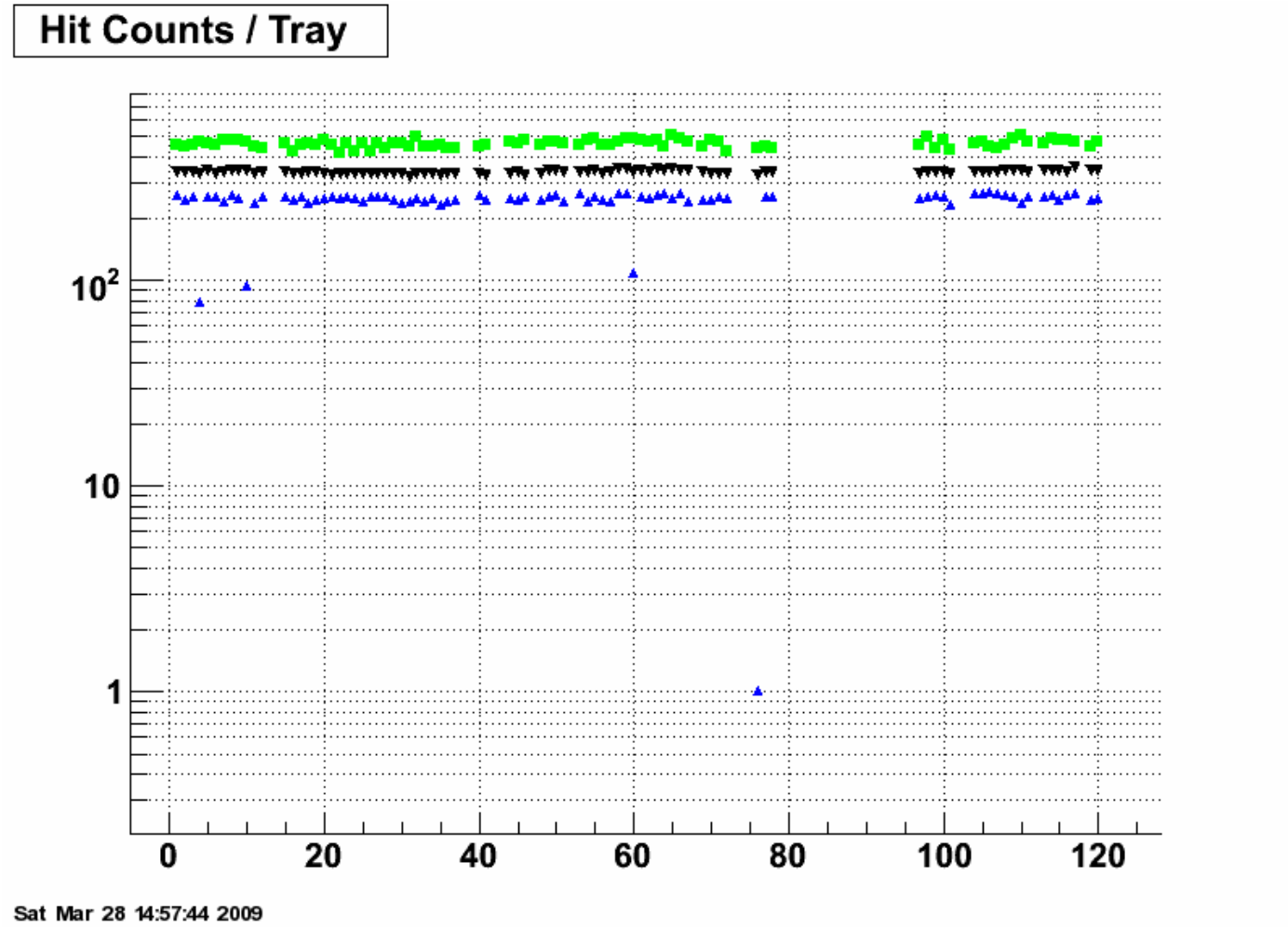

Figure 6.2: Hit counts per tray of run 10087063; green box, black inverted triangle, blue triangle represents tray maximum, tray average, tray minimum respectively. Four trays, at position 4, 10, 60, and 76, have one or more dead channels.

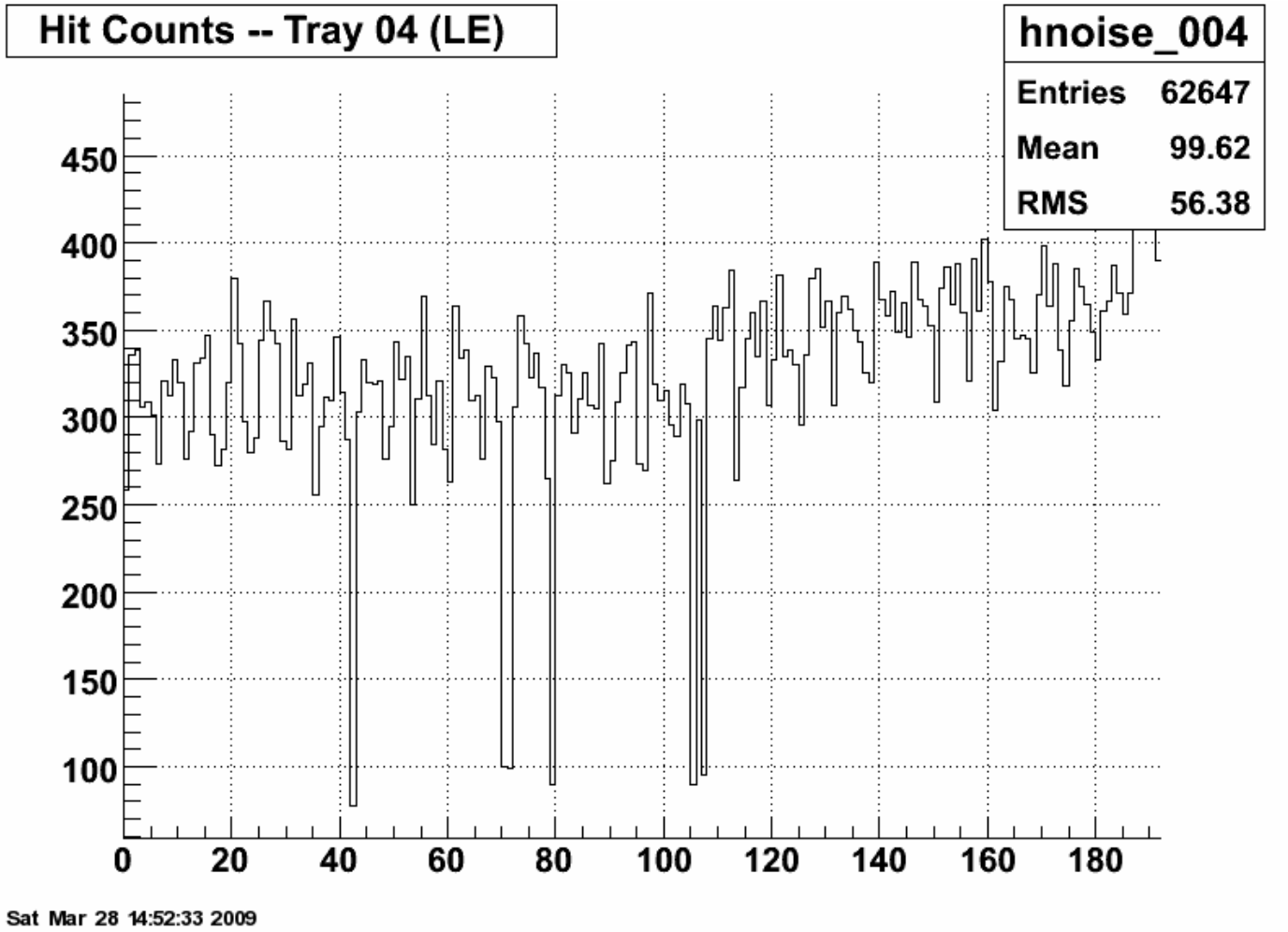

Figure 6.3: Hit pattern on tray 4 of Run 10087063.

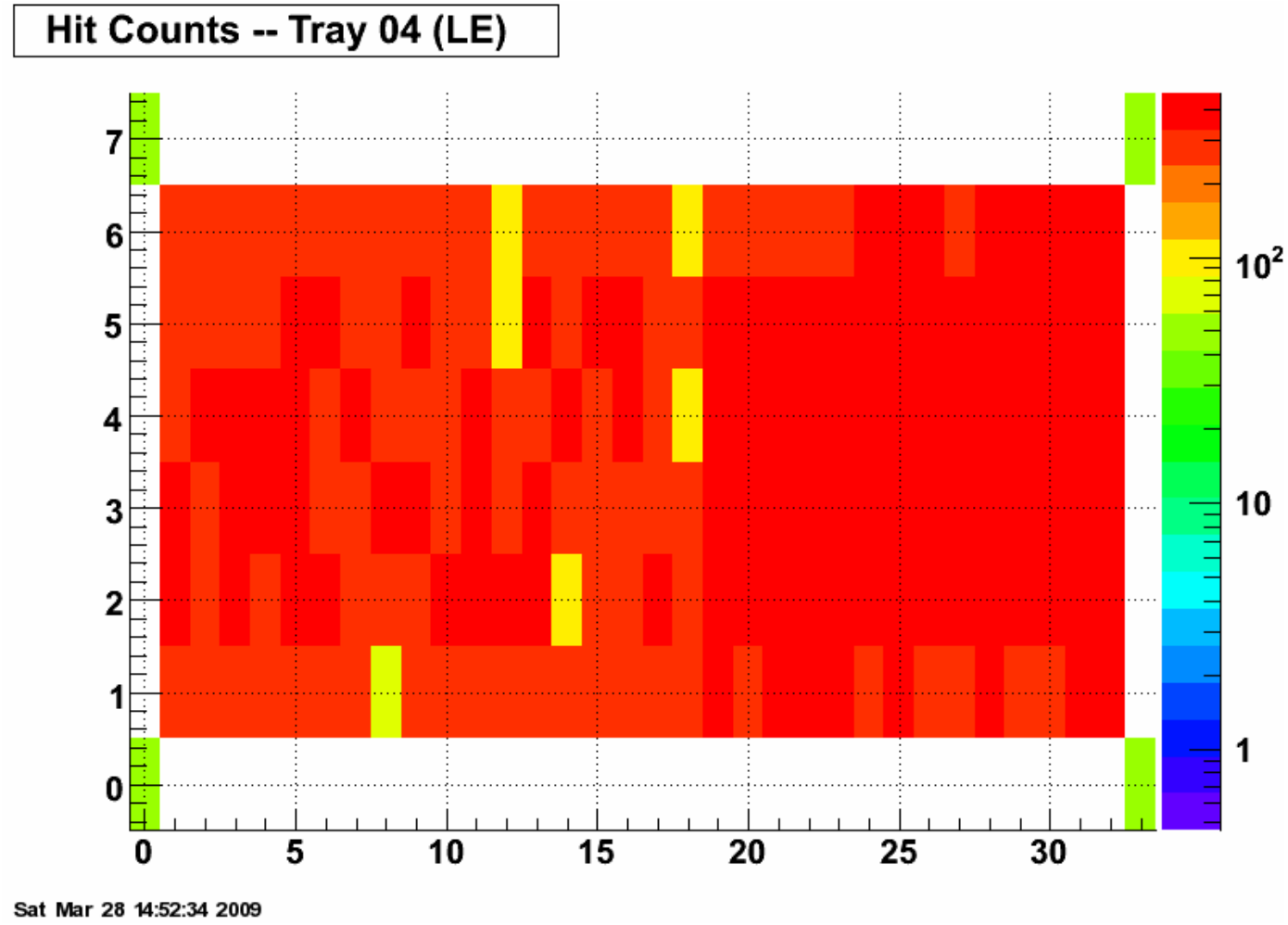

Figure 6.4: Hit pattern ontTray 4 in Run 10087063 in 2D map. Four green struts at corners are scale indicators, not related to real hits. X-axis corresponds to module location and Y-axis corresponds to pad location.

Tray Pos.	Tray SN	No. of Dead Ch	Dead Ch No. (Module, Pad)
4	6	6	43 (8, 1), 71 (12, 5), 72 (12, 6), 80 (14, 2), 106 (18, 4), 108 (18, 6)
10	60	1	49 (9, 1)
60	55	1	124 (21, 4)
76	4	1	168 (28, 6)

Table 6.6: Summary of Dead Channels in Run 10087063.

6.3.1 Discriminator Threshold Scan

On February 19, 2009 (Day 50), several noise runs were devoted to a threshold scan study similar to the test mentioned in Section 5.5.1. A list of the runs is shown in Table 6.7. As mentioned in the table, some of the raw DAQ files are not used in the analysis due to data corruption. We measured the average noise rates for each of the 192 channels on each installed tray. While most of the trays reacted well throughout the whole range of thresholds, 500–2500 mV, as shown through example in Figure 6.5 for Tray 1, some trays showed a divergence in lower region, 500–600 mV, as can be seen in Figure 6.6 for Tray 78. Values above 100 Hz tend to indicate that the threshold was too low, and this is seen in a few trays. Full listing can be found in Appendix 1.1. The STAR TOF group concluded that it was worthwhile to test the 1200 mV threshold during beam for a substantial period based of this study.

Run No.	Threshold (mV)	No. of Events	No. of Errors	Note
1005058	2500	1M	71	1% dead time, 3600–4100Hz.
1005059	2500	1M	67	
1005060	1500	1M	74	
1005061	1500	1M	65	
1005062	1000	1M	553	enabled more EVB's before this run. raw_3030001.daq was skipped.
1005063	1000	1M	517	
1005064	500	1M	504	50% dead time, raw_(503001|603001).daq were skipped.
1005065	500	1M	496	40–50% dead time, raw_503001.daw was skipped.
1005066	600	1M	n/a	2-3% dead time.
1005067	600	1M	517	2-3% dead time.
1005068	800	1M	n/a	1-3% dead time.
1005069	800	1M	547	1-3% dead time.
1005070	550	1M	542	3-8% dead time.
1005071	1500	1M	572	1-3% dead time.

Table 6.7: List of Threshold Scan Runs on Day 50.

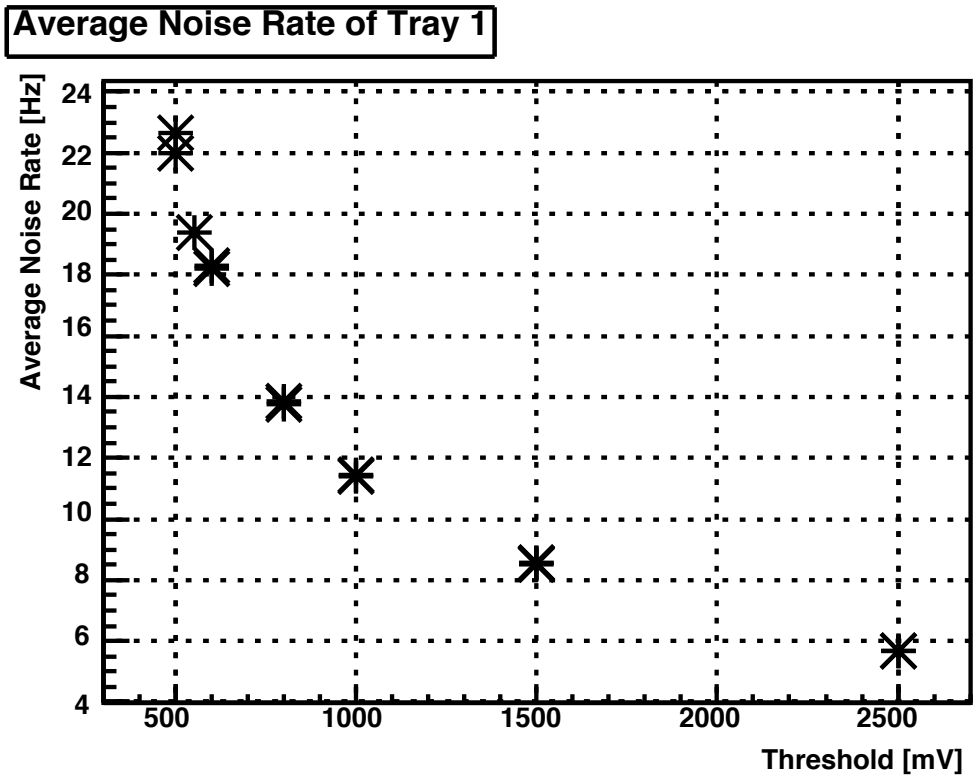

Figure 6.5: The threshold scan result for Tray 1 on Day 50.

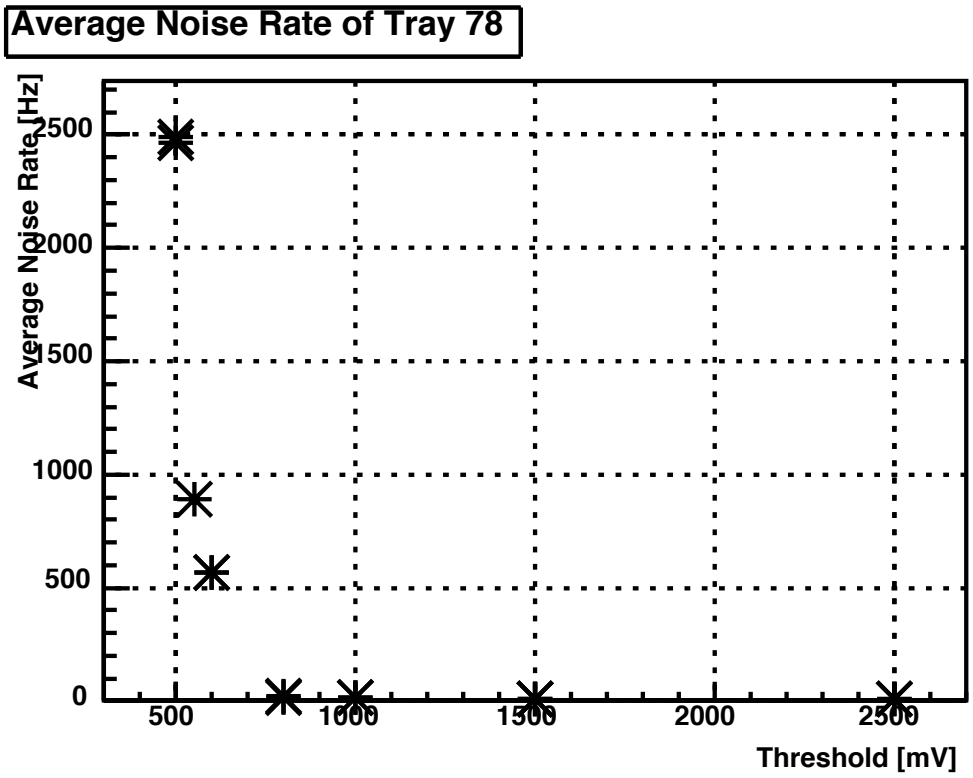

Figure 6.6: The threshold scan result for Tray 78 on Day 50.

Chapter 7

Conclusions

7.1 Summary

An overview of the STAR experiment at RHIC was given in Chapter 2. It discussed all major subsystems of the STAR detector. The design and expected performance of the STAR TOF system were described in Chapter 3. The system consists of two subdetectors: the start-side pVPD and the stop-side TOF detector trays, and both systems are equipped with newly developed electronics. The final configuration of pVPD has been functional since RHIC Run 6 and the stop-side detector has been under gradual upgrade. We conducted various tests, such as MRPC module noise rate tests, cosmic ray timing resolution tests, during the STAR TOF research and development phase. The apparatus, procedure, and selected results of these tests were described in Chapter 4. The knowledge accumulated during the period was utilized in the quality control activities done during the stop-side tray production. We assembled and tested all stop-side trays, 120 plus 6 spares, at UT and shipped them to BNL over the past two years. Tray assembly and test procedures, and selected results of the tests were presented in Chapter 5.

Chapter 6 provided details of the status of the detector and the results from

the RHIC Runs 8-9. 5 stop-side trays were installed and commissioned during Run 8. 94 trays were installed before Run 9 and 86 trays out of the 94 were active during the run. The coverages of the stop-side detector were 4.2 % and 71.7 % of the full system, for Run 8 and Run 9, respectively. Considerable QA efforts described in the previous two chapters led to a delivered TOF system with only 2 dead channels out of 960 for Ru8 and 10 channels out of 16,512 channels for Run 9. The average number of live channels per tray for these two runs, 195.60 and 195.88, respectively, is significantly above design requirement: number of live channels per tray greater than 175. The requirement was satisfied not only for average, but also for each installed tray.

7.2 Future Direction

STAR collected data from p+p collisions at 250 GeV and 100 GeV in RHIC Run 9 from January 16 to July 4, 2009 with 86 TOF trays. The coverage of the system is a factor of 17 larger than that of the previous year. The STAR TOF group checked the system status constantly during the run and already has started calibration of the data. Although the preliminary outcome seems promising, fully calibrated results are still in progress.

Appendix

Appendix 1

Detail Results

1.1 Threshold Scan on Day 50

Full results from the threshold scan study mentioned in Section 6.3.1 are listed in this section. The study was performed with a threshold range of 500–2500 mV, on February 19, 2009 (Day 50) at BNL.

1.2 Dead Channel Search

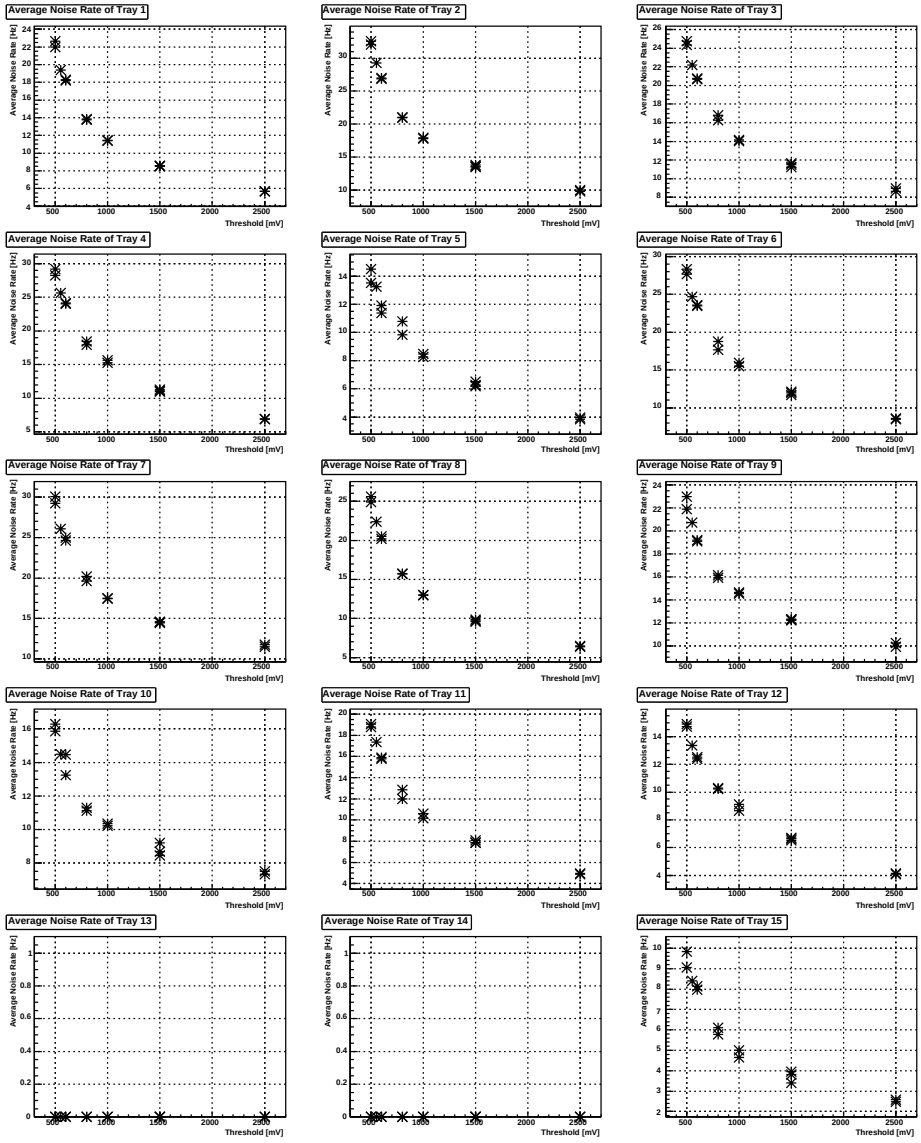

Figure 1.1: Threshold Scan Results for Trays 1–15

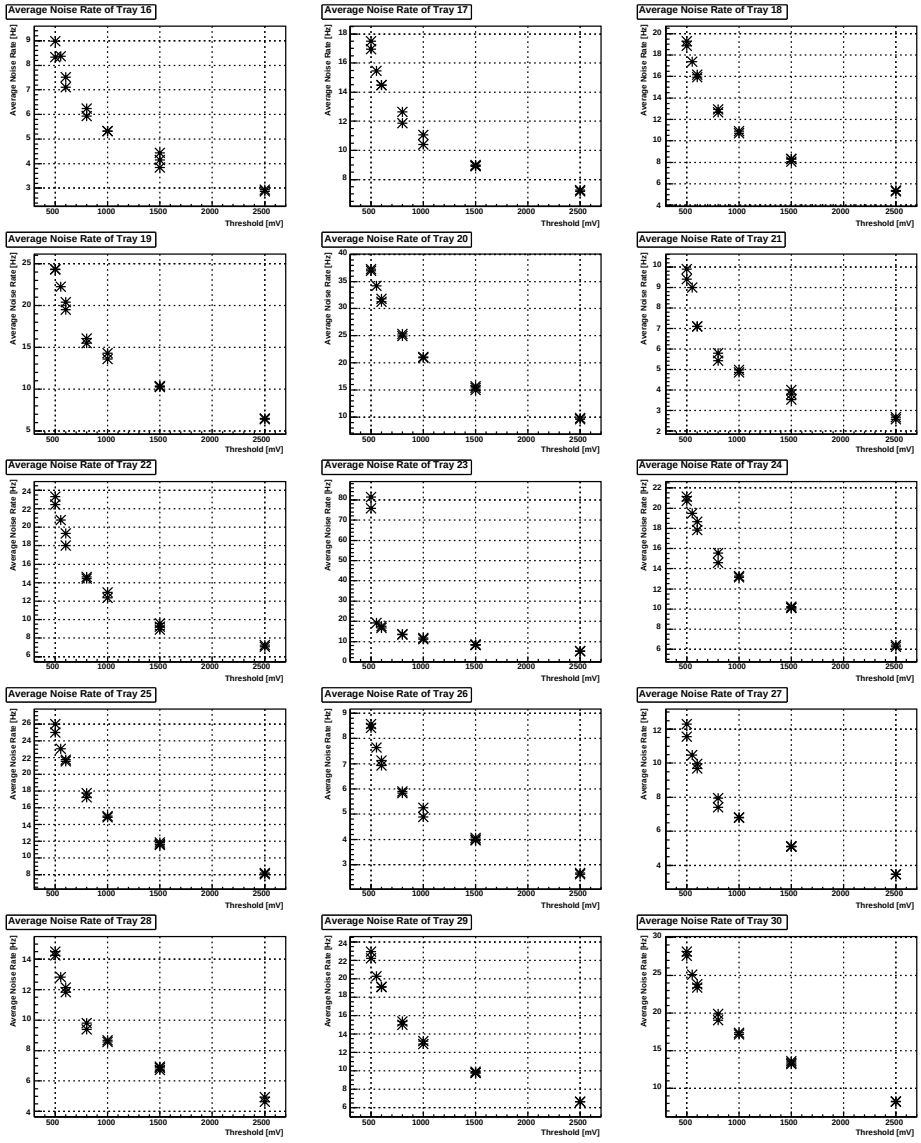

Figure 1.2: Threshold Scan Results for Trays 16–30

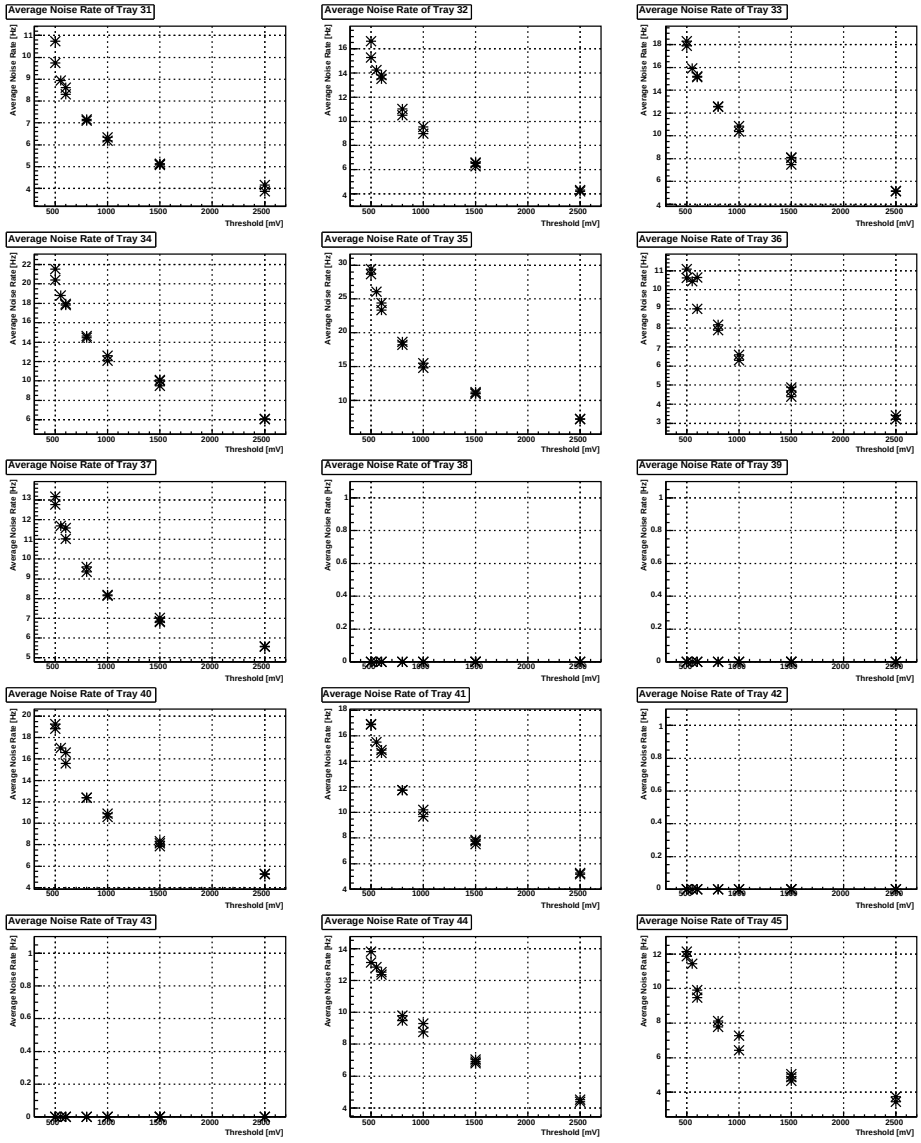

Figure 1.3: Threshold Scan Results for Trays 31–45

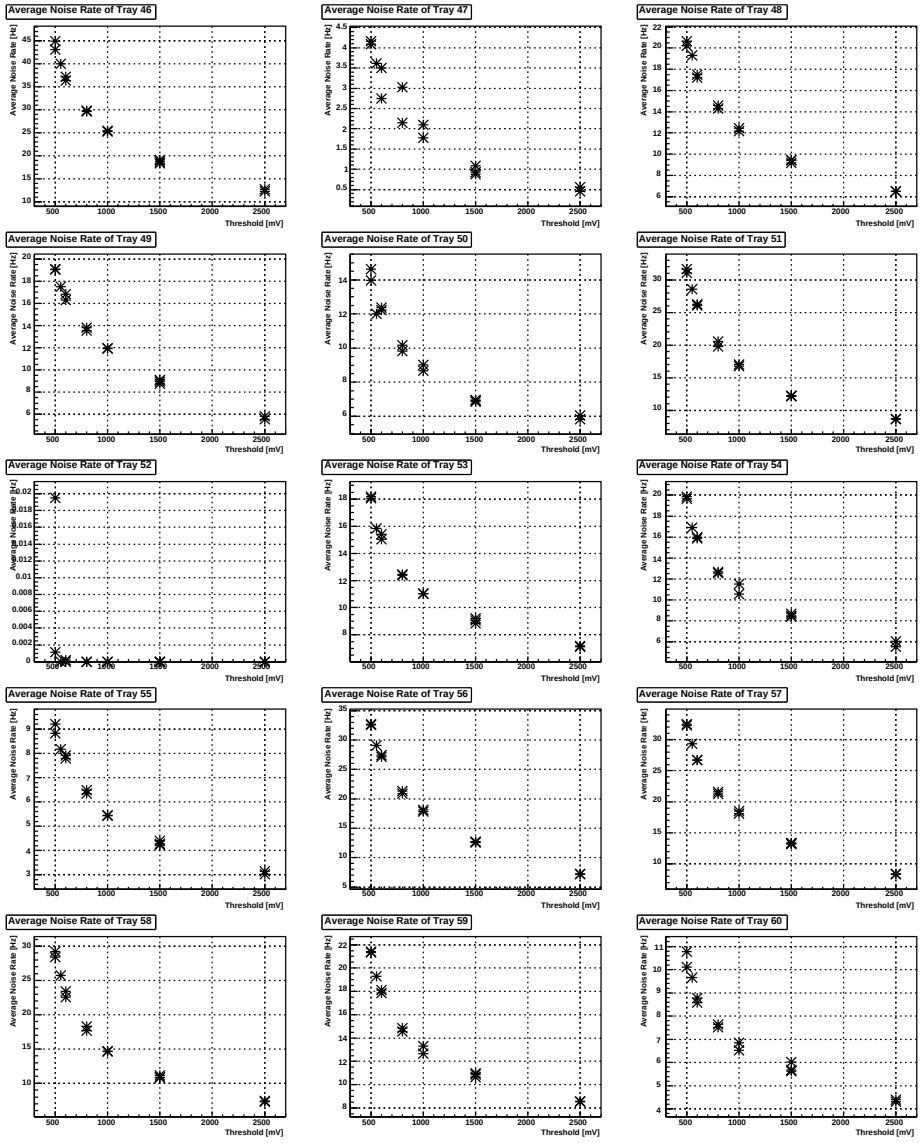

Figure 1.4: Threshold Scan Results for Trays 46–60

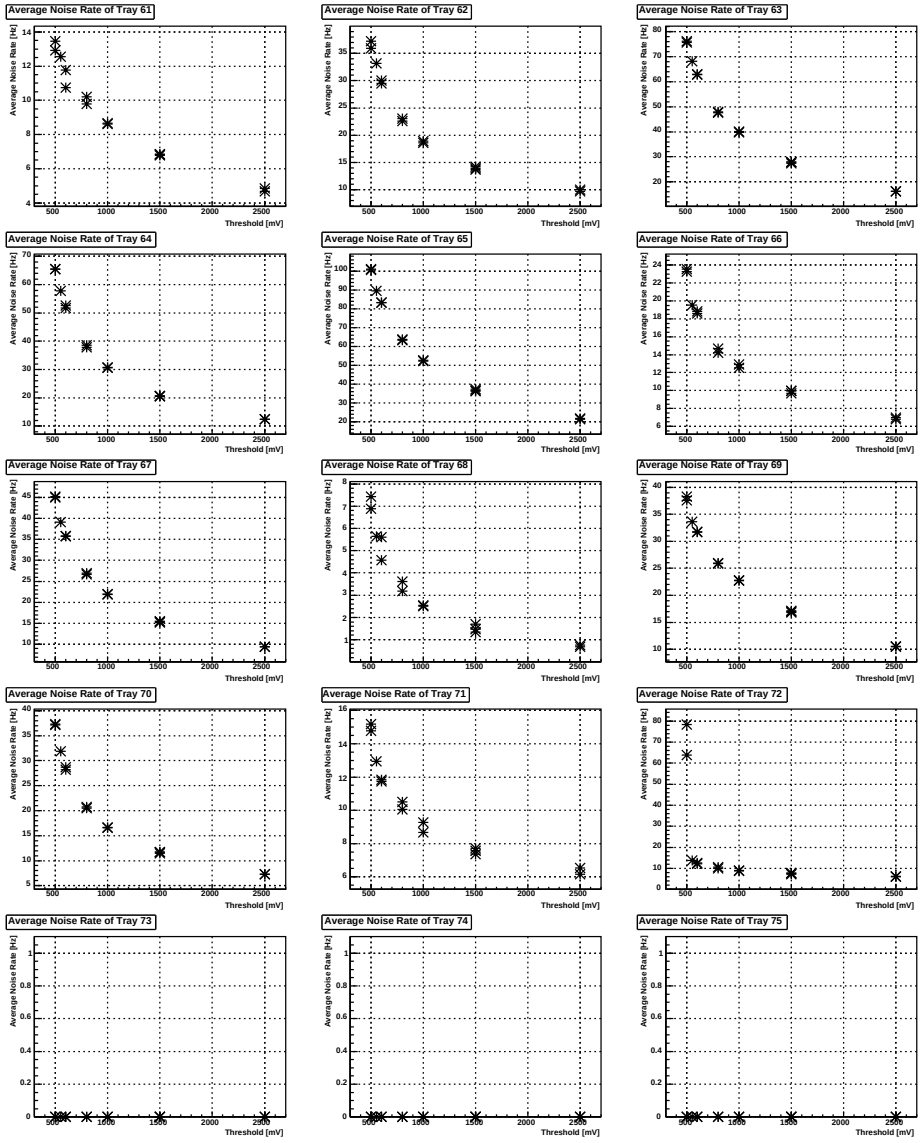

Figure 1.5: Threshold Scan Results for Trays 61–75

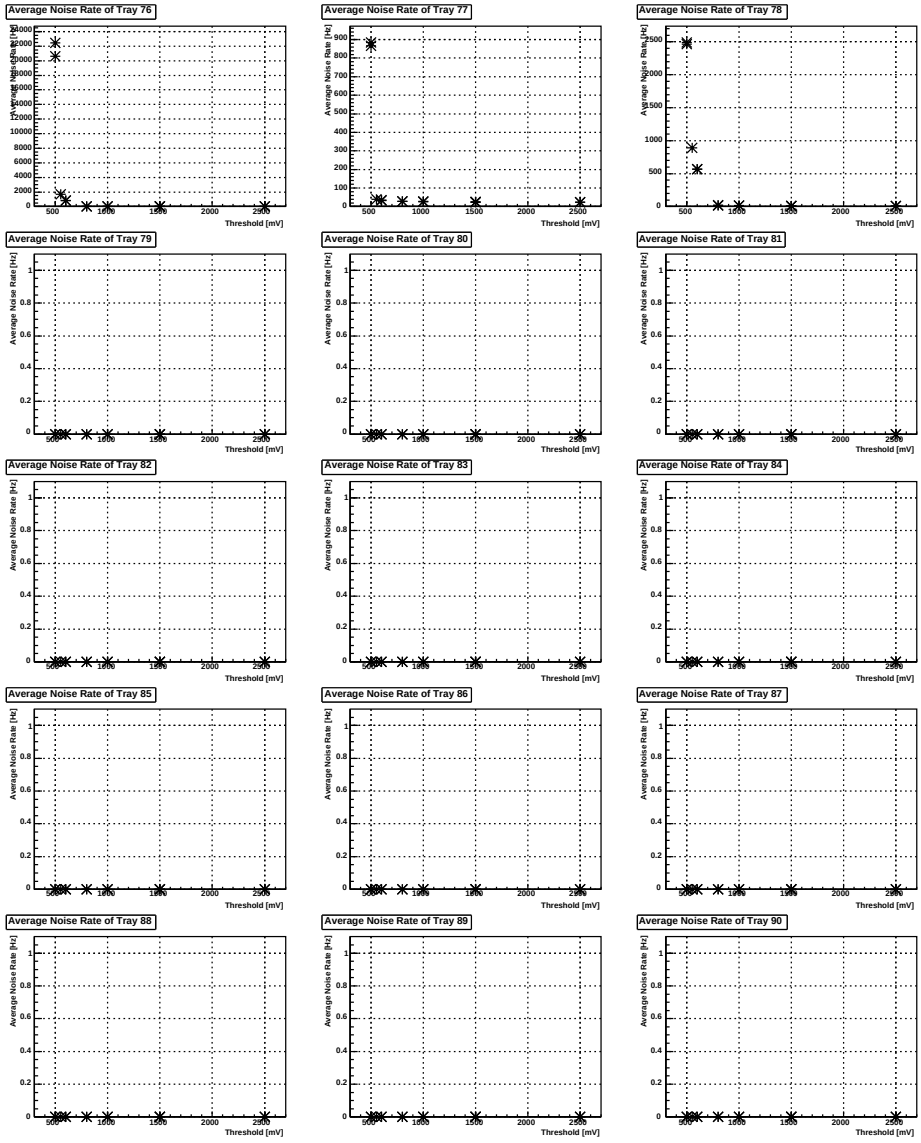

Figure 1.6: Threshold Scan Results for Trays 76–90

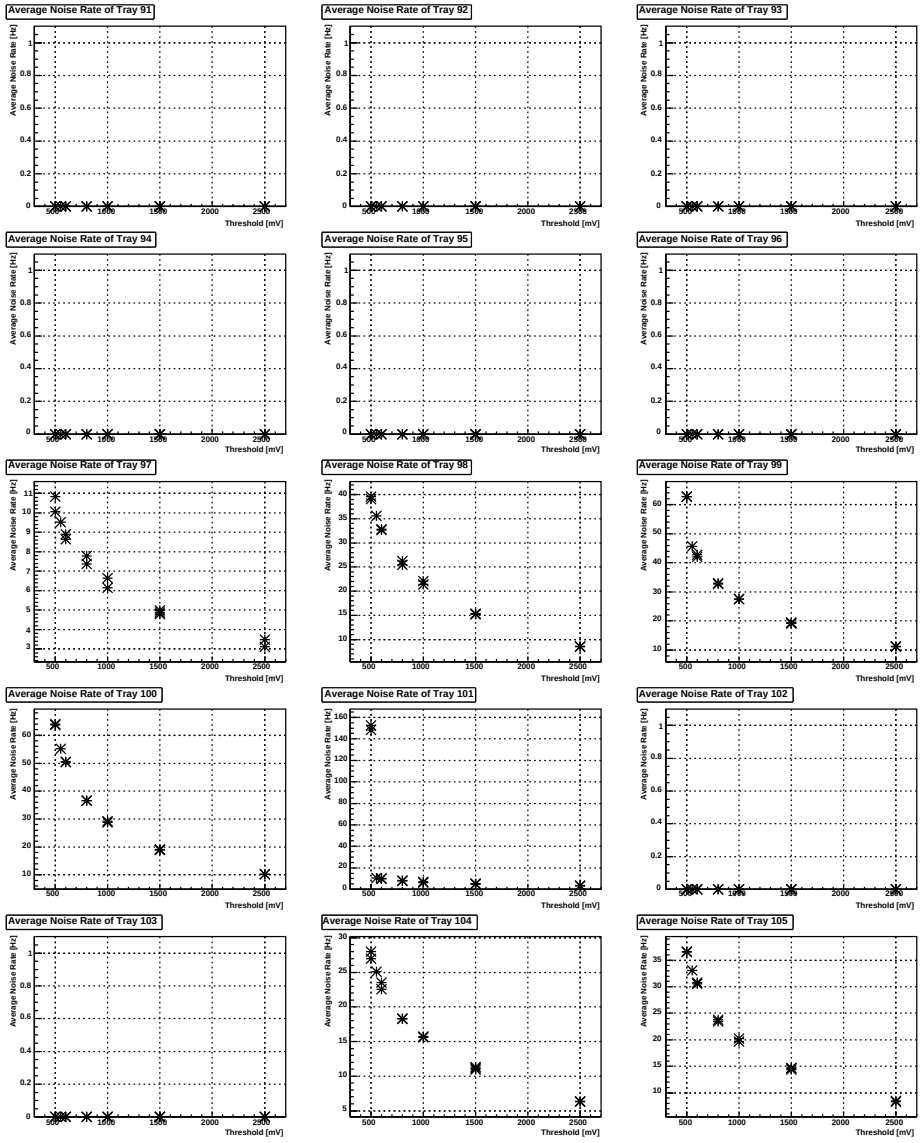

Figure 1.7: Threshold Scan Results for Trays 91–105

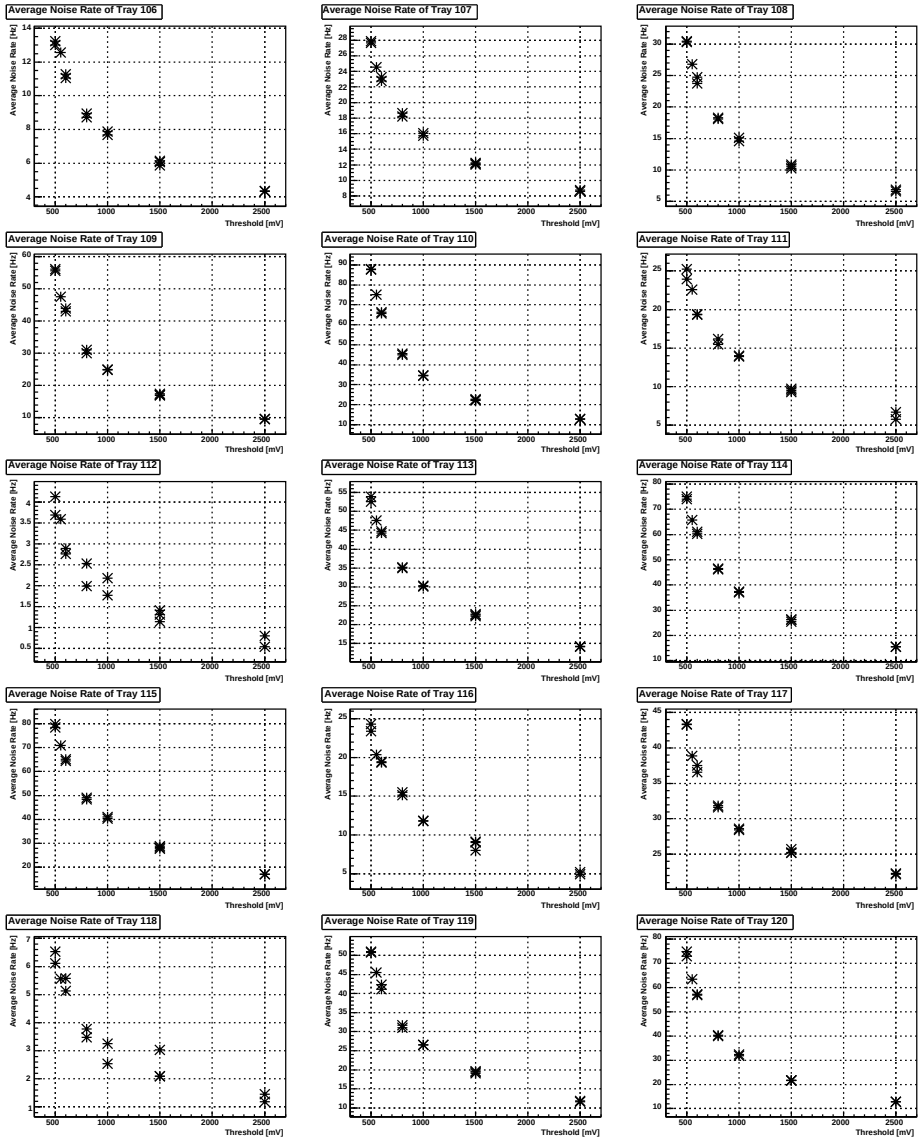

Figure 1.8: Threshold Scan Results for Trays 106–120

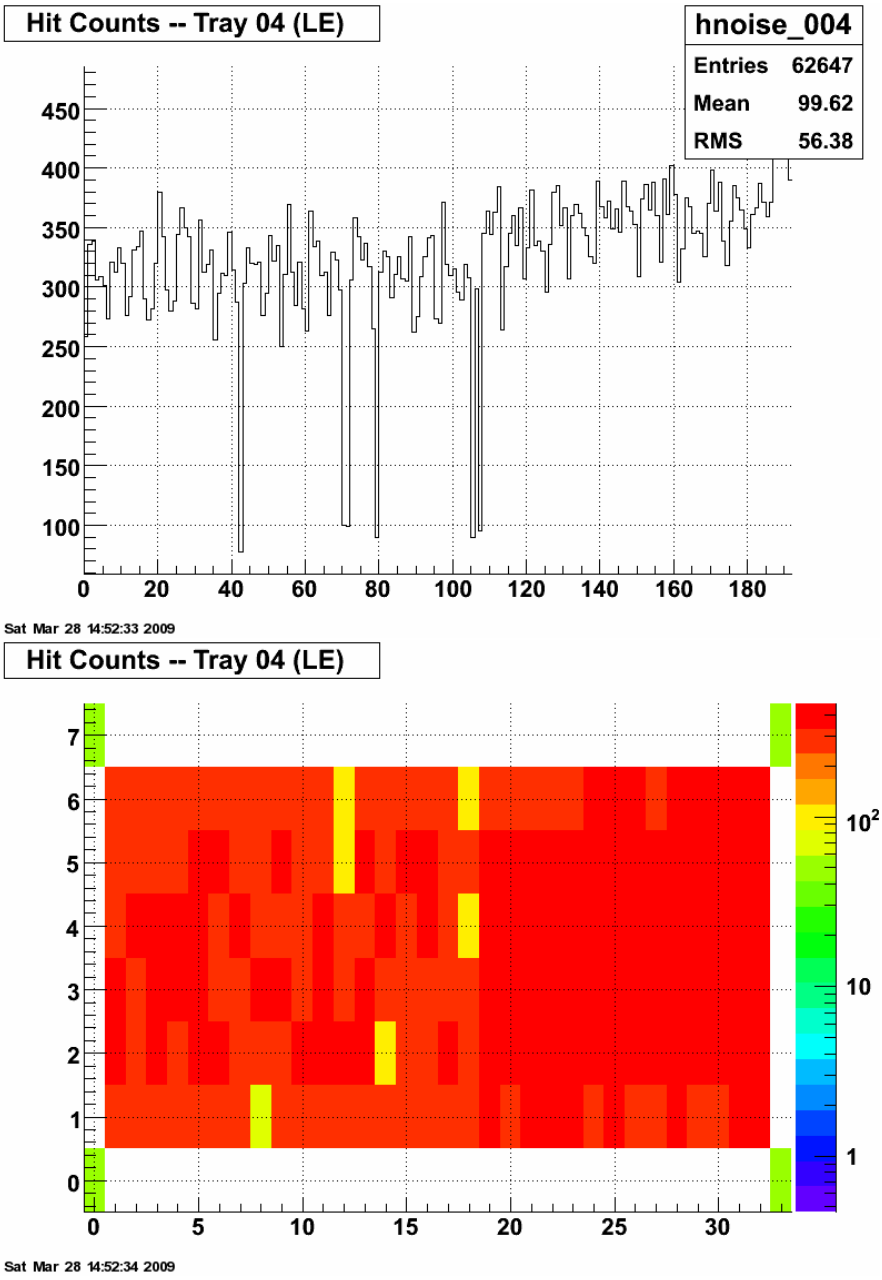

Figure 1.9: Tray 4

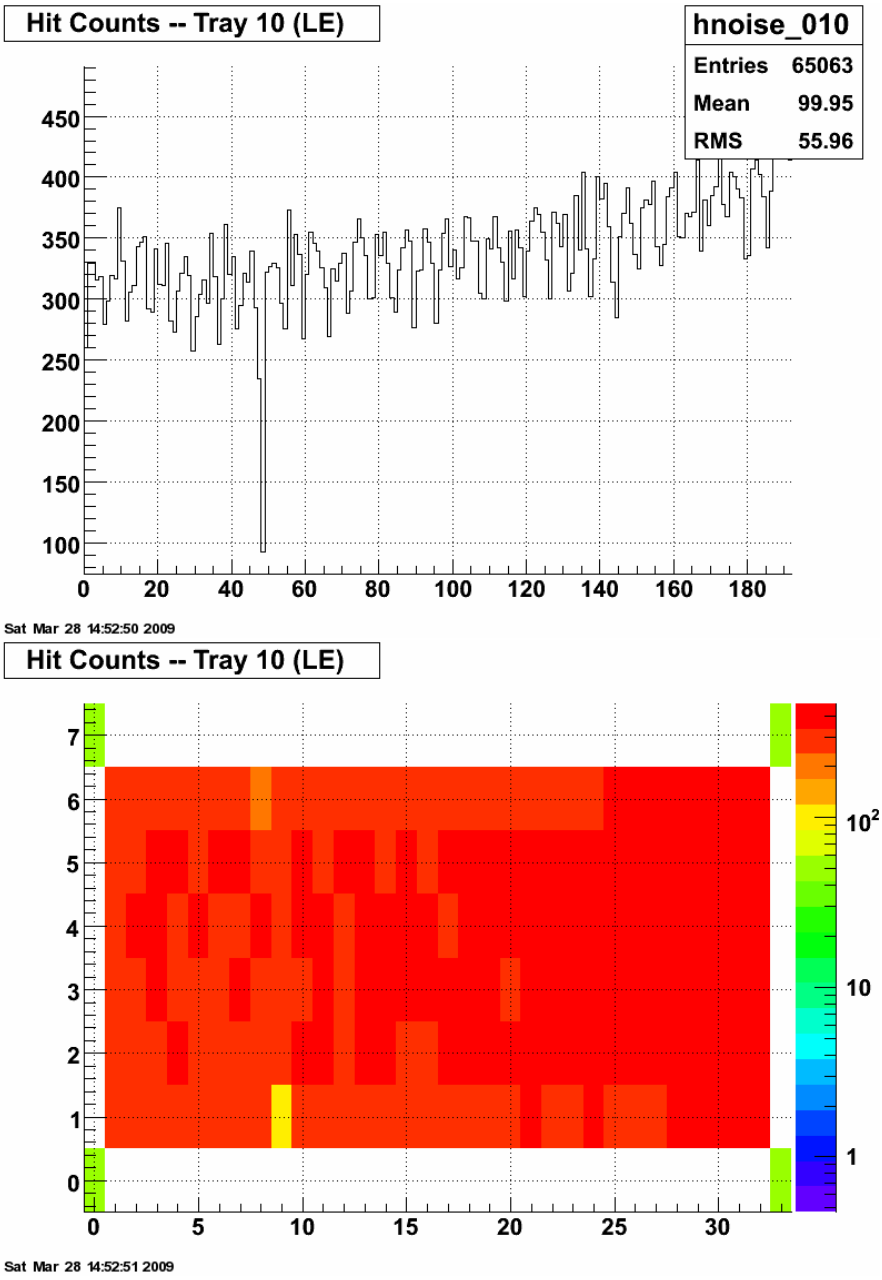

Figure 1.10: Tray 10

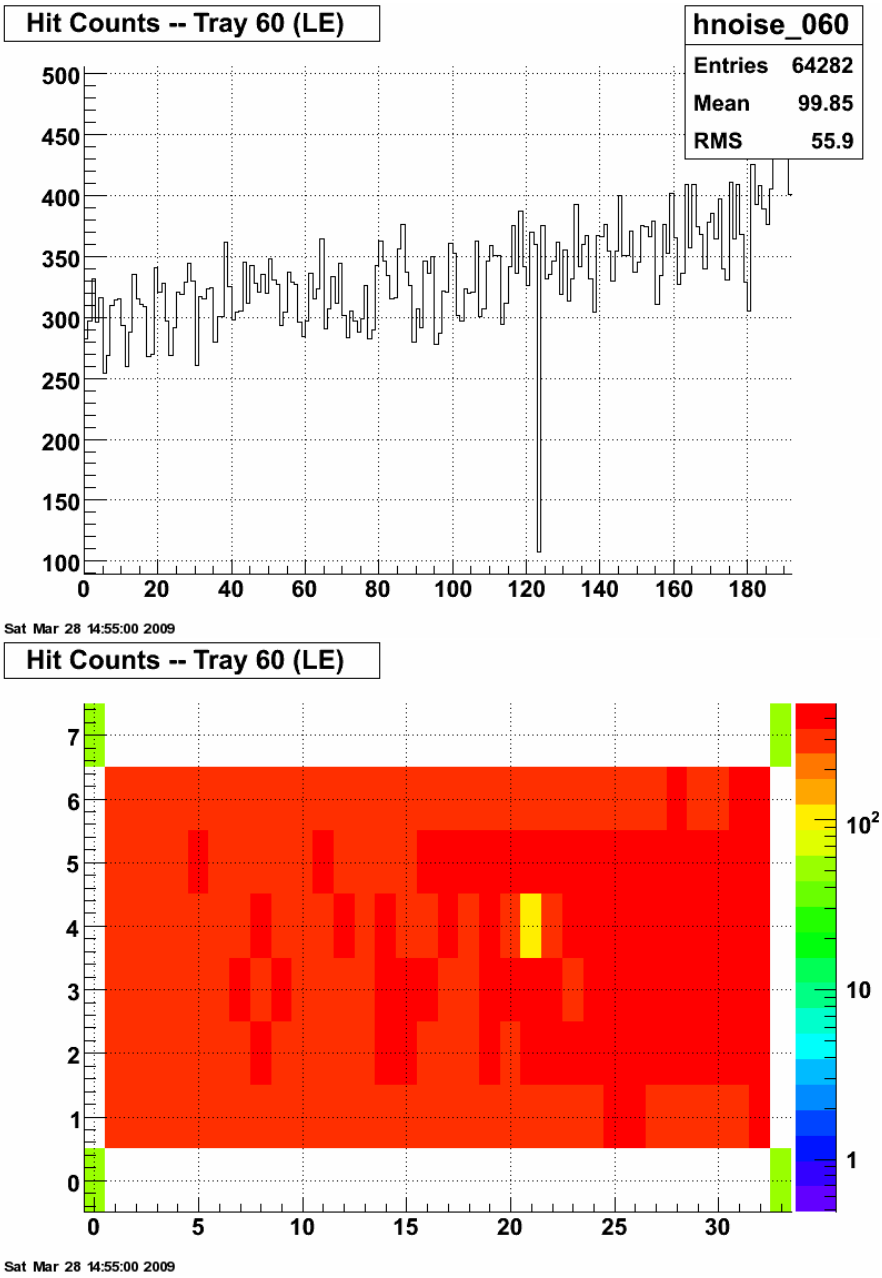

Figure 1.11: Tray 60

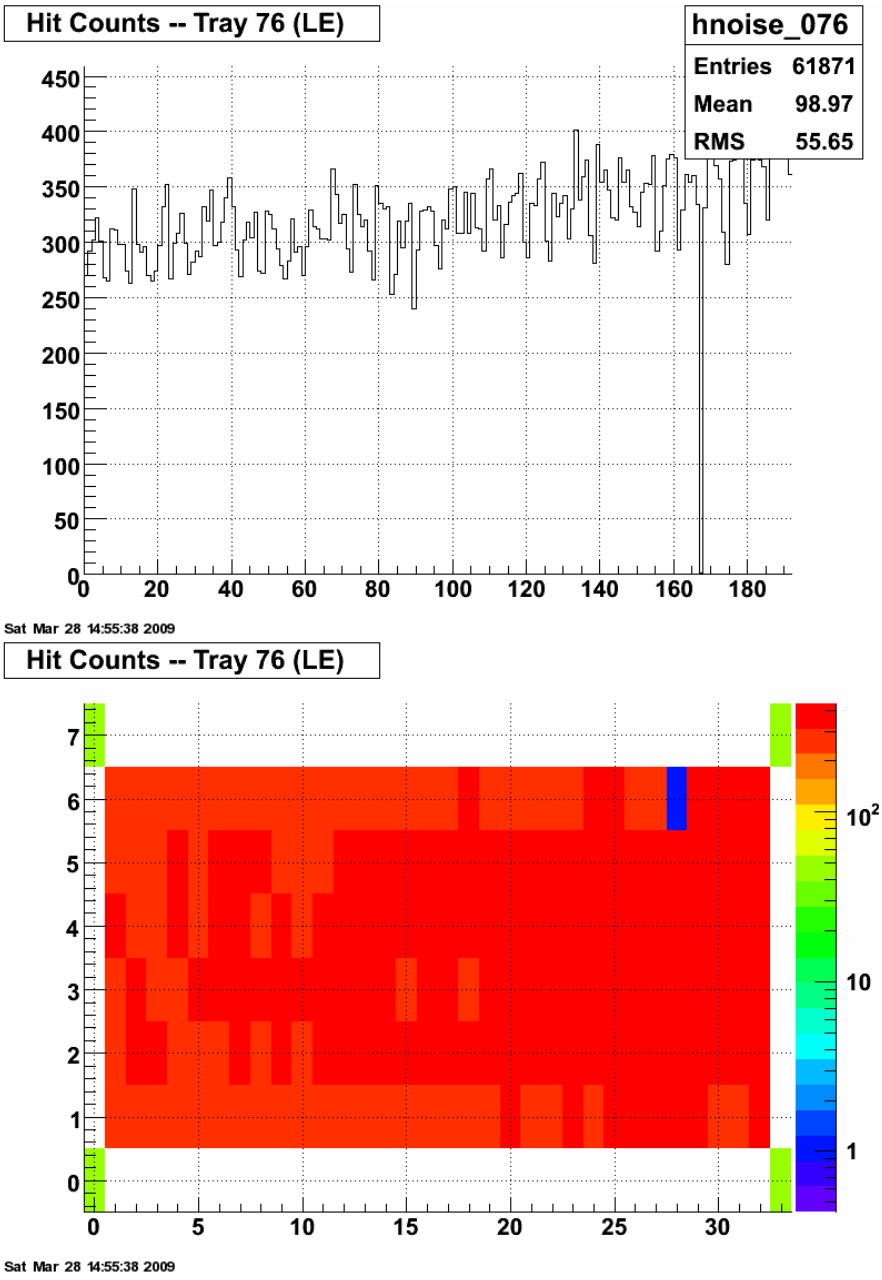

Figure 1.12: Tray 76

Appendix 2

Software

2.1 Anaconda

A GUI software package named Anaconda was developed to operate various tests at the Wide Angle Hall at RHIC. It communicates with TOF trays via a CAN-bus network and provides a human interface to various functions such as configuring and checking status of the on-board electronics. Most importantly, Anaconda can take noise rate data for all channels on a tray. A built-in analysis routine provides realtime feedback to users and generates files of raw-data and histograms at the end of each run. The test results are used for quality assurance activities during STAR operations (see Sec. 5.4 for the test).

The software was designed and developed using pcanloop[1] with original C-version GTK+ and CERN ROOT libraries. Screenshots of the software are shown in Figure 2.1 and Figure 2.2 [2].

2.2 Anaconda Ⅱ

Anaconda Ⅱ is a GUI for the STAR TOF electronics system. The software was developed between October 2008 and present. It is written in C++ with Qt[3] and comes with a CAN-bus network device simulator for development and debugging[4]. Its configuration parameters are stored in an SQLite database so that re-compiling is not necessary for updating the parameters. It is relatively easy to maintain the database. Figure 2.3 shows a screenshot of this software.

[1] pcanloop has been developed by J. Schambach
[2] CVS repository of the source files is located at tof/anaconda.
[3] Qt – A cross-platform application and UI framework.
[4] CVS repository of the source files is located at tof/anaconda_two.

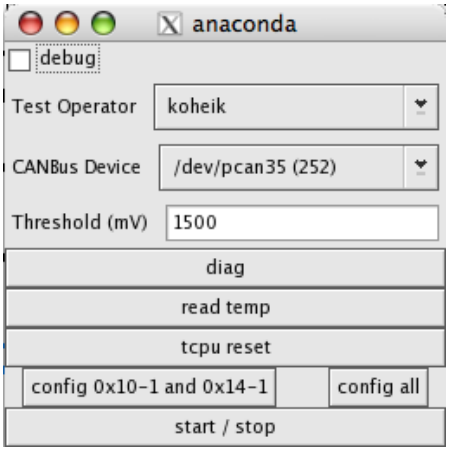

Figure 2.1: Anaconda – Test Stand Controller.

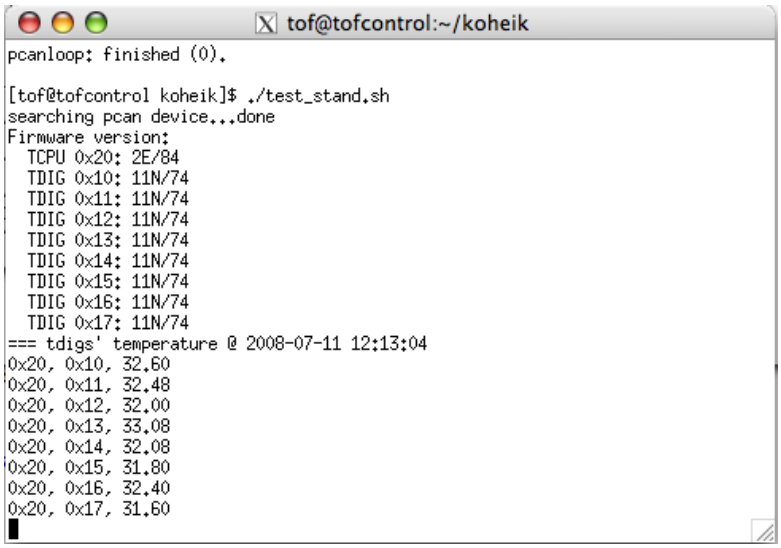

Figure 2.2: Anaconda – Test Stand Controller.

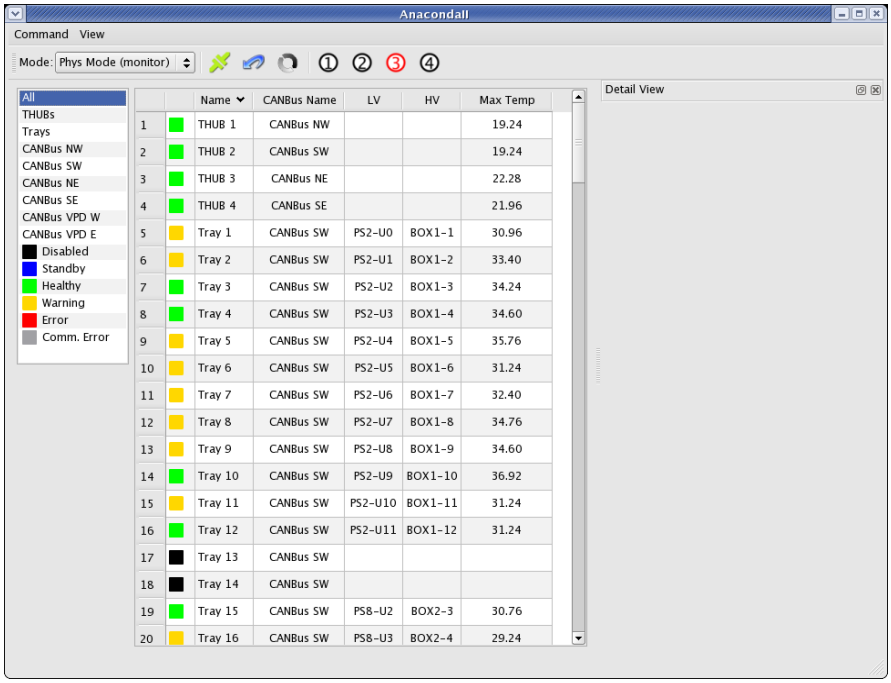

		Name	CANBus Name	LV	HV	Max Temp
1		THUB 1	CANBus NW			19.24
2		THUB 2	CANBus SW			19.24
3		THUB 3	CANBus NE			22.28
4		THUB 4	CANBus SE			21.96
5		Tray 1	CANBus SW	PS2-U0	BOX1-1	30.96
6		Tray 2	CANBus SW	PS2-U1	BOX1-2	33.40
7		Tray 3	CANBus SW	PS2-U2	BOX1-3	34.24
8		Tray 4	CANBus SW	PS2-U3	BOX1-4	34.60
9		Tray 5	CANBus SW	PS2-U4	BOX1-5	35.76
10		Tray 6	CANBus SW	PS2-U5	BOX1-6	31.24
11		Tray 7	CANBus SW	PS2-U6	BOX1-7	32.40
12		Tray 8	CANBus SW	PS2-U7	BOX1-8	34.76
13		Tray 9	CANBus SW	PS2-U8	BOX1-9	34.60
14		Tray 10	CANBus SW	PS2-U9	BOX1-10	36.92
15		Tray 11	CANBus SW	PS2-U10	BOX1-11	31.24
16		Tray 12	CANBus SW	PS2-U11	BOX1-12	31.24
17		Tray 13	CANBus SW			
18		Tray 14	CANBus SW			
19		Tray 15	CANBus SW	PS8-U2	BOX2-3	30.76
20		Tray 16	CANBus SW	PS8-U3	BOX2-4	29.24

Figure 2.3: Anaconda II – TOF Electronics Status Monitor.

The main features of the software include:

- configuring electronics: THUBs, TCPUs and TDIGS,
- querying and displaying the status of electronics,
- detecting and reporting errors,
- logging electronics' temperatures,
- setting the electronics to rest when users explicitly command or when it receives an end-of-run command from the STAR DAQ system.

Appendix 3

Acronyms

ADC Analog-to-Digital Converter

AGS Alternating Gradient Synchrotron [BNL]

ALICE A Large Ion Collider Experiment at CERN LHC

BNL Brookhaven National Laboratory

CAMAC Computer Automated Measurement And Control

CAN Controller Area Network

CERN *Conseil Européen pour la Recherche Nucléaire* (European Organization for Nuclear Research)

CMS Compact Muon Spectrometer [CERN LHC]

CTB Central Trigger Barrel

DAQ Data Acquisition System

DDL Detector Data Link [ALICE]

DIU DDL Destination Interface Unit

FEE Front-End Electronics

GUI Graphical User Interface

IDC Insulation-Displacement Connector

IDE Integrated Development Environment

LHC Large Hadron Collider

MRPC Multi-gap Resistive Plate Chamber

NIM Nuclear Instrumentation Module

PCB Printed Circuit Board

QCD Quantum Chromo-Dynamics

QGP Quark Gluon Plasma

RHIC Relativistic Heavy Ion Collider [BNL]

RORC Read-Out Receiver Card

SerDes Serializer / Deserializer

SPS Super Proton Synchrotron [CERN]

STAR Solenoidal Tracker At RHIC

SIU DDL Source Interface Unit

TDC Time-to-Digital Converter

TOF Time-Of-Flight (Detector)

TOT Time-over-Threshold

TPC Time Projection Chamber

USTC University of Science and Technology of China

UT University of Texas at Austin

VME VERSAModule Eurocard

Bibliography

[1] C. Amsler *et al.*, Physics Letters B **667**, 1 (2008), review of Particle Physics.

[2] R. Ray, Nuclear Physics A **715**, 45c (2003), quark Matter 2002, Proceedings of the 16th International Conference on Ultra-Relativistic Nucleus-Nucleus Collisions.

[3] C. Adler *et al.*, Phys. Rev. Lett. **90**, 082302 (2003).

[4] C. Albajar *et al.*, Nucl. Phys. **B309**, 405 (1988).

[5] X.-N. Wang, Phys. Rev. D **43**, 104 (1991).

[6] M. S. Daugherity, Ph.D. thesis, The University of Texas at Austin, Austin, Texas, 2008.

[7] J. Putschke, in *The 24th Winter Workshop on Nuclear Dynamics*, edited by W. Bauer, R. Bellwied, J. W. Harris, and C. Markert (EP Systema, Budapest, Hungary, 2008).

[8] P. Fachini *et al.*, Proposal for a Large Area Time of Flight System for STAR, 2004, `http://wjllope.rice.edu/~TOF/TOF/Documents/TOF_20040524.pdf`.

[9] D. Kharzeev and E. Levin, Phys. Lett. **B523**, 79 (2001).

[10] W. Xin-Nian and B. Mller, Nuclear Physics A **566**, 555 (1994).

[11] E. Shuryak, Nuclear Physics A **566**, 559 (1994).

[12] Z. Lin and M. Gyulassy, Nuclear Physics A **590**, 495 (1995).

[13] H. Satz, Reports on Progress in Physics **63**, 1511 (2000).

[14] A. Andronic, P. Braun-Munzinger, K. Redlich, and J. Stachel, Nuclear Physics A **715**, 529c (2003), quark Matter 2002, Proceedings of the 16th International Conference on Ultra-Relativistic Nucleus-Nucleus Collisions.

[15] T. Ludlam, Nuclear Instruments and Methods in Physics Research Section A: Accelerators, Spectrometers, Detectors and Associated Equipment **499**, 428 (2003), the Relativistic Heavy Ion Collider Project: RHIC and its Detectors.

[16] J. M. Landgraf *et al.*, Nuclear Instruments and Methods in Physics Research Section A: Accelerators, Spectrometers, Detectors and Associated Equipment **499**, 762 (2003), the Relativistic Heavy Ion Collider Project: RHIC and its Detectors.

[17] R. Bellwied *et al.*, Nuclear Instruments and Methods in Physics Research Section A: Accelerators, Spectrometers, Detectors and Associated Equipment **499**, 640 (2003), the Relativistic Heavy Ion Collider Project: RHIC and its Detectors.

[18] L. Arnold *et al.*, Nuclear Instruments and Methods in Physics Research Section A: Accelerators, Spectrometers, Detectors and Associated Equipment **499**, 652 (2003), the Relativistic Heavy Ion Collider Project: RHIC and its Detectors.

[19] M. Anderson *et al.*, Nuclear Instruments and Methods in Physics Research Section A: Accelerators, Spectrometers, Detectors and Associated Equipment **499**, 659 (2003), the Relativistic Heavy Ion Collider Project: RHIC and its Detectors.

[20] M. Beddo *et al.*, Nuclear Instruments and Methods in Physics Research Section A: Accelerators, Spectrometers, Detectors and Associated Equipment **499**, 725 (2003), the Relativistic Heavy Ion Collider Project: RHIC and its Detectors.

[21] C. E. Allgower *et al.*, Nuclear Instruments and Methods in Physics Research Section A: Accelerators, Spectrometers, Detectors and Associated Equipment **499**, 740 (2003), the Relativistic Heavy Ion Collider Project: RHIC and its Detectors.

[22] M. M. Aggarwal *et al.*, Nuclear Instruments and Methods in Physics Research Section A: Accelerators, Spectrometers, Detectors and Associated Equipment **499**, 751 (2003), the Relativistic Heavy Ion Collider Project: RHIC and its Detectors.

[23] W. J. Llope *et al.*, Nuclear Instruments and Methods in Physics Research Section A: Accelerators, Spectrometers, Detectors and Associated Equipment **522**, 252 (2004).

[24] C. Adler *et al.*, Nuclear Instruments and Methods in Physics Research Section A: Accelerators, Spectrometers, Detectors and Associated Equipment **499**, 433 (2003), the Relativistic Heavy Ion Collider Project: RHIC and its Detectors.

[25] Y. V. Fisyak *et al.*, Journal of Physics: Conference Series **119**, 032017 (10pp) (2008), international Conference on Computing in High Energy and Nuclear Physics (CHEP07).

[26] E. Judd, STAR Trigger Introduction, `http://www.star.bnl.gov/public/trg/runschool/introduction/index.html`.

[27] H. Crawford *et al.*, Forward Meson Spectrometer (FMS) status report, 2005 STAR Collaboration Meeting; `http://hena.lbl.gov/FMS/talks/HC_star_collab_050731.ppt`.

[28] T. Ludlam, Nuclear Instruments and Methods in Physics Research Section A: Accelerators, Spectrometers, Detectors and Associated Equipment **499**, 428 (2003), the Relativistic Heavy Ion Collider Project: RHIC and its Detectors.

[29] F. S. Bieser *et al.*, Nuclear Instruments and Methods in Physics Research Section A: Accelerators, Spectrometers, Detectors and Associated Equipment **499**, 766 (2003), the Relativistic Heavy Ion Collider Project: RHIC and its Detectors.

[30] E. C. Zeballos *et al.*, Nuclear Instruments and Methods in Physics Research Section A: Accelerators, Spectrometers, Detectors and Associated Equipment **373**, 35 (1996).

[31] F. Anghinolfi *et al.*, Nuclear Instruments and Methods in Physics Research Section A: Accelerators, Spectrometers, Detectors and Associated Equipment **533**, 183 (2004), proceedings of the Seventh International Workshop on Resistive Plate Chambers and Related Detectors.

[32] J. Christensen, HPTDC – High Performance Time to Digital Converter, 2004, http://tdc.web.cern.ch/tdc/hptdc/docs/hptdc_manual_ver2.2.pdf.

[33] H. Matis *et al.*, Controlled STAR Note 229A (1998), http://drupal.star.bnl.gov/STAR/files/starnotes/csn0229a.pdf.

Vita

Kohei Kajimoto was born in Kyoto. In April, 1995, he entered Waseda University in Tokyo, Japan. He received the degree of Bachelor of Science in March, 2000 and the degree of Master of Science in March, 2002 from Waseda University. In September, 2002, he entered the Graduate School at The University of Texas at Austin.

Permanent Address: 1206-49, Myodenjimae Otsu, Uwajima, Ehime,
798-0071, Japan

This manuscript was typed with LaTeX by the author.